HYBRID CONJUGATED POLYMER / ZINC OXIDE COMPOSITE PHOTOVOLTAIC DEVICES

by

Dana C. Olson

A thesis submitted to the Faculty and Board of Trustees of the Colorado School of Mines in partial fulfillment of the requirements for the degree of Doctor of Philosophy (Materials Science).

Golden, Colorado

Date_____

Signed: _____
Dana C. Olson

Approved: _____
Dr. Reuben T. Collins
Thesis Advisor

Approved: _____
Dr. David S. Ginley
Thesis Advisor

Golden, Colorado

Date_____

_____
Dr. John J. Moore
Professor and Department Head
Materials Science

ABSTRACT

Organic semiconductor-based photovoltaic devices offer the promise of a low cost photovoltaic technology that could be manufactured via large-scale, roll-to-roll printing techniques. Existing organic photovoltaic devices have currently achieved solar power conversion efficiencies approaching 5%. Though encouraging, higher efficiencies have not been achieved due to poor overlap between the absorption spectrum of the organic chromophores and the solar spectrum, non-ideal band alignment between the donor and acceptor species, and low charge carrier mobilities resulting from the disordered nature of organic semiconductors. To address the latter issues, we are investigating the development of nanostructured oxide/conjugated polymer composite hybrid photovoltaic devices. These composites can take advantage of the high electron mobilities attainable in oxide semiconductors and can be fabricated using low-temperature solution-based growth techniques. Additionally, the morphology of the composite can be controlled in a systematic way through control of the nanostructured oxide growth, and the electron affinity of the metal oxide can be more easily modified allowing for easily optimized band offsets between electron donor and acceptor materials.

In this study, we discuss the fabrication of such nanostructures and present results from poly(3-hexylthiophene)/ZnO nanofiber composite PV devices. The best performance with this nanostructured cell architecture produced an open circuit voltage (V_{oc}) of 440 mV, a short circuit current density (J_{sc}) of 2.2 mA/cm^2, a fill factor (FF) of 0.56, and a conversion efficiency (η) of 0.53% that is significantly higher than a comparable planar bilayer device. Finally, the incorporation of Mg into the ZnO material results in a reduced electron affinity, thereby increasing the open circuit voltage of the hybrid device. Bilayer devices were developed based on $Zn_{1-x}Mg_xO$ electron acceptors, which reduce the band offset between the donor and acceptor. This enhanced the V_{oc}

dramatically with an increase from 500 mV to 900 mV. This work presents the successful utilization of ZnO nanofibers into solid-state hybrid polymer/inorganic photovoltaic devices.

TABLE OF CONTENTS

LIST OF FIGURES

LIST OF TABLES

ACKNOWLEDGEMENTS

I would like to express sincere gratitude to my advisors both at the Colorado School of Mines and at the National Renewable Energy Laboratory (NREL), Prof. Reuben Collins, Dr. David Ginley, and Dr. Sean Shaheen, for providing me with the opportunity to grow as a student and an individual.

Also, a special thanks to Matthew White, Dr. Jorge Piris, Dr. Nikos Kopidakis, Dr. Don Selmarten, Dr. Brian Gregg, Dr, Maikel van Hest, Matthew Dabney, Jeff Allemen, Dr. Garry Rumbles, and everyone I have had the pleasure of knowing and working with while at NREL for the many productive discussions.

I would also like to thank Dr. Yuxiang Liu at Stanford University and Bobby To at NREL for the production of SEM images. This work was performed through the NREL DDRD program under the DOE contract DE-AC36-99-GO10337.

DEDICATION

This thesis is dedicated to my wife, who has been a great source of motivation and inspiration throughout this process. Also, this thesis is dedicated to my family who has supported me since the beginning of my studies. Finally, this thesis is dedicated to all those who believe in the richness of learning.

CHAPTER 1

INTRODUCTION

Abstract

This chapter introduces the concept and application of polymer-based solar cells. Different strategies towards hybrid organic/inorganic composite materials are reviewed and discussed with respect to application in photovoltaic devices. Using present knowledge from polymer bulk-heterojunction solar cells, the design of a simple, low-cost hybrid solar cell based on nanostructured metal oxides and conjugated polymers is presented. Organic semiconductor-based photovoltaic devices offer the promise of low cost photovoltaic technology that can be manufactured via large-scale, roll-to-roll printing techniques. State-of-the-art organic photovoltaic devices are currently limited to solar power conversion efficiencies of ~5%. The reasons for this are poor overlap between the absorption spectrum of the organic chromophores and the solar spectrum, non-ideal band alignment between the donor and acceptor species, and low charge carrier mobilities resulting from the disordered nature of organic semiconductors. To address the latter issues, we investigate the development of conjugated polymer/nanostructured oxide composite photovoltaic devices. These composites can take advantage of the high electron mobilities attainable in oxide semiconductors while using low-temperature solution-based growth techniques. Additionally, the morphology of the composite can be controlled in a systematic way through control of the nanostructured oxide growth. We develop zinc oxide (ZnO) nanostructures that are grown vertically aligned with respect to the substrate. By using doped metal oxide semiconductors as acceptors we can easily change the band offsets in these devices as well as increase the open circuit voltage

relative to traditional polymer/fullerene bulk heterojunction devices. The nature of this device structure also allows for the use of more stable electrodes such as Ag. Here we develop such nanostructures, explore their basic material properties and prepare hybrid photovoltaic devices from poly(3-hexylthiophene)/ZnO nanofiber composites.

1.1 Introduction to Photovoltaics

As the world's energy demands continue to grow and non-renewable resources are consumed, interest in the photovoltaic conversion of the sun's energy into electricity grows. The consumption of non-renewable resources is leading to a decrease in their supply and an increase in their cost as a result of more expensive extraction techniques. There are many environmental concerns connected with the consumption of fossil fuels, such as the rising awareness of emitted greenhouse gases and the encroachment of fuel extraction processes on protected wildlife refuges. Another concern associated with our continued dependence on fossil fuels is energy security. A reduction in our foreign fuel dependence and a change from centralized to distributed power could lead to an increased level of homeland security. These factors result in favorable economic conditions for solar cell technologies.

However, the overwhelming problem with the application of solar cells has been their cost. Though their prices have decreased dramatically over the years, commercial solar cells still fall short of having the competitive prices needed to be an economically viable alternative to traditional on-grid power generation. Traditional inorganic solar cells have achieved high efficiencies and very stable performance with device lifetimes reaching 20 to 30 years. However, the processing techniques and the materials used to manufacture these devices are energy intensive and expensive. Although the cost of these modules is decreasing, the current cost ≤ \$4/W_p (peak watt) is too high to significantly influence energy production as seen in Figure 1.1.[1, 2] Until this price

becomes competitive with fossil fuels at values closer to \$0.33/W_p, solar technologies will only be used in niche markets where distributed fuel costs are higher. This is not likely to change unless the cost of fossil fuels increases dramatically from their present levels. Significant changes in either processing techniques, materials selection, or a change in technology are needed for photovoltaics to become an economically viable option for large-scale energy production.

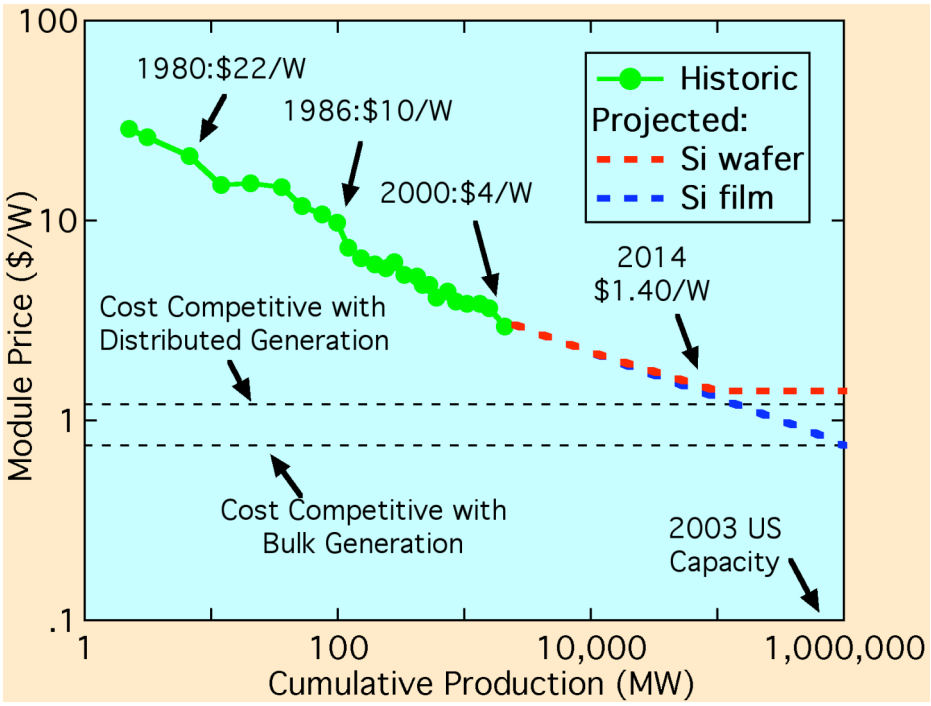

Figure 1.1 Historical and projected costs for crystalline and thin film silicon photovoltaic modules versus there cumulative production.[1, 2]

1.2 Organic Photovoltaics

Photovoltaics have a long history with the first silicon solar cell being developed over 50 years ago. However, their utilization for large-scale energy production has been limited due to large fabrication and material costs. A goal for more widespread application of photovoltaics would be to develop solar cells with moderate efficiency (15–20%) at a very low cost. Achieving this will require inexpensive materials for the active components, substrates and packaging, while allowing for low-temperature atmospheric processing techniques and high fabrication throughput. Organic-based photovoltaics have potential to make a significant impact. Organic photovoltaics have a theoretical efficiency equivalent to conventional semiconductor devices[3] and a cost structure derived from plastic processing.[2] As a result, organic photovoltaics may offer the long-term potential of achieving a PV technology that is economically viable for large-scale power generation.

There are many potential advantages to using organic materials for PV devices. Organics are inherently inexpensive and use low temperature processing techniques that most often take place at atmospheric pressure. This allows them to be deposited readily on plastic substrates through printing techniques in a roll-to-roll process. Organic materials can be used in very thin film device architectures because their optical absorption coefficients are very high. As a result, most of the incident light can be absorbed in only a few hundred nanometers of material. These processing techniques that can be employed in the manufacturing of solution-processed organic devices require less capital investment, can be easily scaled up, and can be printed at higher speed than those for current technologies.[4]

For comparison, a typical inorganic silicon solar cell plant production with a 30 cm wafer process can produce a maximum area of 88,000 m^2 per year. However, a typical printing press used in polymer processing can produce at least 1 meter of a sheet of printed film per second. Therefore polymer active area could be produced almost

1000 times faster than inorganic silicon.[5] When we consider the potential decrease in material costs combined with the increased output and reduced costs of production, organic solar cells could be produced significantly below $1/W, which would make them quite competitive in today's energy market.[5] If 15% efficient devices could be made at $50/m^2, then the cost per peak watt would be $0.33/W, which is competitive with present fossil fuel-based energy production.

Organic semiconductors are also very versatile in their development. The synthesis methods used for the development of organic materials is extremely flexible, allowing for the tailoring of a wide range of properties including their molecular weight, optical band gap, molecular orbital energy levels, solubility, wetting properties and structural properties. The ability to design and synthesize materials with specific absorption and electronic properties allows the integration of these materials into a variety of device architectures including organic-organic and organic-inorganic composites.

1.3 Organic vs. Inorganic Semiconductors

Photoexcitations in organic semiconductors are inherently different than those in conventional inorganic semiconductors, largely due to the weak intermolecular interactions and the disordered arrangement of molecules in the material. These result in the relatively low dielectric constant of these materials. The intermolecular forces that are employed in organic solids are often van der Waals or dispersion forces. As a result of the weak interaction between molecules, light absorption in an organic semiconductor results in the formation of a neutral mobile excited state. However, light absorption in an inorganic semiconductor often leads to the immediate formation of free carriers throughout the bulk based on the exponential decrease of the incident light intensity and the smaller exciton binding energy.

This excited state, known as an exciton, can be viewed as an electron–hole pair that is bound together by coulombic forces.[6-9] The energy required to dissociate the exciton is referred to as the exciton binding energy. In inorganic semiconductors this energy is generally smaller than the thermal energy (kT) at room temperature. However, the exciton binding energy in organic semiconductors is most often larger than kT.[10, 11] As a result, excitons must dissociate through a non-thermal process in order for a significant number of free carriers to be generated. Dissociation can occur in the presence of high electric fields greater than 10^6 V cm^{-1}[12] at a defect site in the material,[6] or at the interface between two materials that have a sufficient offset in their energy levels (band offset).[13] The exciton binding energy in a typical conjugated polymer such as poly(3-hexylthiophene) (P3HT) is 0.44 eV as determined by the difference in the optical and electrical band gaps in P3HT.[14] Similar measurements have established a binding energy of 0.4 eV for poly(*p*-phenylene vinylene) (PPV).[11] The offset of the energy levels between the P3HT or PPV donors and the 3-phenyl-3H-cyclopropa[1,9][5,6]fullerene-C_{60}-I_h-3-butanoic acid methyl ester (PCBM) acceptor can be viewed in an energy level diagram as seen in Figure 1.2. In these donor-acceptor pairs the offset can be estimated at 0.9 eV, which is much larger than the exciton binding energy in either P3HT or PPV. Due to this large band offset, very efficient exciton dissociation has been observed in both P3HT-PCBM and PPV-PCBM systems.

A photogenerated exciton can diffuse to an interface where the electron affinities and ionization potentials are different in the two materials. If the difference in energy levels is larger than the exciton binding energy, the exciton can be dissociated, leading to either electron transfer to the material with higher electron affinity or hole transfer to the material with the lower ionization potential. Most often the majority of the light is absorbed in the donor material. As a result, the dominant charge transfer process that is utilized in organic photovoltaic devices is electron transfer from the material with low electron affinity to the material with a higher electron affinity. However, the opposite process of hole transfer from the electron acceptor to the donor material is also an

efficient process and is employed in a number of devices where both the acceptor and donor as light absorbers.

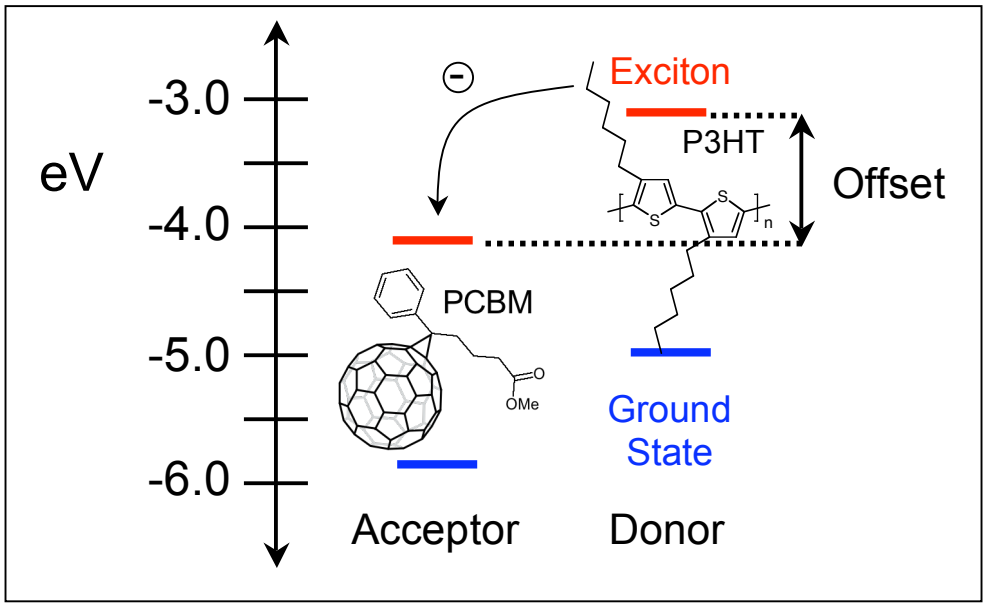

Figure 1.2 Energy level diagram for the conjugated polymer donor (P3HT) and e^- acceptor (PCBM) showing electron transfer from P3HT to PCBM.

Organic semiconductors can be roughly categorized as either small molecules, with molecular weights of less than a few thousand atomic mass units (amu), or polymers, with molecular weights greater than 10,000 amu. Small molecule organic semiconductors typically need to be thermally evaporated, as they do not easily form quality thin films from solution. Polymer organic semiconductors, however, more easily form high quality films using solution-processing methods. The fundamental mechanisms for the optical and electronic properties of the different classes are identical.

The highest occupied molecular orbital (HOMO) and the lowest unoccupied molecular orbital (LUMO), largely determine the optical and electronic properties in organic semiconductors. The HOMO and LUMO energy levels in disordered organic semiconductors are delocalized molecular energy states that usually exist over single polymer chains. This is unlike the typical energy band levels in inorganic semiconductors that are delocalized over the entire periodic crystal lattice of the material. Therefore, in both small molecules and polymers, charge carrier transport relies on thermally activated hopping between molecules. Generally, the charges are localized to a single molecule due to the poor overlap of the molecular orbitals between adjacent molecules.

Charge transport in organic molecular solids does not follow true band transport, which occurs in conventional, inorganic semiconductors that are hindered by phonon scattering in the crystal lattice. Evidence for band transport has been demonstrated in single crystal small molecules materials such as pentacene. However, the majority of work on organic semiconductors to date has been on disordered materials, where the carrier mean-free path is found to be less than the lattice constant of the molecular solid.[15] Therefore, the band model is not a reasonable model as the charge is localized to single molecules. The model that does work to describe the transport properties in these amorphous materials is the disorder formalism.[16-18] This model is based on a hopping mechanism for charge transport, where the activation energy for the hopping between molecules is dependent on the site energies related to orientational and positional disorder.

1.4 Challenges with Organic Semiconductors

There are a variety of issues to be overcome with organic electronics. One of the issues associated with organic electronics is their lack of stability when exposed to air,

moisture, and photoexcitation. Organic semiconductors can show very good environmental stability and resistance to photo-oxidation. An encouraging indicator for the stability of organic-based solar cells is the increasing lifetimes under high injection currents found in organic light-emitting diodes (OLEDs), where lifetimes of 46,000 hours have been demonstrated.[19] Device degradation can be largely a function of morphological changes, loss of interfacial adhesion, and inter diffusion of the components, rather than from chemical decomposition, assuming that an encapsulation scheme is employed to protect the device from exposure to both oxygen and water. Even with these current limitations in device stability, reasonable lifetimes have already been achieved. Organic photovoltaic devices crudely encapsulated between two glass slides have demonstrated half-lives of over 2000 hours at an elevated temperature of 85 ºC.[5] It is reasonable to expect that with proper materials engineering and improved device architectures the lifetimes can improve significantly.

In particular, it is the small exciton diffusion length that presents a challenge in device design. Exciton diffusion lengths of most polymeric semiconductors are on the order of 3 to 20 nm.[20-24] Excitons diffuse from one molecule to the next through an energy transfer. When a transition is dipole forbidden an electron exchange mechanism (Dexter) dominates.[15] Förster energy transfer occurs due to a dipole-dipole interaction between the exciton donor and acceptor molecules.[25-27] The maximum distance over which Förster energy transfer can occur is 3 to 5 nm. This mechanism occurs efficiently when the donor fluorescence and the acceptor absorption spectra overlap significantly. The exciton hops to a neighboring molecule with the energy level closest to its initial one. After hopping, the energy of the exciton decreases due to structural relaxation as a result of the induced dipole in the environment around the exciton. As the exciton migrates toward the dissociation site, its energy is reduced. Therefore, the exciton diffusion slows down over time as lower energy sites are occupied.

The exciton diffusion length in conjugated polymers is short due to both a short lifetime of about 1 ns[14] and the dispersive migration of the exciton to lower energy sites.

The exciton diffusion length is a function of the conjugation length that exists in the polymer chain and the intermolecular ordering of the molecules with respect to each other. Both of these factors have a dramatic effect on the HOMO and LUMO positions in a given polymer chain, which directly affects the energy of that site in the exciton diffusion process.[20] If the polymer chains are made more rigid, the conjugation length as well as the intermolecular ordering is likely to increase. This can increase the diffusion length of the excitons through a decrease in the energy lost through the exciton migration process and the formation of lower energy states that would help to provide additional hopping sites for further exciton migration. If the conjugation length in a particular polymer chain is increased then a lower energy site is established due to enhanced delocalization of the electron density over the molecule. Therefore, if the polymer ordering can be enhanced toward the dissociation interface, the exciton diffusion may be directed toward that interface resulting in enhanced exciton diffusion lengths.

Efficient organic photovoltaic devices must have architectures that allow for efficient dissociation of photogenerated excitons in the active layer into electrons in the acceptor material and holes in the electron donor material. As discussed above, the exciton will only be efficiently dissociated at an interface between materials with a sufficiently large band offset. Because of the short exciton diffusion length, the interface must be ≤10 nm from any location at which an exciton is generated if high carrier generation efficiencies are to be achieved. An important development in organic photovoltaic devices occurred with the observation of extremely fast photoinduced electron transfer from a conjugated polymer to buckminsterfullerene (C_{60}).[28] The forward electron transfer rate was measured to be 45 fs,[29] whereas the reverse recombination rate of separated electrons with holes has been measured as greater than 300 ns.[30] The discovery of electron transfer from a polymer to a fullerene made it possible to make reasonably efficient organic solar cells and provides the basis for a large portion of the devices studied today. As discussed later, the reason that a bulk heterojunction polymer/fullerene blend device works as well as it does is due to the fact

that the majority of the excitons are efficiently dissociated, as seen through photoluminescence quenching data presented in Figure 1.3.[31] In order to maximize the device performance, nanometer scale phase separation can be introduced into the donor/acceptor composite, thereby dissociating all of the excitons and generating separated charge carriers. This can be monitored effectively with photoluminescence studies of various donor/acceptor materials and architectures.

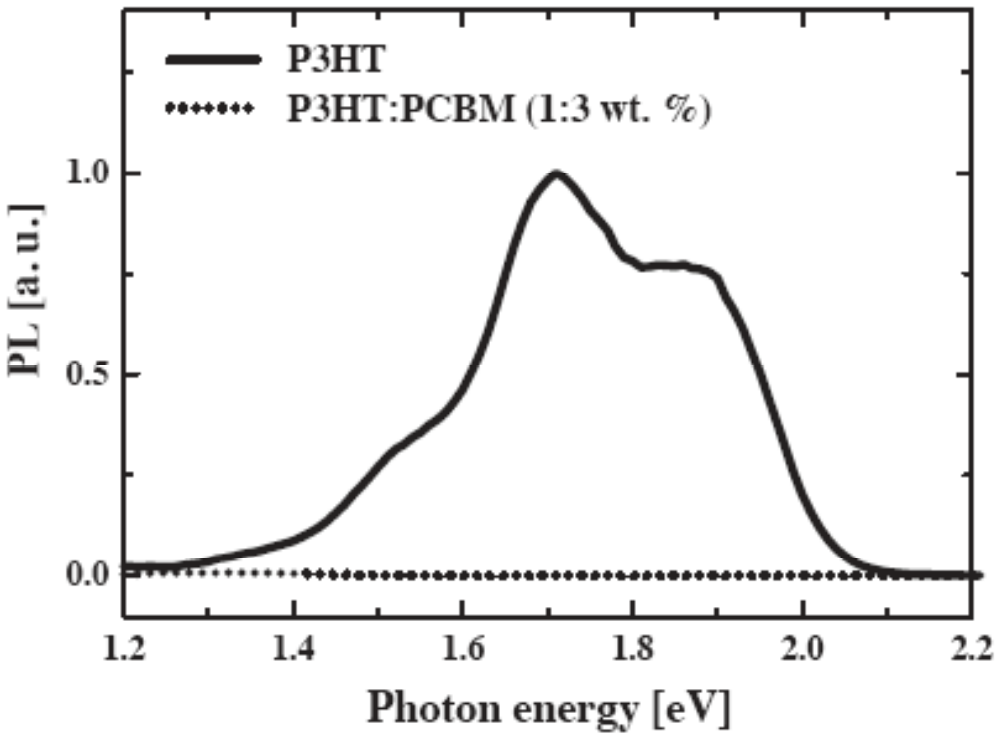

Figure 1.3 Photoluminescence spectra of P3HT film (solid line), and 1:3 P3HT:PCBM blend film (dotted line).[31]

A key advantage of using a heterojunction device architecture, apart from the necessary band offset, is the physical separation of charges through separate charge transport pathways. Opposite charges are transported through different materials, thus dramatically reducing the recombination rate through the special separation of electrons and holes. If electrons and holes were to travel through the same material they would have an increased possibility of recombining. By separating them into different materials, the probability of the charges escaping the device is increased resulting in improved device efficiency.

Another area of particular interest is the collection of the charge carriers at the electrodes. In the bulk heterojunction polymer/fullerene blends the transparent conducting oxide is coated with poly(ethylenedioxythiophene)-poly(styrene sulfonate) (PEDOT-PSS), a conductive polymer blend that helps match the work function of the electrode to the polymer semiconductor thereby reducing the resistive losses related to non-ohmic contacts. The back contact in this type of cell is often a low work function metal contact to the fullerene material. This limits recombination losses at the back contact, since high work function metals form ohmic contacts with both the fullerene and the polymer phases, resulting in enhanced surface recombination.[32] While high work function contacts will result in a functional device, the enhanced recombination leads to poor device performance. In order to preserve much of the voltage developed in the cell, metals with low work functions such as Al or Ca are used as seen in Figure 1.4. This also helps to establish an asymmetry and selectivity in the work function of the contacts, dictating the direction of current flow in the device through the introduction of a built-in field in the device after contact as seen in Figure 1.4. However, the use of low work function metals as contacts may lead to stability concerns due to the increased oxidation rate of these metals.

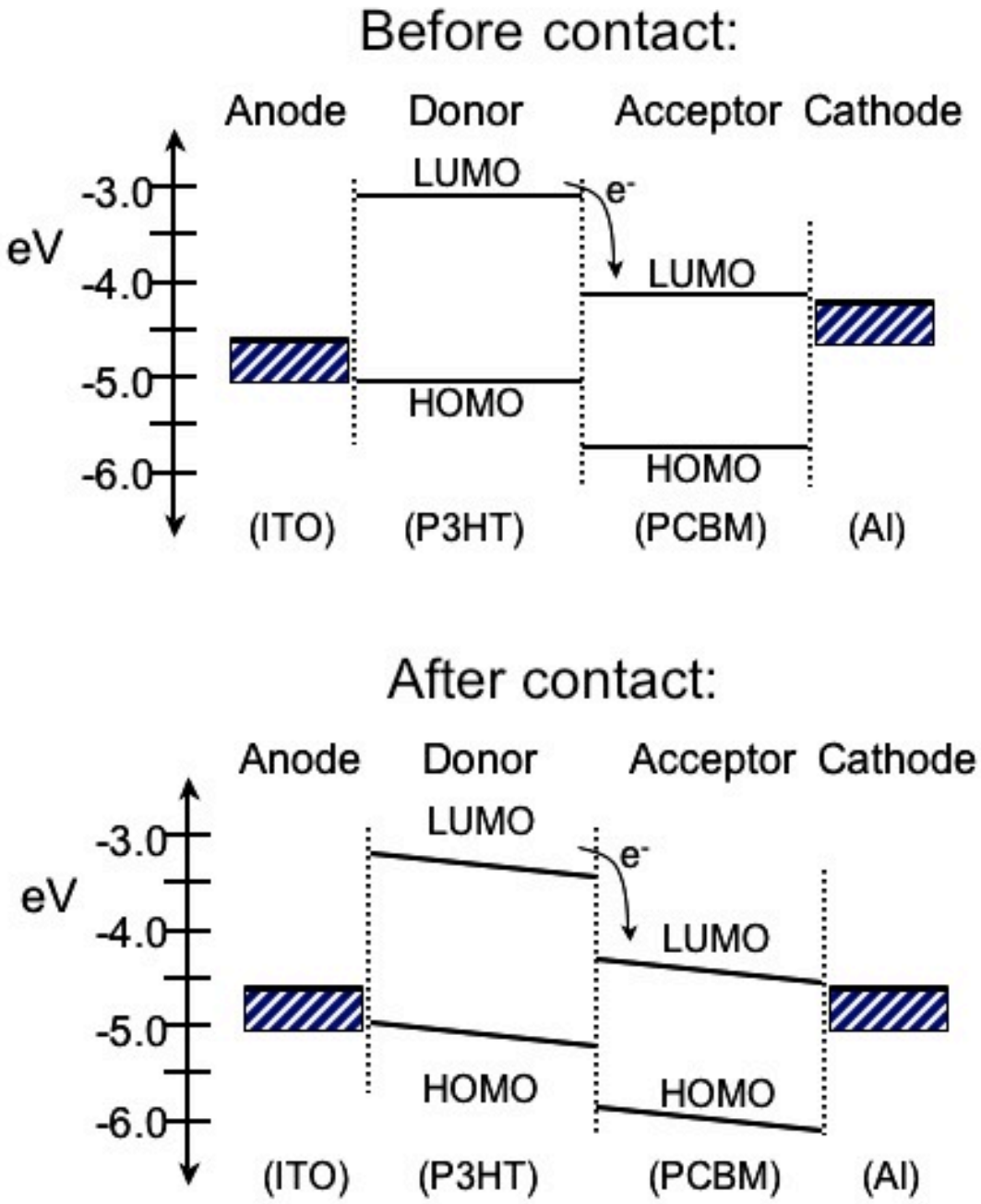

Figure 1.4 Band diagram showing bulk heterojunction device with electrodes. Top diagram shows before contact (not at equilibrium). Bottom diagram shows after contact (at equilibrium).

To make these devices more stable under ambient conditions, high work function metals can be employed as the back contact. In order for such a device to operate efficiently, it must run in the reverse direction as shown in Figure 1.5. Holes would then need to flow out through the top (back) contact and electrons out through the transparent conducting oxide. This can be accomplished if an electron acceptor material is first deposited onto the transparent conducting oxide, which has been demonstrated for a polymer/TiO_2 system in which the indium tin oxide (ITO) is coated with TiO_2, filled with a conjugated polymer, and completed by evaporation of a gold back electrode.[33] The blend can also be deposited onto an electron acceptor and a high work function metal can be used as the back contact to the cell. This has been demonstrated and shown to work quite well,[34] though increased stability of such a device has yet to be established. In such devices, carriers move through diffusion currents based on a chemical potential gradient, not through drift currents induced by a built-in electric field as seen in the devices in Figure 1.4. Efficient solar cells can be made that rely strictly on the chemical potential gradient for the movement of charges as all dye sensitized solar cells demonstrate, rather than relying on a built-in field that moves charges in traditional inorganic PV devices.

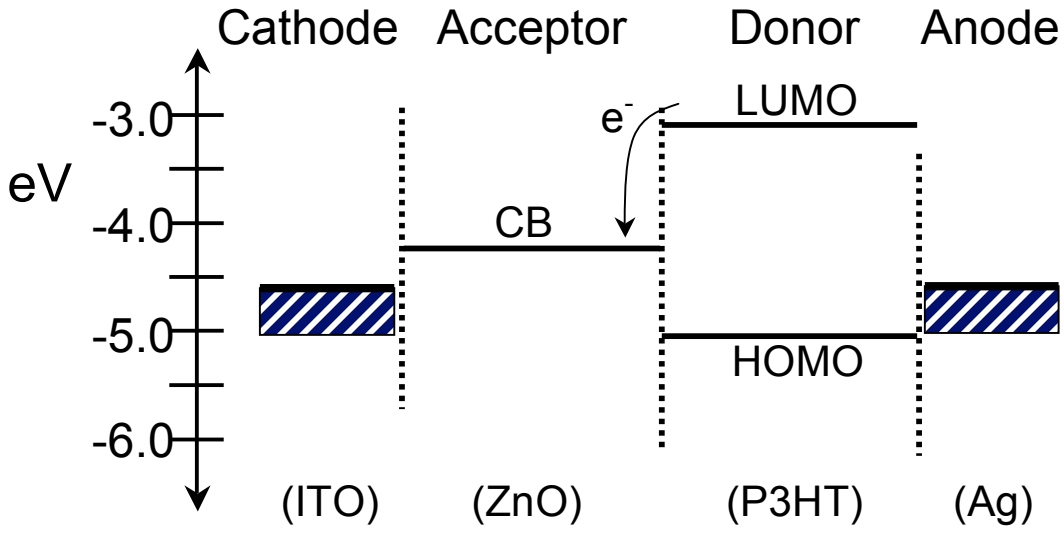

Figure 1.5 Band diagram showing inverted heterojunction device with contacts.

As mentioned above, one of the key advantages of using organic semiconductors is that they have very high absorption coefficients, such as 1. 8 x 10^7 m^{-1} for poly[2-methoxy-5-(3',7'-dimethyloctyloxy)-1,4-phenylene vinylene] (MDMO-PPV) at a λ_{max} of 505 nm,[35] and absorb most of the incident light in only a couple hundred nanometers of material. An optical density of over 2.0 for a 230 nm P3HT film thickness results in an absorption coefficient of 2 x 10^7 m^{-1} at a λ_{max} of 520 nm as seen in Figure 1.6. A large amount of light can be absorbed in a very thin film, however the low mobilities (10^{-4} $cm^2/v*s$) in these organic materials lead to charge recombination when the film gets too thick. As a result, the active layers in OPV devices are made very thin (≤ 200 nm) to maximize their efficiency thereby reducing the amount of light that they absorb.

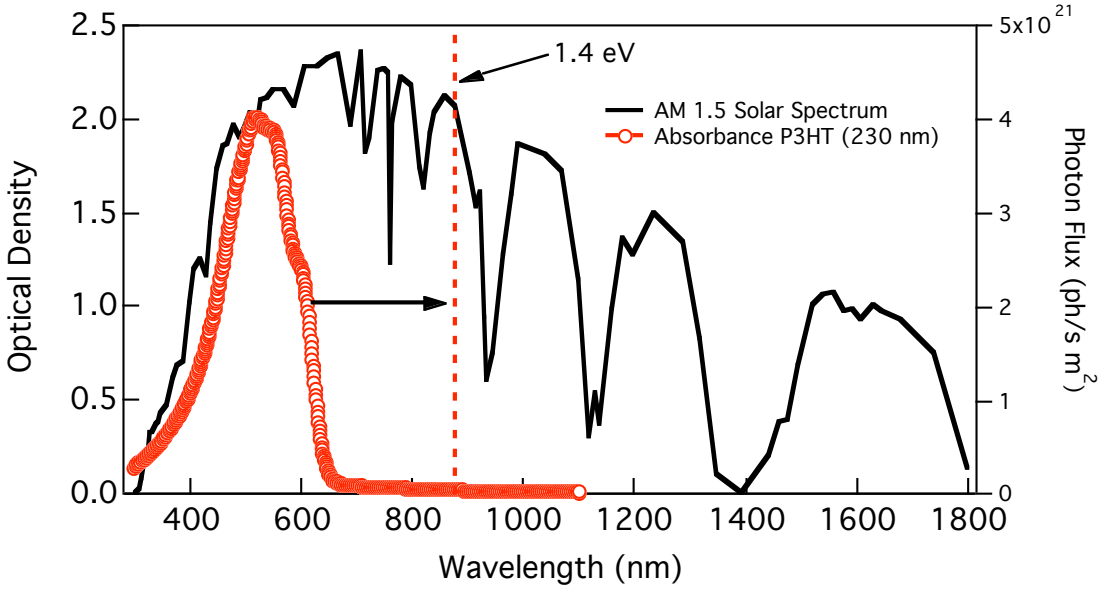

Figure 1.6 AM 1.5 solar spectrum and absorption of P3HT as a function of wavelength.

In addition, Figure 1.6 also demonstrates that the band gap of the absorbing material needs to be decreased dramatically. The band gaps of most of the polymeric semiconductors employed in photovoltaics to date have typically been greater than 1.9 eV. This limits their absorption to the visible part of the solar spectrum and reduces their achievable efficiency, as they can only absorb about 30% of the incident light. If the band gap is reduced closer to the optimal theoretical value of 1.4 eV as indicated in Figure 1.6, more of the incident light would be absorbed and the efficiency could increase accordingly. This is a parameter that needs ongoing development, as it is a large part of the reduced efficiencies observed in organic solar cells to date. This limitation will not be addressed in this thesis. Instead, this thesis will focus on the design, fabrication, and morphological issues related to hybrid organic/inorganic photovoltaic devices.

1.5 Organic Photovoltaic Device Architectures

There are a number of device architectures that each address certain aspects of the challenges faced when fabricating organic photovoltaic devices (OPVs). The architectures can vary from simple planar bilayer heterojunction structures to nanostructured, easily fabricated blended bulk heterojunction devices as discussed briefly in the last section. Both architectures address some of the unique constraints that organic semiconductors put forth.

1.5.1 Bilayer Heterojunction Polymer Photovoltaic Devices

Planar bilayer heterojunction devices can be made out of donor and acceptor species as seen in Figure 1.7. The first efficient organic solar cell consisted of a phthalocyanine/perylene bilayer deposited by thermal evaporation, which resulted in an efficiency of about 1%.[36] Such devices efficiently separate charge carriers at the interface between the donor and acceptor materials, and subsequently the charges travel in opposite directions through the different materials to the appropriate electrodes. This effectively reduces the recombination rate by limiting interactions between electrons and holes. Planar heterojunction devices using a conjugated polymer and fullerene can be easily fabricated using solution and thermal deposition processes resulting in relatively low efficiency devices.[24, 37] Since the exciton diffusion length in conjugated polymer semiconductors is ~10 nm, the thickest the collection layer in the device can be is on the order of 20 nm. Material outside of this region only results in excitons photogenerated far from the heterojunction where they cannot easily be dissociated.[24, 38] When this is combined with low carrier mobilities, the active layer thickness in the bilayer device must be kept relatively thin to allow for efficient charge collection. Such devices are limited in their optical density and in turn their power conversion efficiency. Despite their

limitations, bilayer devices provide a relatively simple geometry from which models can be more easily developed. In addition, bilayer devices also provide straightforward methods for testing different material compositions for photovoltaic applications. Therefore, there are a number of applications of the bilayer device geometry in this thesis.

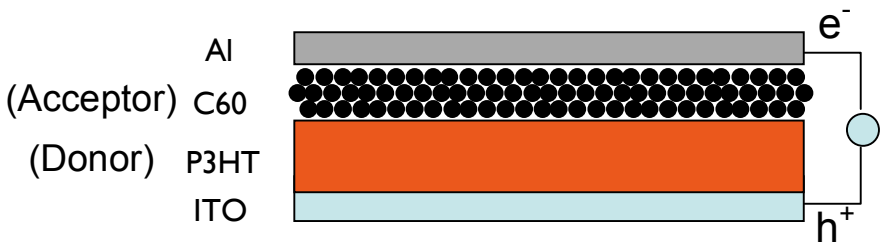

Figure 1.7 A cartoon interpretation of a planar bilayer heterojunction OPV device fabricated by thermal evaporation.

Multijunction devices can be fabricated relatively easily through vacuum deposition methods. Such devices allow for both the use of multiple layers of very thin absorbers to allow for efficient exciton dissociation in each layer while multiplying the overall V_{OC} of the device by the number of active layers.[39] Neighboring layers can be interconnected by a thin, non-continuous Ag film, which serves as an efficient recombination site for the electrons and holes from adjacent devices. Multilayer devices based on donor molecules with sufficiently large exciton diffusion lengths have reached very high efficiencies as a result of the higher theoretical efficiency of tandem and multijunction solar cells.[39, 40] Due to the increased complexity of the device fabrication process, multijunction devices are more expensive than other polymer PV devices.

1.5.2 Bulk Heterojunction Polymer/Fullerene Photovoltaic Devices

Instead of using a planar heterojunction, the donor and acceptor materials can be combined and cast to form a blend through spin coating from a single solution. A blended architecture provides a large interfacial area between the donor and acceptor materials as illustrated in Figure 1.8. This creates a bulk heterojunction where the intimate mixing of donor and acceptor species results in excellent exciton dissociation where any photogenerated exciton is within a diffusion length of an acceptor molecule leading to charge generation. Therefore, charges can be generated everywhere in the bulk, which dramatically increases the volume of the photoactive layer. If continuous pathways exist in each material from the bulk to the electrode, the efficiency can increase dramatically. Bulk heterojunction devices can be very cost effective solution-processed devices. Initially, polymer/C_{60} bulk heterojunction devices were fabricated and demonstrated improved photovoltaic performance over equivalent bilayer devices.[38] However, C_{60} is relatively insoluble in the solvents used for casting the polymer films. In addition, C_{60} forms large crystal domains, thereby reducing the intimate contact between the donor and acceptor, which is necessary for large internal quantum efficiencies. As a result, the synthesis of more soluble forms of C_{60} such as PCBM lead to significant increases in efficiency.[38]

The most successful polymer based photovoltaic cells to date are of this type, with efficiencies approaching 5% being reported using a conjugated polymer and fullerene derivatives. For example, current state-of-the-art OPV devices based on composite blends of a conjugated polymer, such as poly(3-hexylthiophene) (P3HT), and a fullerene (PCBM) have exhibited solar power conversion efficiencies greater than 3%.[41-43] These devices rely on ultra-fast photoinduced charge transfer between the P3HT donor and the PCBM acceptor to dissociate excitons created anywhere in the bulk of the film.

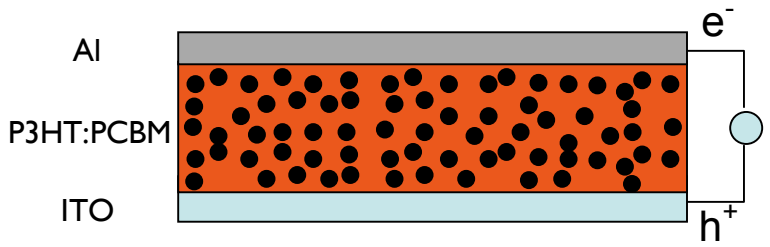

Figure 1.8 A cartoon interpretation of the main components of a polymer/fullerene bulk heterojunction OPV device fabricated by spin coating from a single solution.

The morphology of the polymer/fullerene blend plays a very important role in determining the device performance. The blend morphology can be significantly modified through careful solvent selection resulting in control of the phase separation. Spin coating the film from chlorobenzene instead of toluene as an example, can improve the device performance from 0.9% to 2.5% in MDMO-PPV/PCBM bulk heterojunction devices through the formation of nanodomains in the composite layer.[44, 45]

The donor/acceptor ratio can have a dramatic effect on the device performance as well through its effect on the percolation of molecules for charge transport and on exciton dissociation through nanoscale phase separation.[45, 46] The ratio is dependent on the donor/acceptor pair being investigated, with thiophene donors requiring significantly less PCBM than PPV systems.[47] The ratio must be optimized to eliminate large domain phase separation after thermal annealing and interface damage in P3HT/PCBM thin films through the formation of disruptive crystalline PCBM grains.[43, 47]

The thermal stability of the morphology of such blends may be an issue, as the glass transition temperature of these materials can be well below 200 ºC.[48] There is evidence, however, that the blends become more thermally stable after a post fabrication thermal anneal induces beneficial phase separation. In several devices based on P3HT as the electron donor, thermal annealing is necessary in order to achieve increased performance.[41-43] Increased intermolecular ordering of polythiophenes has been

demonstrated to shift the absorption to lower energies. This effect has been observed in both polymer solutions and thin films where the band edge shifts in excess of 100 nm are observed as a result of the formation of a shoulder in the absorption spectrum at 620 nm.[47, 49] This red shift is believed to be the result of a transition from coil to rod-like structures in the polymer chains.[50-53] Therefore, the morphology and intermolecular ordering of P3HT can be characterized to some extent through the measurement of the absorption spectra of the composite devices.

Recent work on thermal annealing of the P3HT/PCBM blends has resulted in the formation of nanocrystalline domains upon annealing, which have been identified in x-ray diffraction measurements.[43, 54] Another demonstration of increased intermolecular order in the performance of P3HT-based devices has been established when the composite film is formed more slowly, giving the polymer and fullerene more time to organize prior to the film drying.[42] If a higher boiling point solvent is used, such as dichlorobenzene, the film will take longer to dry. When the spin speed is reduced and the films are placed in a closed vessel to dry slowly, similar results can be observed without extensive post-production annealing. The result is a more ordered film, where the mobility of both charge carriers can be increased dramatically, and a thick composite film can be made that demonstrates a low series resistance and a conversion efficiency greater than 4%.[42]

Other acceptor materials, such as 3-phenyl-3H-cyclopropa[8,25][5,6]fullerene-C-D(6)-3-butanoic acid methyl ester ([70]PCBM) have been investigated to increase the absorption of the acceptor material in the visible part of the solar spectrum. If C_{70} is substituted for C_{60}, there is a change in molecular symmetry. In C_{70} or [70]PCBM, optical oscillator strengths are stronger, leading to increased absorption. This results in an increase in the quantum efficiency in the visible part of the spectrum in MDMO-PPV blend devices. In addition, there is a 50% increase in the short circuit current density and an increase in efficiency over MDMO-PPV/PCBM bulk heterojunction devices.[55] However, due to the increased cost of C_{70}, most devices are fabricated with C_{60}-based

acceptors such as PCBM. Devices using lower band gap donors such as poly(N-dodecyl-2,5-bis(2'-thienyl)pyrrole, 2,1,3-benzothiadiazole) (PTPTB) have been fabricated as well, using a blend with PCBM, and resulted in an increase in the red response out to almost 800 nm. These devices, however, demonstrated reduced efficiencies of about 1%.[56] These results are important for the development of blend devices with higher efficiencies. However, they do not address the important aspect of morphology.

As discussed above, the morphology of the donor-acceptor blend in these systems has proven to be critical to their operation. In order for separated charge carriers to exit the device, there must be percolation of the acceptor and donor molecules to the correct electrode. Without a percolation pathway, charges can be trapped without a path to the correct electrode leading to recombination and reduced efficiency. This also effectively limits the thickness of the device, reduces the amount of light absorbed and decreases the efficiency. Defects in the network represent significant challenges to increased performance. Additionally, connectivity of the correct material with the corresponding electrode is not easily controlled.

Current polymer/fullerene blend devices suffer from a variety of problems associated with these organic semiconductors. The development of high efficiency organic photovoltaic devices is already becoming more focused on the details and control of the morphology of the molecules and materials incorporated into these devices. These devices most often consist of disordered materials with low carrier mobilities and short exciton diffusion lengths. Control of the crystallinity in each phase of the system has become increasingly important for the optimization of the material parameters that affect device performance. Presently, control of the blend morphology is dictated by the choice of solvent, casting conditions and thermal annealing either prior to or after deposition of the counter electrode. Often, these do not secure the nanoscale phase separation and molecular percolation characteristics that are necessary for optimum device performance. With changes in the materials incorporated, the morphology must be re-optimized.

1.5.3 Bulk Heterojunction Polymer/Inorganic Nanoparticle Photovoltaic Devices

Bulk heterojunction devices consisting of a blend of a conjugated polymer with nanocrystals of conventional semiconductors such as CdSe have been fabricated and demonstrate efficiencies around 1.7%.[57] The nanoparticles can be synthesized with a variety of sizes and shapes, as seen in Figure 1.9. When compared to the polymer/fullerene blends described above, these systems can provide light absorption in the acceptor species as well, thereby increasing the optical density of thin films of such blends. The band gap of inorganic nanoparticles can be tuned by constraining the size of the particles. For example, the band gap of CdSe can be adjusted through quantum confinement.[58] The interface between the organic donor and inorganic acceptor materials must be optimized to maximize performance. The alignment between the molecular orbitals and the bands of the inorganic material must be optimal if electron or hole transfer is to occur efficiently. The band offset can be controlled in these systems by changing the band gap of the particle through changes in the nanoparticle dimensions. The band offset can be reduced as the band gap of the CdSe nanoparticles is increased. As a result, the conduction band of the acceptor is moved closer to vacuum resulting in an increase in the photovoltage.[59] However, it was observed that with an increased band gap of the CdSe nanoparticles, the current density of the device was reduced resulting in lower power conversion efficiencies.

The inorganic nanoparticles, while having better bulk transport properties than PCBM, suffer from low mobilities of 10^{-6} to 10^{-4} $cm^2V^{-1}s^{-1}$ in polymer/inorganic nanoparticle blends, due to a charge transport process based on a hopping mechanism.[60, 61] CdSe nanorods were synthesized and utilized in order to improve the charge transport characteristics of the CdSe nanoparticles. It was concluded that CdSe nanorods with dimensions of 7 x 60 nm demonstrated higher performance than either shorter 7 x 30 nm nanorods or spherical CdSe nanoparticles with diameters of 7 nm. The increase in current density in the longer CdSe nanorods is likely the result of enhanced electron

transport through the long axis.[57] This points towards single crystal nanorods as an improved morphology for enhanced carrier transport and efficiency in OPVs. In these P3HT/CdSe nanoparticle bulk heterojunction devices it was observed that a mixture of chloroform with pyridine resulted in increased performance over a single solvent.[62] Hybrid polymer/inorganic nanoparticle blends suffer from the same morphological issues, however, as the polymer/fullerene bulk heterojunction devices above. Hence, solvent selection becomes an important processing parameter in the development of higher efficiency devices.

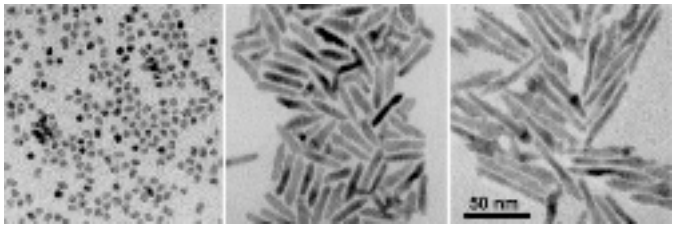

Figure 1.9 Transmission electron microscope images of cadmium selenide nanocrystals.[57]

A cartoon illustrating the polymer/inorganic nanoparticle device is shown in Figure 1.10, indicating an architecture similar to that of the polymer/fullerene bulk heterojunction devices. Photoinduced charge transfer has also been observed from a conjugated polymer donor to a number of metal oxide acceptors such as SnO_2, TiO_2, and ZnO.[23, 63] The main concern when choosing a donor-acceptor pair is obtaining a fast forward electron transfer with a much lower probability backward electron transfer process, which allows the charge to be extracted from the device prior to recombination of the charge carriers. This has been demonstrated for conjugated polymers and metal oxides, where the forward electron transfer rate is less than 100 fs, and the recombination

rate, which includes both backward electron transfer and recombination, is greater than 1 ns.[63] These electron transfer kinetics ensure that the exciton will be dissociated and the carriers will begin to diffuse away from the interface before any significant recombination occurs. While the electron mobility in nanoparticle ZnO can be rather high in pure nanoparticle films ($\mu_e \sim 10^{-2}$ $cm^2V^{-1}s^{-1}$),[64] in a polymer/nanoparticle blend that value may be reduced to values similar to polymer/fullerene blends.

Devices based on composites of metal oxide semiconductor nanoparticles embedded in a conjugated polymer matrix have been developed and have demonstrated reasonable efficiencies approaching 2%.[35, 65-67] Devices based on ZnO nanoparticles perform better than TiO_2-based bulk heterojunctions, which is presumably due to easier dispersion and crystallization of ZnO nanoparticles.[33, 66] These devices have demonstrated the feasibility of hybrid polymer/metal oxide composites for photovoltaic applications. Also, these devices perform comparably to the polymer/CdSe bulk heterojunction devices mentioned above, though the metal oxide acceptor has a large band gap (3.2 eV) and therefore does not contribute to light absorption in the device.

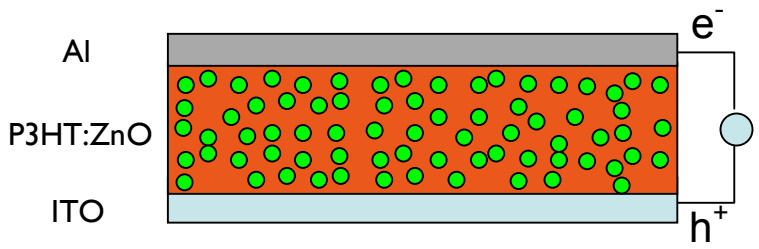

Figure 1.10 A cartoon interpretation of a polymer/inorganic nanoparticle bulk heterojunction OPV device fabricated by spin coating from single solution.

1.5.4 Ordered Hybrid Polymer/Nanostructured Oxide Composite Devices

Ordered organic/inorganic hybrid bulk heterojunction devices might be a means to combine a light absorbing conjugated polymer donor species with an electron acceptor that demonstrates control over the nanostructured morphology through the directed growth of a nanostructured metal oxide.[2, 68] Such a device would operate similar to a bulk heterojunction device based on a blend of donor and acceptor molecules, however the organized growth of the nanostructured oxide would determine the bulk heterojunction morphology in the composite, as demonstrated in Figure 1.11. Models developed to investigate the ideal morphology for ordered polymer/inorganic devices, indicate that the conjugated polymer should be intercalated into an inorganic electron acceptor made up of small diameter nanostructures oriented vertically off of the substrate.[69] A key advantage of this approach over the polymer/fullerene bulk heterojunction device structure is the potential for directly controlling and tailoring the morphology of the donor/acceptor interface.

Systematic control of the donor-acceptor morphology might lead to better charge transport out of the device with connected pathways for charges to travel to the correct electrode, while maintaining efficient exciton dissociation in the composite. Devices made by incorporation of a conjugated polymer into the nanostructured oxide film may be more thermally stable over time than bulk heterojunction blend devices. Blends rely on phase separation to determine morphology and this can change at elevated temperatures, while the morphology of a polymer/nanostructured oxide composite would not be expected to change to any large extent.

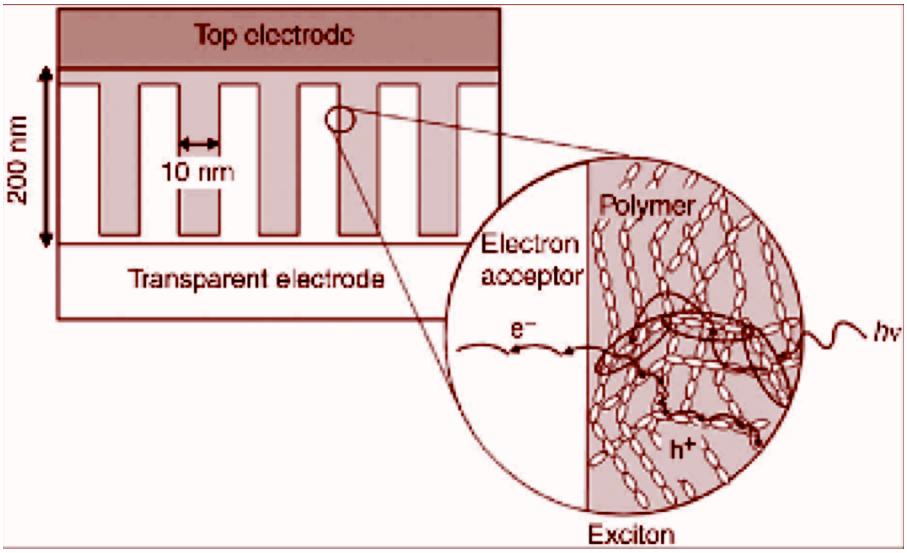

Figure 1.11 Schematic diagram of an ordered bulk heterojunction polymer photovoltaic device.[68]

A nanostructured oxide acceptor can be grown with a great deal of morphological control thanks to recent advances in growth of inorganic nanostructures. This allows for significant control in the spacing between the oxide nanostructures as well as their length or film thickness. Various metal oxide materials can be chosen, each with their own set of parameters and processes for controlled growth of nanostructures. Metal oxides can be grown with pore sizes and spacings on the order 10 nm, which would allow for efficient exciton dissociation and charge transport out of the device.[70-73] ZnO nanostructures have been fabricated from solution as seen in Figure 1.12.[72]

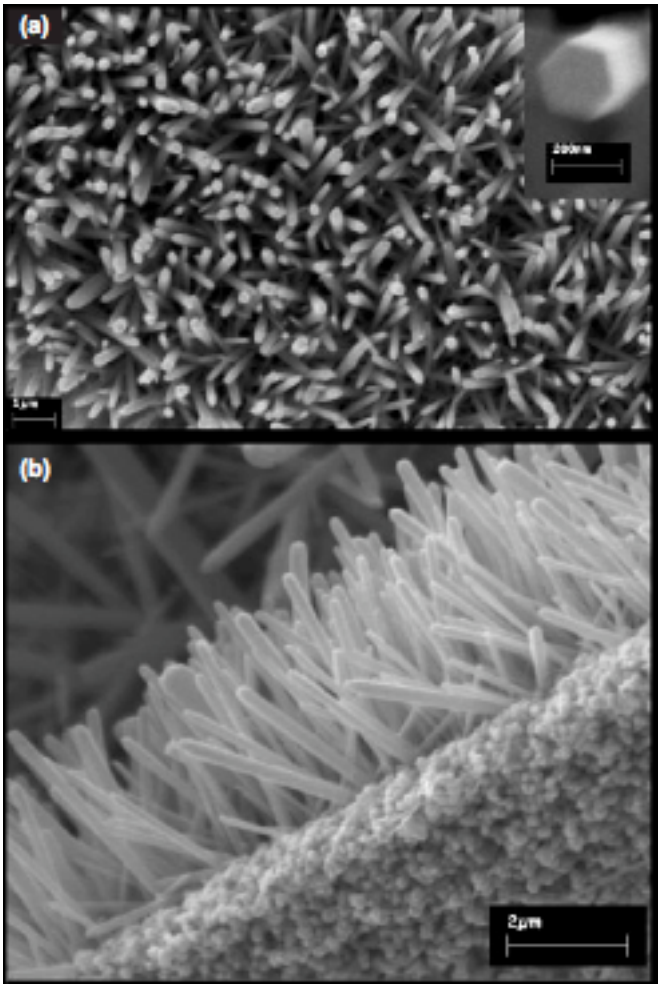

Figure 1.12 Scanning electron microscope (SEM) images of ZnO fibers grown from an aqueous solution of zinc nitrate.[72] (a) Top view. (b) Cross-sectional view.

Devices fabricated from a nanostructured oxide acceptor grown on a transparent conductive oxide will also have guaranteed percolation of both charge carrier materials. This eliminates recombination due to charges not escaping the device as a result of isolated phases of a material in the film.[68] With such a geometry, there is guaranteed percolation of both the donor and acceptor materials through the active layer. Since the metal oxide acceptor is grown directly off of the transparent electrode, it will only be

connected to the cathode and the polymer donor will only be in contact with the anode. A hybrid conjugated polymer/nanostructured oxide device might also be made thicker due to the percolation of charge carrier through the donor/acceptor materials and to the increased carrier mobility of the metal oxide semiconductor as compared to electrons in a blend.

The inverted nature of this device architecture as compared to a bulk heterojunction blend, illustrated in Figures 1.4 and 1.5, allows a high work function metal electrode to be deposited to contact the polymer and extract holes.[33, 74] The use of electrodes with similar work functions results in a device where the current is dominated by a diffusion current rather than a drift current, which is the dominate mechanism in traditional inorganic photovoltaic devices utilizing a p-n junction. This potentially eliminates the oxygen sensitive Al, Ca or other low work-function electrodes from the device structure, which has the potential to increase device stability and lessen the requirements for device encapsulation.

Ordered hybrid polymer/metal oxide devices have been fabricated using a mesoporous TiO_2 acceptor species, as seen in Figure 1.13. The material exhibits a pore size of less than 10 nm, which is less than the typical exciton diffusion length in the conjugated polymer. Significant exciton dissociation (95%) is demonstrated by PL quenching data,[73] which is anticipated with pores of this size. However, despite relatively efficient exciton dissociation and complete percolation of both species, reported efficiencies are estimated at less than 0.45% under A.M. 1.5 conditions.[75, 76]

Based on optical absorption data, the conclusion is that the conjugated polymer species is not well ordered in contrast to what is typically observed in annealed bulk heterojunction blend devices with P3HT & PCBM. This would lead to drastically reduced mobility in the P3HT and poor carrier transport properties.[75] When compared to annealed P3HT films, the absorption spectra of the intercalated P3HT is blue shifted with the shift increasing the deeper the polymer is infiltrated into the nanostructured TiO_2 film. A shoulder at 620 nm is also absent in the absorption spectra, which is often

observed for P3HT with a large amount of intermolecular ordering.[73] Additional support for the coiling of the polymer chains in the mesoporous TiO_2 stems from the decreased photoluminescence quenching observed at increased temperatures. This indicates a reduced exciton diffusion length, which is typically enhanced by molecular order.

It is likely that the reduced order in the P3HT component is related to the size and morphology of the interconnected pores in the nanostructured TiO_2 film. These pores are not vertical and are very small, leading to disordered polymer chains that coil upon themselves instead of ordered chains lying outstretched with longer conjugation lengths.[73, 75] When the polymer is more crystalline or ordered, it is expected that the charge mobility will be considerably higher, the absorption is red-shifted, and the exciton diffusion length is increased. The disordered nature of the polymer in these devices leads to a lower absorption coefficient and poor charge transport, thereby dramatically decreasing the short circuit current. Polymer films annealed for extended times at 170 ºC result in decreased hole mobility and exciton diffusion lengths. Films annealed for longer times have higher polymer optical densities in the mesoporous TiO_2 but demonstrate lower external quantum efficiencies.[75] It is thought that the oxide morphology is not ideal in this case, leading to poor intramolecular ordering. As a result, high efficiencies have not yet been realized using this mesoporous TiO_2 as an electron acceptor in an ordered hybrid solar cell.

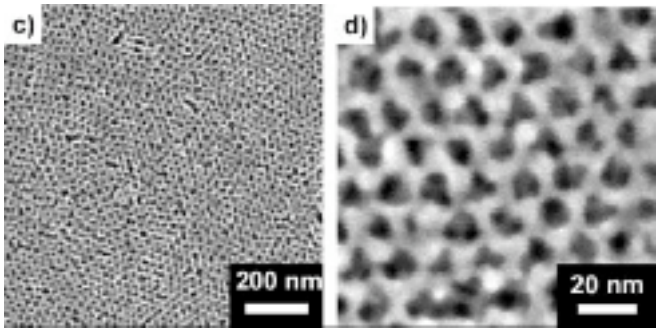

Figure 1.13 SEM image of mesoporous TiO_2 sintered from a sol-gel film of titanium tetrachloride and a structure directing block copolymer.[75]

It has recently been observed that P3HT incorporated into small vertically oriented pores in anodic alumina can lead to improved polymer hole mobilities.[68, 77] To characterize the electronic properties of the polymer in the nanoporous metal oxide, devices were prepared on fluorine doped tin oxide (FTO). The anodic alumina was deposited onto the FTO coated glass. Next, the polymer was intercalated into the porous metal oxide by annealing at 200 °C for one minute, and a gold counter electrode was thermally evaporated to complete the device, as seen in the Figure 1.14.[77] The hole mobility increased by more than an order of magnitude from 3 x 10^{-4} $cm^2V^{-1}s^{-1}$ for a P3HT thin film to 6 x 10^{-3} $cm^2V^{-1}s^{-1}$ in the charge transport direction, as estimated by fitting the space charge limited current vs. voltage data on the polymer/alumina devices.

The polymer chain orientation can be determined through polarized optical transmission and reflection measurements.[78] It has been observed that conjugated polymer chains prefer to lie in the plane of the substrate in neat films.[78] The same characterization technique was used to measure the polymer chain orientation of the P3HT in the porous anodic alumina. It was observed that the P3HT chains are partially aligned vertically along the sides of the oriented pores in anodic alumina film.[77] This is encouraging given that the charge transport direction in a photovoltaic device is in the vertical direction, normal to the substrate. Therefore, if such a structure could be made in

a nanostructured oxide such as TiO_2 or ZnO, one would expect increased mobility and in turn efficiency in ordered hybrid polymer/metal oxide devices. If the polymer chains increase in order from the middle of the pore to the side of the pore, then the polymer's exciton diffusion length might be increased leading to enhanced photovoltaic device performance.

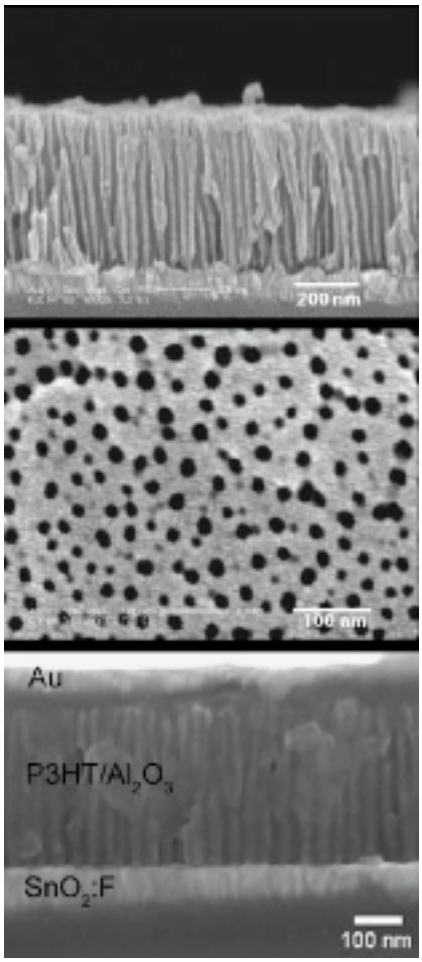

Figure 1.14 SEM cross sectional image of a porous anodic alumina thin film (top), plan view image of 20 nm pores in the anodic alumina (middle), and cross sectional image of the polymer intercalated into porous alumina with FTO and Au contacts.[77]

Another study efficiently infiltrated a number of different PPV-based polymers into a nanostructured TiO_2 film formed by sintering nanoparticles. This effort concluded that the limit in the short circuit current density of these devices is likely related to the photogeneration rate and the quality of the interfaces.[76] Neither increased polymer carrier mobility nor spectral response in the red to infrared resulted in dramatic improvements in device performance.[76] Ultimately, these devices were limited to a conversion efficiency of 0.4%, despite efforts to change the optical and electronic properties of the polymers investigated. Therefore, the current limitations of ordered hybrid polymer/nanostructured oxide devices are associated mainly with the interface between the organic and inorganic materials and the low electron mobility of the nanostructured oxide material. This is likely affected by the wetting of the polymer on the surface of the oxide as well as the complete filling of very small pores with ordered polymer chains. The low electron mobilities in the sintered TiO_2 nanoparticle films, which have been estimated at 10^{-6} $cm^2V^{-1}s^{-1}$, are much lower than the mobility in bulk heterojunction blend devices.[76]

1.6 Hybrid Polymer/Zinc Oxide Nanofiber Composite Devices

In this work, a systematically controlled device fabrication scheme is developed involving the directed nanostructured growth of a metal oxide semiconductor acceptor to dictate the device structure and nanoscale phase separation. Hybrid structures are formed, where the organic semiconductor is intercalated into an inorganic network that has significant influence on the molecular alignment. To increase the efficiencies of these hybrid devices, a promising route is to use a nanostructured oxide that is vertically aligned with respect to the substrate. Figure 1.15 shows what a composite device based on vertically aligned nanostructures might look like. This metal oxide morphology might allow ordering of the polymer chains in the vertical direction, thereby increasing the hole

mobility compared to the mesoporous TiO_2 materials described above.[76, 77] Such an architecture also has the advantage of creating electron transport pathways connected to the negative electrode that possess very high electron mobility. For example, the electron mobility of ZnO nanofibers has been measured as 10 $cm^2V^{-1}s^{-1}$, which is several orders of magnitude higher than is typically found in organic semiconductors or in sintered nanoparticle TiO_2 films.[79, 80]

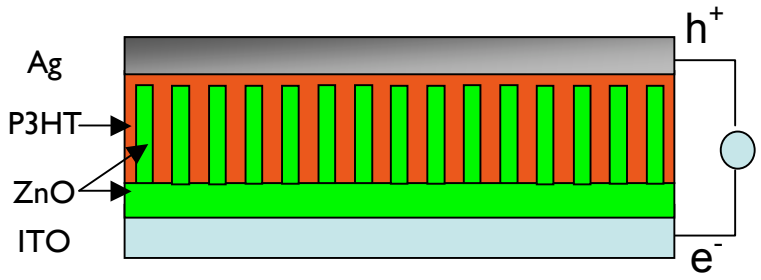

Figure 1.15 Schematic diagram of an ideal conjugated polymer/zinc oxide nanofiber photovoltaic device.

Through a low-temperature chemical solution growth technique, single crystal ZnO nanofibers that demonstrate high electron mobilities can be grown.[72, 79] The ZnO fibers grow normal to the substrate in the 002 direction as seen in Figure 1.16. However, the substrate must often first be coated with a nucleation layer for controlled growth to occur.[81] The length of the fibers can be controlled by changing the growth time, solution concentration, temperature, and pH.[82] The fiber diameter might be controlled by varying the grain size of the nucleation layer through the anneal conditions.[83] The fiber spacing can also be controlled through changes to the microstructure of the underlying nucleation layer and through the growth of vertical or tilted fibers.[81] Equally

important in the optimization of such a device is that the ZnO nanofibers, based on a decomposed zinc acetate nucleation layer, make an ohmic contact to indium tin oxide (ITO), the electrode on which the fibers are grown.[81] This is discussed in more detail in the following chapter.

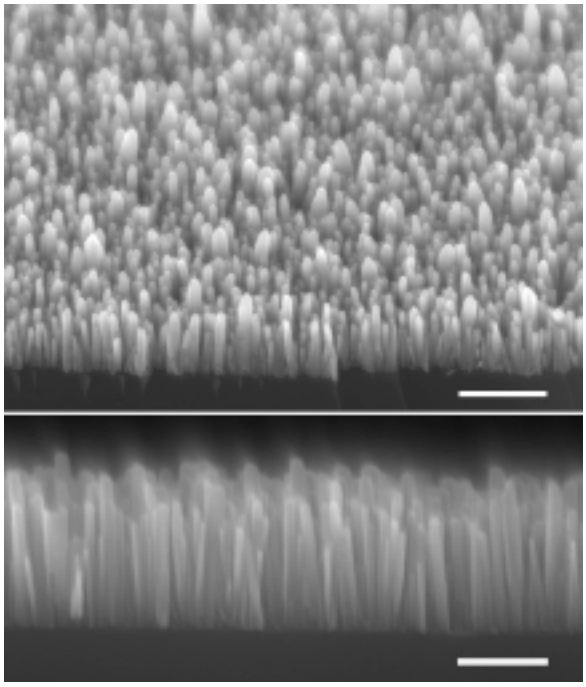

Figure 1.16 SEM images of ZnO fibers grown from an aqueous solution of zinc nitrate on a decomposed zinc acetate nucleation layer.[81] The scale bars are 200 nm.

1.7 Changing the Band Offset in Hybrid Polymer/Metal Oxide Photovoltaic Devices

The band offset in the donor-acceptor pair is important for controlling both the electron transfer kinetics as well as determining the maximum open circuit voltage. The

offset between the donor LUMO and the acceptor LUMO, or conduction band as seen in Figure 1.5, must be great enough to allow for fast electron transfer while keeping the recombination rate low. However, it is important that the offset is not too great as there is a significant loss of photovoltage with a band offset that is too large. In order to increase the performance of hybrid polymer/metal oxide devices, substitutional dopants such as Mg can be incorporated into the solution-based ZnO precursor solutions to form ZnMgO. By incorporating Mg into ZnO ,the electron affinity can be decreased. As a result, there can be an increase the photovoltage, or open circuit voltage (V_{OC}) as illustrated in Figure 1.17. Devices made using the Mg doped nanofibers may have increased efficiency because of a reduction of the energy lost through electron transfer from the donor polymer to the metal oxide acceptor material. The effect of Mg doping on the electron affinity and maximum expected V_{OC} are presented in Figure 1.17. It has been shown that the band gap of ZnO (3.2 eV) increases linearly with the incorporation of Mg.[84] This could be of additional benefit as photoexcitation in the ZnO from ultraviolet radiation can result in hole transfer from the ZnO to the polymer. This often leads to degradation of the polymer due to the strong oxidizing potential of the ZnO. Increasing the band gap might reduce the amount of photoexcitation in the metal oxide, and thereby eliminate one of the degradation mechanisms in this cell design. A more detailed description is presented in Chapter 4.

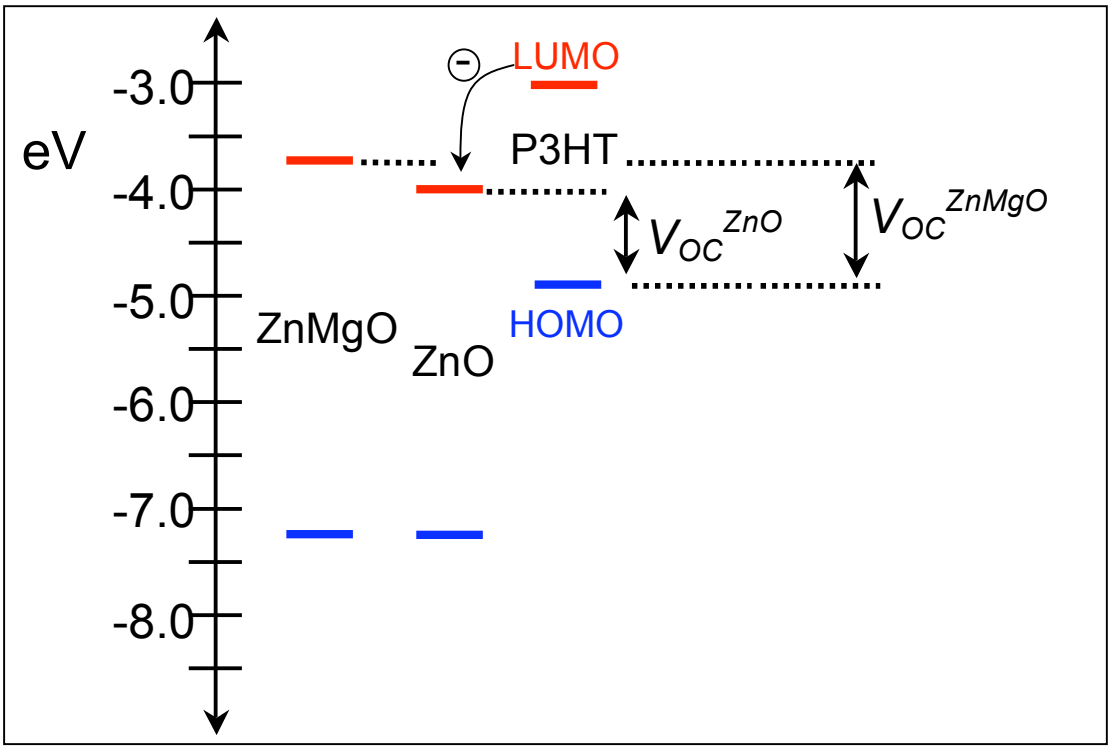

Figure 1.17 Band diagram of P3HT and e^- acceptors, ZnO and ZnMgO, showing electron transfer and maximum V_{OC} for both ZnO and $Zn_{0.9}Mg_{0.1}O$ acceptors.

1.8 Thesis Outline

As discussed above, composites of conjugated polymers and inorganic semiconductor materials are an attractive route toward simple, low-cost photovoltaic devices. The main objective of this thesis is to explore the use of hybrid materials in ordered bulk heterojunction polymer solar cells. This thesis specifically focuses on hybrid devices using ZnO nanofibers as an ordered inorganic acceptor. Bulk heterojunction solar cells are fabricated from conjugated polymers and ZnO nanofibers.

The second chapter explores the growth and morphological control of the ZnO

nanofiber film. The synthesis of ZnO structures consists of the precipitation of the inorganic out of a basic aqueous solution of zinc salts. The structural and optical properties of the ZnO nanofibers are characterized using different techniques. These nanofibers appear very suitable for forming a composite with conjugated polymers.

Chapter 3 introduces ZnO as an electron-accepting species in hybrid photovoltaic devices. The characterization of these devices is explained in detail. The photovoltaic effect found in composites of conjugated polymers and ZnO nanofibers is studied as a function of the ZnO nanofiber morphology and the processing conditions of the composite device. Light-intensity dependence measurements and external quantum efficiencies give insight into the factors that limit the performance of this solar cell. The PV properties and morphology of these composites are examined in detail.

Chapter 4 covers the incorporation of $Zn_{1-x}Mg_xO$ electron acceptor materials into hybrid polymer/metal oxide solar cells. The substitution of Mg into the ZnO lattice decreases the electron affinity of the acceptor material, and therefore reduces the band offset in the device. The reduced band offset leads to a larger open circuit voltage in the device and leads to increased photovoltaic performance. The optical, structural, and electrical properties of the $Zn_{1-x}Mg_xO$ material are characterized using a number of techniques in the context of photovoltaic device performance.

The final chapter presents overall conclusions of the work and future directions for further improvements in these devices.

CHAPTER 2

ZINC OXIDE NANOFIBER SYNTHESIS AND APPLICATION IN HYBRID POLYMER/INORGANIC SOLAR CELLS

Abstract

This chapter introduces ZnO nanostructures for applications in hybrid solar cells. ZnO nanofibers have been grown from several different nucleation layers in a low-temperature solution process. The structural and optical properties of the ZnO nanofibers are characterized using several techniques. The high surface area of nanostructured ZnO films, combined with their electron accepting and exceptional transport properties, make ZnO nanofibers excellent candidates for ordered bulk heterojunction composite devices.

2.1 Introduction

To create ordered hybrid polymer/metal oxide solar cells, the nanostructured metal oxide acceptor must be synthesized at the proper length scale prior to the incorporation of the conjugated polymer. The application of nanostructured metal oxides in solar cells has received much attention since the introduction of the dye sensitized cell developed by O'Regan and Grätzel based upon nanocrystalline TiO_2 electrodes.[85] These films are based upon hydrothermally grown metal oxide nanoparticles that are coated onto the substrate from a paste. They are subsequently sintered at temperatures greater than 400 ºC for extended periods of time to form semicrystalline thin films. A light absorbing dye is then absorbed on the surface of the nanocrystalline TiO_2 film. As the

surface area or roughness of the nanocrystalline TiO_2 film increases, more dye can be absorbed, resulting in an increase in the optical density. Photoexcitation of the dye results in electron transfer to the metal oxide acceptor and subsequent hole transfer to the liquid electrolyte. The electron then travels through the TiO_2 material to the front contact, and the hole travels through the liquid electrolyte to the counter electrode.

A number of groups have developed dye sensitized solar cells based on ZnO nanoparticle films, and despite lower performance than TiO_2 equivalents, they have demonstrated reasonable efficiencies for polycrystalline nanostructured films.[86, 87] The charge transport properties of these nanoparticle films are regarded as being a limiting factor in these devices. The utilization of nanorod geometries have lead to enhanced charge transport in cells based on hematite nanorods. This is attributed to the reduction of grain boundary interfaces.[88]

Recently, dye sensitized solar cells have been realized using oriented single crystal ZnO nanowires grown from a low-temperature aqueous solution. Despite improved transport properties, however, the nanowire devices do not reach the same levels of performance as the nanoparticle devices, presumably due to lower surface areas resulting in the decreased optical density of the absorbed dye.[80] They do demonstrate larger short-circuit current densities than devices based on ZnO nanoparticle films with similar surface areas. This indicates that the improved charge transport in the nanowire films leads to more efficient charge extraction out of the device. The ZnO nanofiber devices demonstrate open circuit voltages greater than 600 mV, which are similar to devices based on nanoparticle TiO_2.[80, 85] These are much larger than the photovoltages measured in ZnO nanoparticle devices,[86, 87] indicating that the ZnO nanofibers may offer superior material properties.

Dye sensitized solar cells are dependent on extremely large roughness factors for efficient light absorption of the surface-absorbed dye molecules. Other types of excitonic solar cells, however, might benefit from the charge transport and ordered nature of nanowire-based devices. Due to the filling of the nanostructured metal oxide pores with

a conjugated polymer absorber, solid state hybrid polymer/inorganic photovoltaic devices do not require the same levels of surface roughness for efficient device performance. Efficient devices with estimated power conversion efficiencies of 1.0% have been fabricated using low surface roughness nanostructured films of CdTe nanorods infiltrated with poly(3-octylthiophene) (P3OT).[89] These efficiencies are comparable to those present in the nanowire-based dye sensitized solar cells discussed above despite the fiber length being over two orders of magnitude shorter. This is also reasonably close to the efficiencies found in hybrid polymer/inorganic nanoparticle blends presented in the last chapter, indicating the viability of the hybrid polymer/nanostructured inorganic device. Recent work on modeling of an ordered bulk heterojunction device architecture indicates that small diameter nanofibers are necessary for high quantum efficiency values.[69] Therefore, the development of hybrid polymer/ZnO nanofiber devices is a promising route to increased performance and stability in polymer-based solar cells.

2.2 Synthesis of ZnO Nanostructures

The synthesis of ZnO nanofibers has been studied extensively. Various deposition techniques have been developed for the growth of oriented ZnO nanofibers with diameters ranging from 20 nm to greater than 200 nm and lengths from less than 100 nm to more than 25 μm. Oriented arrays of ZnO fibers can be synthesized from vapor-liquid-solid epitaxial (VSLE) growth,[90, 91] metal-organic chemical vapor deposition (MOCVD),[92] through templates with anodic alumina,[93] and epitaxial electrodeposition.[94]

A more economical wet chemical approach is necessary for the development of large area solar cell devices. Work on the electrodeposition of mesoporous ZnO has demonstrated that cathodic electrochemical deposition reduces the dissolved oxygen or nitrate ions in acidic solutions containing Zn^{2+} ions to increase the pH near the electrode

surface. The result is Zn ions near the electrode precipitating out of solution forming mesoporous ZnO films.[95] It is important to note that hydrothermal ZnO nanofiber growth often results in much smaller diameter fibers, compared to gas-phase growth processes.[81] This preferred morphology is yet another potential advantage of using a solution-based ZnO fiber growth method in addition to the lower processing costs compared to gas phase growth.

The hydrothermal growth of the oriented ZnO nanorods through a wet chemical process involves the thermal decomposition of a 1:1 ratio of methenamine and zinc nitrate in an aqueous solution.[96] This approach can deposit ZnO nanostructures on a variety of substrates.[72, 97-99] The diameter of the ZnO nanorods can be decreased through a reduction of the concentration of either component. Disordered ZnO nanowires with diameters near 20 nm have been grown from 1 mM solutions of zinc nitrate and methenamine.[72] Similar results have been observed with the use of other complexing agents that help to stabilize the zinc cation (Zn^{2+}) in solution such as hexamethylenetetramine (HMT), sodium citrate, dimethylaminoborane (DMAB), urea, ethylenediamine, and ammonium fluoride.[97-101] These hydrothermal growth methods use complexing agents to increase the pH upon their decomposition to the necessary values for precipitation of ZnO.[97, 101]

The crystal structure of ZnO is a hexagonal close packed (HCP) wurtzite structure with the point group 3m, space group $P6_3mc$, and zinc atoms on the tetrahedral sites. There is a nonpolar plane (1000) with C_{6v} symmetry, a polar basal plane and a polar top face (0001) consisting of tetragonal zinc atoms with terminal hydroxyl groups as seen in Figure 2.1.[82, 98] The nonpolar (1000) face is more stable than the polar faces. Since there is no center of inversion in the wurtzite crystal structure, there is an asymmetry along the c-axis, allowing for the anisotropic growth of ZnO crystallites.[96, 98] Water is unable to deprotonate hydrated divalent metal cations at ambient pressure. Deprotonation requires the utilization of hydrothermal conditions and neutralization under basic conditions, or chemical complexation in order to generate ZnO from zinc salts.[72] The

growth unit of the crystal is the complex formed by the connection of the Zn^{2+} with the hydroxyl ligands on the polar (0001) top face. As a result, the growth velocities under hydrothermal conditions are greatest in the polar top (0001) surface of the ZnO crystal.[98, 102]

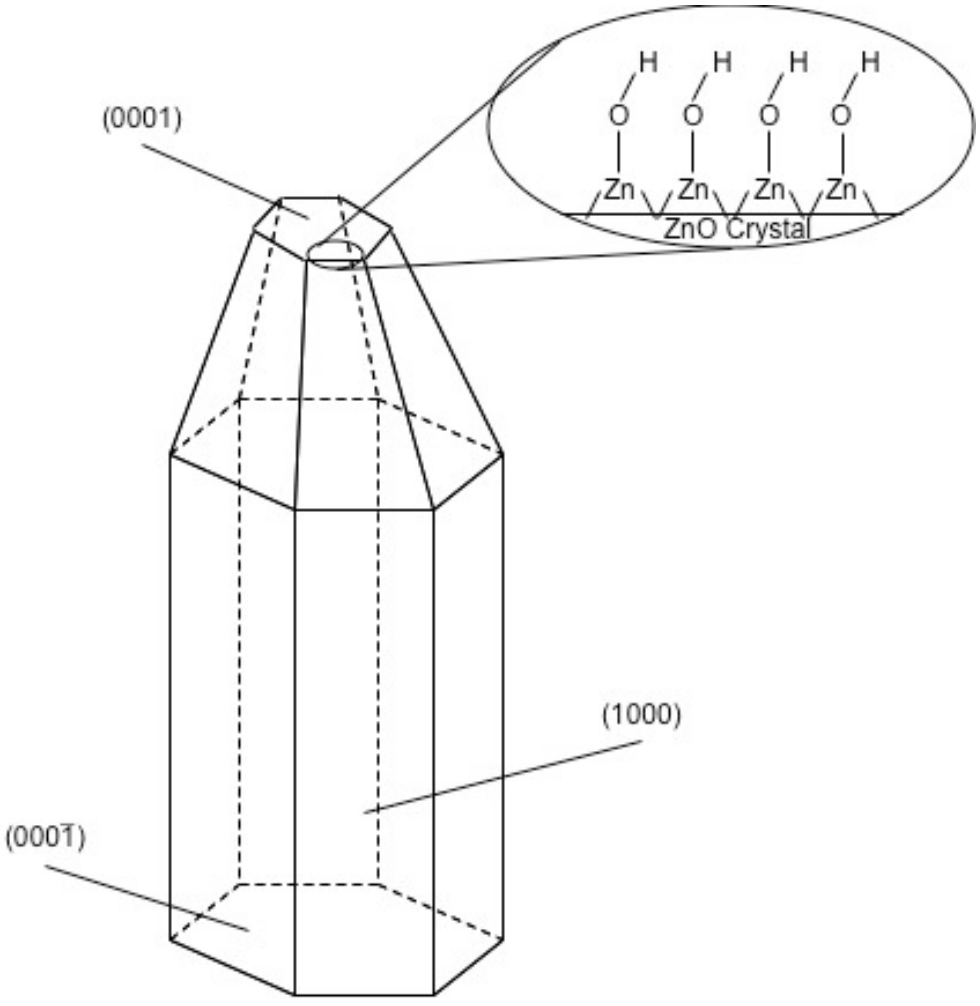

Figure 2.1 Growth habit of ZnO columns. Expanded view of the surface of the (0001) plane.[82]

The hydrothermal method for ZnO nanofiber growth used in this work was developed by colleagues at NREL. This method does not rely on a complexing agents and is capable of growing ZnO nanofibers at higher rates with excellent uniformity over large areas.[82] Due to the basic conditions required for growth, elaborate substrate cleaning is not required for uniform growth of ZnO nanofibers. Ordered (0001) oriented ZnO nanofibers were grown by epitaxial chemical deposition from a supersaturated solution at pH 12 of 1 mM zinc nitrate and sodium hydroxide (NaOH) on substrates coated with sputtered ZnO nucleation layers. It was observed that the pH of the aqueous solution determines the crystal phase of the material deposited on the substrate. ZnO precipitation occurs above pH 9, whereas below this pH, zinc hydroxide is precipitated.[82, 101] Therefore, careful control of the pH through the concentration of NaOH and the solution temperature is necessary for ZnO nanofiber growth.

The two processes required for crystallization in a supersaturated solution are nucleation and growth. Nucleation is a critical step with this particular deposition method, since ZnO nanofibers growth was observed only on substrates coated with ZnO.[82] Nucleation can occur through two methods. Homogeneous nucleation can occur in a supersaturated solution, resulting in precipitation of ZnO particles.[82, 96] Homogeneous nucleation will occur if is the pH is lowered to a value below pH 12, above which ZnO will not precipitate out of the solution.[82] Heterogeneous nucleation on the substrate coated with sputtered ZnO has a lower free energy activation barrier than homogeneous nucleation, and therefore fiber growth occurs there.[82, 96] The interfacial tension between the species in solution and the nucleation site is lower with growth on the same crystal type, which leads to fiber growth on the ZnO-coated substrates and no fiber growth on other substrate materials with this method. The hydroxyl groups on the polar ZnO surfaces may help to enhance the growth mechanism by lowering the activation energy for ZnO precipitation at the interface of the ZnO nucleation site and the Zn^{2+} in solution.[82] Therefore the ZnO-coated substrates act as nucleation sites for epitaxial growth of the ZnO fibers. Similar results have been observed previously where

ZnO fibers were grown off of substrate coated with an amorphous and crystalline ZnO nucleation layers compared to uncoated substrates.[101]

2.3 Growth of ZnO Nanofibers on Sputtered ZnO Nucleation Layers

The growth of ZnO fibers was reproduced on thin (~50 nm) sputtered ZnO nucleation layers on glass.[82] An aqueous solution of zinc nitrate with concentration of 0.001 M and NaOH with concentration of 0.08 M was made and heated to 70 °C in a shallow glass beaker. The total volume of the solution was 200 ml. The ZnO-coated glass substrates were cleaned by rinsing with deionized (DI) water, acetone, and ethanol prior to placing them into the solution, which was stirred. Four to five samples were submersed for 20 minutes while covered. It was observed that the ZnO nanofiber growth rates were inversely proportional to the number of substrates. After removing the samples from the solution, they were rinsed with DI water and blown dry with flowing N_2 gas. The ZnO nanofiber morphology was characterized on a JEOL 6320 FE-SEM. SEM images were taken of the fibers grown on the thin sputtered ZnO nucleation layer, as seen in Figure 2.2. The nanofibers are spaced very close together and have relatively small diameters of less than 50 nm with uniform fiber lengths of 500 nm for a growth time of 20 minutes. The fibers grow vertically and coalesce into groups at the tips of the fibers; therefore, they do not maintain the same fiber spacing as they grow.

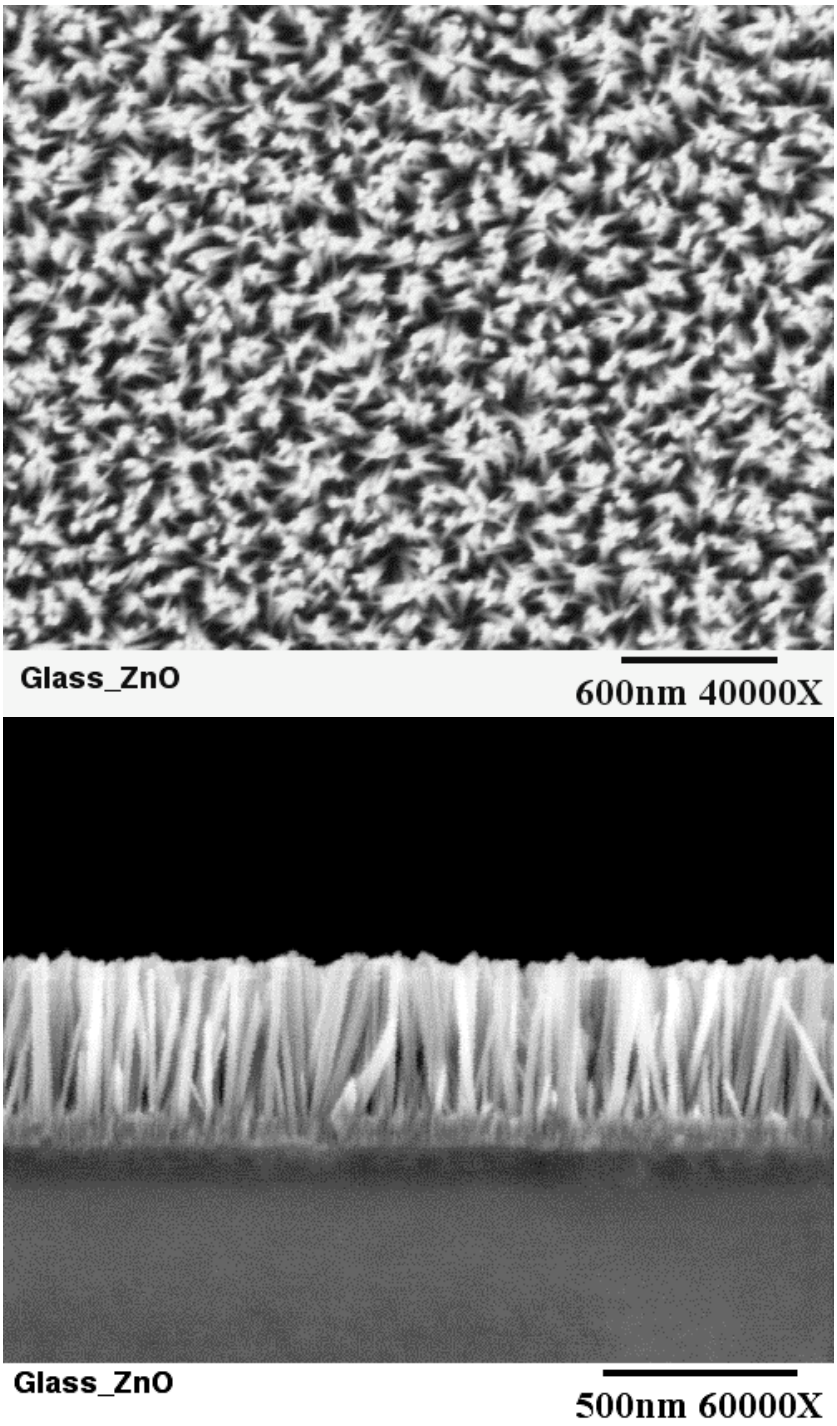

Figure 2.2 SEM images of ZnO nanofibers grown from a thin sputtered ZnO nucleation layer. **a.** Top view. **b.** Cross section.

ZnO fibers were also grown as described above for 20 minutes off of thick (> 500 nm) sputtered ZnO nucleation layers as seen in Figure 2.3. These fibers have larger diameters of greater than 100 nm, which is likely due to larger grain size in the sputtered ZnO nucleation layer. The length of the ZnO nanofibers is uniform across the sample and is similar to those grown on thin sputtered nucleation layers, indicating that the nucleation layer has little effect on fiber length. The fibers grow much closer together, compared to those grown on thin nucleation layers, leaving little room between the fibers. The fiber growth is still uniform and well ordered with little coalescence at the tips of the fibers with growth. With fibers that are closer together, there is stronger vertical orientation in the resultant thin film of ordered ZnO nanofibers.

As has been observed by others, the microstructure of the nucleation layer plays a very important role in determining the ZnO nanofiber morphology. The fiber diameter, orientation, and spacing are controlled primarily by the morphology of the nucleation layer, whereas the fiber length is controlled by growth solution conditions including growth time, temperature, concentration, and pH. For the development of ordered polymer/inorganic solar cells, smaller fiber diameters are desired, and therefore the thin sputtered nucleation layer is more applicable. While growth off of the sputtered ZnO nucleation layer proceeds uniformly with very good vertical alignment, the fiber spacing might prove to be too small for polymer/ZnO nanofiber devices due to the inability to intercalate the polymer completely. In addition, sputtered ZnO nucleation layers might not be ideal since it introduces another vacuum-based deposition into the fabrication process. The use of solution-processed materials more compatible with traditional plastic processing is more desirable for lower processing costs.

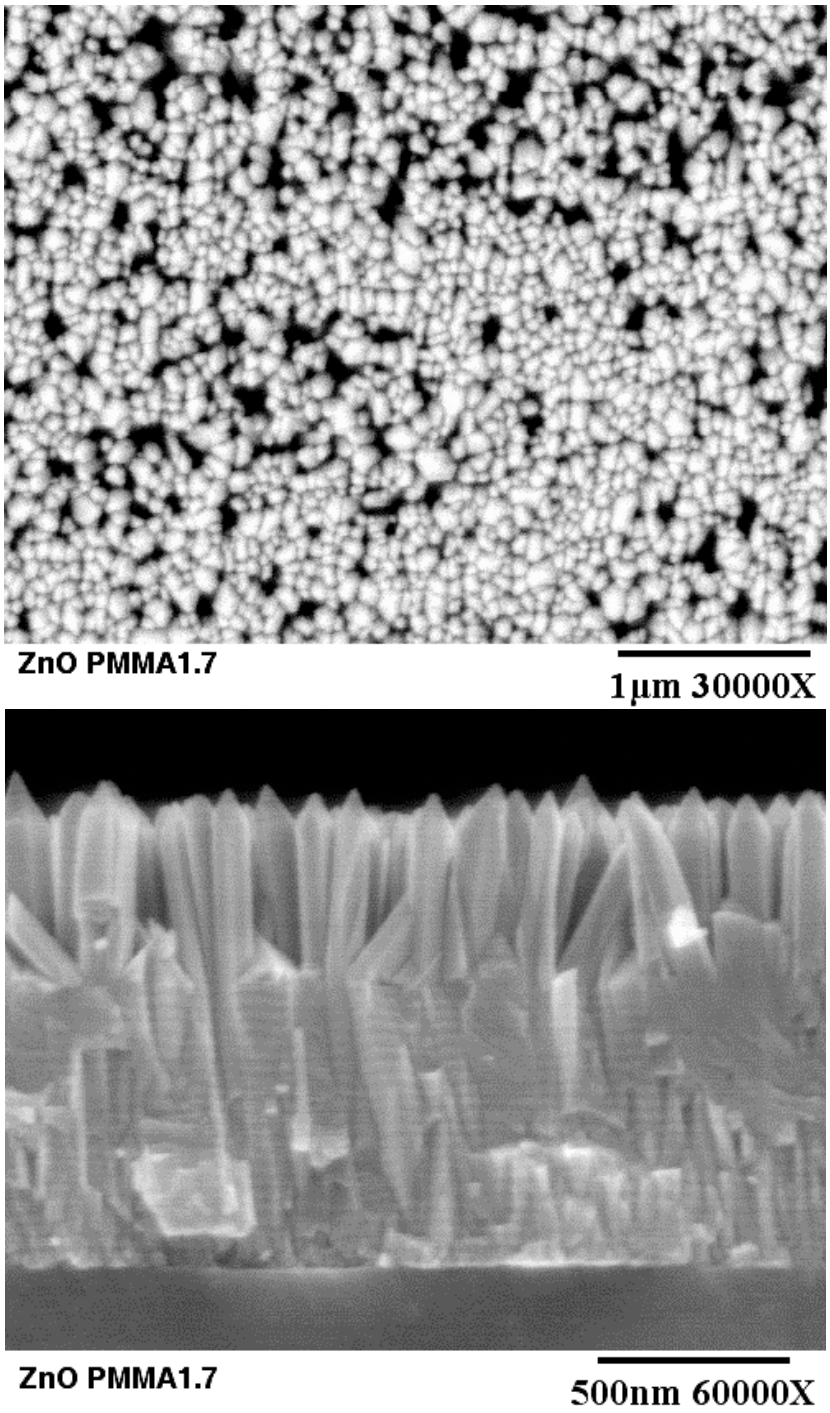

Figure 2.3 SEM image of ZnO nanofibers grown from a thick sputtered ZnO nucleation layer. **a.** Top view. **b.** Cross section.

2.4 Growth of ZnO Nanofibers on Solution-Based ZnO Nucleation Layers

Hydrothermal growth has been demonstrated with much success on nucleation layers derived from thermally decomposed zinc acetate (ZnAc) thin films.[81, 101] Thin films of ZnO have been prepared from solution-based precursors with preferred (0001) orientation, which is ideal for ZnO fiber growth.[83] A similar method has been used here without the high-temperature anneal to maintain small ZnO grains in the film. With the deposition of a solution-based ZnO nucleation layer, ZnO nanofibers can be grown on a variety of substrates such as glass, quartz, sapphire, fluorine-doped tin oxide (FTO), and ITO, all of which are flat and stable at the processing temperatures employed here.

The substrates used in this study were first cleaned by ultrasonic agitation in acetone, chloroform, and isopropanol for 10 minutes each followed by an oxygen plasma treatment of 150 watts at 500 mTorr for 5 minutes. The plasma treatment was done to increase the wetting properties of the precursor solution on the substrate. Without this treatment, the thin films are not uniform. A nucleation layer of ZnO was spin-coated at 2000 RPM onto the substrate using a zinc acetate and ethanol amine solution in 2-methoxyethanol. The ratio of ethanol amine to ZnAc was 1.0 and the concentration of zinc acetate was 0.75 M.[83] After spin coating the ZnAc film, the substrate was annealed on a hotplate at 300 ˚C for 30 minutes in air and rinsed with deionized water and ethanol after annealing. Next, ZnO nanofibers were hydrothermally grown for 10 minutes at 70 ˚C from the nucleation layer in a 1 mM solution of zinc nitrate as described above.[82] The samples were rinsed in DI water and ethanol, then were dried under flowing N_2 gas. SEM images show that ZnO nanofibers grow on the ZnAc derived ZnO nucleation layer, as seen in Figure 2.4. The fiber diameters were near 30 nm, with spacing less than 100 nm. The fiber length is reduced to 250 nm with a growth time of 10 minutes for four substrates. This is a shorter length and growth time then used to obtain the nanofibers in Figures 2.3. Despite the shorter growth time, there is still a coalescence of the fibers at the fiber tips resulting in larger fiber spacing.

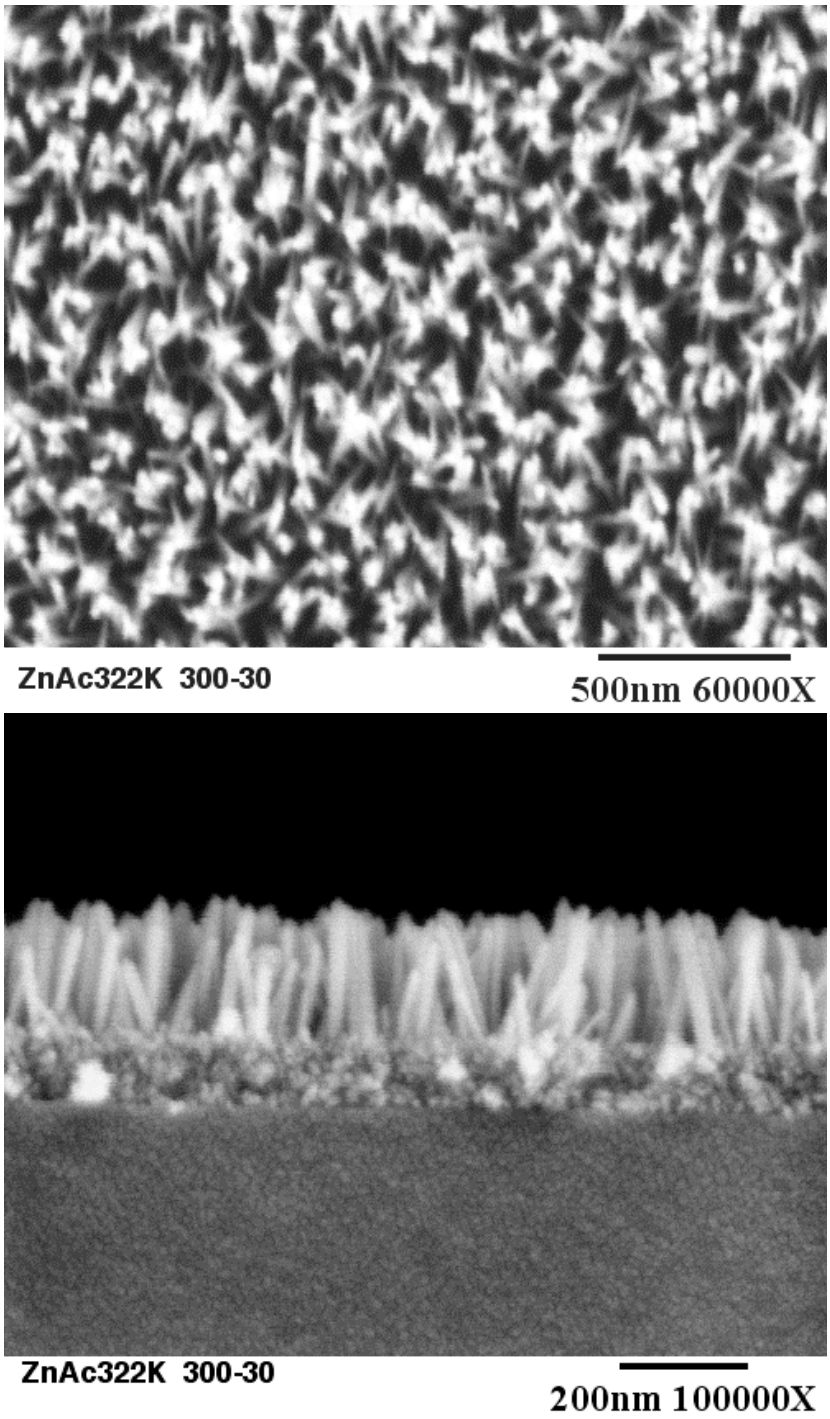

Figure 2.4 SEM images of ZnO nanofibers grown on a ZnAc thin film spin coated on glass and annealed at 300 °C for 30 min. **a.** Top view. **b.** Cross section.

The processing flexibility of the ZnAc-derived nucleation layers leads to easily modified ZnO nanofiber morphologies. The time and temperature of the thermal decomposition of the ZnAc nucleation layer are very important parameters that dramatically affect the fiber morphology. The factors affecting fiber length are the growth time, temperature, concentration, and pH. As noted above, the fiber diameter is determined largely by the microstructure of the polycrystalline nucleation layer from which the fibers are grown. The morphology of these nanostructured oxide films was characterized by scanning electron microscopy (SEM) in both plan view and in cross section on a variety of substrates. The ZnO nanofibers were only observed to grow on the annealed ZnAc-derived ZnO nucleation layer.

The ZnO nucleation layer is spin coated from a ZnAc solution and is subsequently annealed in air to form a ZnO film. Without annealing the ZnAc film, no fiber growth is observed. Fiber growth has been observed previously after extensive drying of the ZnAc film in a vacuum oven at 60 °C for 24 hours prior to fiber growth.[101] This process may eliminate the high boiling point solvent from the film, thus allowing fiber growth to occur. In this work, no fiber growth was observed with annealing of the ZnAc layer at 100 °C for 30 minutes. This may indicate that either evaporation of the solvent or thermal decomposition of the ZnAc is necessary for proper formation of ZnO fiber nucleation sites. The boiling points of 2-methoxyethanol and ethanolamine are 125 °C and 170 °C, respectively. The elimination of the solvent may not take place without extensive drying until the temperature is above the boiling point of both solvents. Additionally, the decomposition temperature for ZnAc is near 240 °C.[103] The crystallization of ZnO from the ZnAc film begins at 200 °C – 300 °C.[83] This agrees with recent results using low boiling point solvents where little fiber growth was observed below 200 °C.[81] These observations indicate that the ZnO fibers can nucleate and grow on the ZnAc material annealed at temperatures less than the decomposition temperature of ZnAc. The evaporation of the solvents, the decomposition of ZnAc, and

the crystallization of ZnO may occur simultaneously with the high heating rates used in this study. Therefore without drying the ZnAc films in a vacuum oven, annealing temperatures greater than 200 °C need to be employed for successful nanofiber growth using the selected growth method.

The diameter of the ZnO fibers is closely related to the temperature at which the ZnAc film is annealed, as seen in Figure 2.5a-d. All of the films were grown from a 1 mM solution of zinc nitrate at 70 ˚C for 20 minutes and, as a result, the fiber lengths are relatively uniform at 500 nm. Annealing the ZnAc layer at 500 ˚C in air for 60 minutes in a preheated oven leads to a relatively thick polycrystalline nucleation layer of about 200 nm that has large nucleation sites from which the ZnO fibers grow. This results in a rather large fiber diameter of 70 nm, and the fibers grow vertically with little coalescence of the fibers at their tips as seen in Figure 2.5a.

The thermal decomposition of a ZnAc layer annealed at 300 ˚C for 30 minutes on a hotplate results in a polycrystalline nucleation layer thickness of about 100 nm with much smaller grain size than for films annealed at 500 ˚C. ZnO fibers grown on nucleation layers annealed at 300 ˚C have diameters near 30 nm and are tilted with significant coalescence as seen in Figure 2.5b.

When the ZnAc layer is annealed at its decomposition temperature of 240 ˚C for 10 minutes, the resulting polycrystalline film has very small diameter grains. The fibers grown on the 240 °C annealed ZnAc film have diameters approaching 20 nm, and are still relatively ordered with a similar amount of coalescence to those of films annealed at 300 °C as seen in Figure 2.5c.

Disordered fiber growth was observed from ZnAc films annealed at 200 °C as seen in Figure 2.5d. Here, the ZnO nucleation layer is extremely thin and may not be continuous leading to a lower density of disordered ZnO fibers with very small nucleation sites. This would indicate that it may be necessary to process the ZnAc nucleation layer at temperatures at or greater than the decomposition temperature of

ZnAc in order to form properly oriented crystalline ZnO nucleation sites. When the nucleation layer is annealed at 200 °C, the fiber diameter remains small. However the diameter is not noticeably smaller than fibers grown from nucleation layers annealed at 300 °C.

In addition to the temperature, the fiber orientation can be controlled by the duration of time for the anneal process of the ZnAc nucleation layer. ZnO fiber growth from a nucleation layer annealed at 300 ˚C for 30 minutes, as seen in Figure 2.5b, show well aligned, near vertically oriented nanofibers. However, fibers grown on a nucleation layer annealed at 300 ˚C for 5 minutes results in more disordered fiber orientation, as seen in Figure 2.5e. This could be the result, again, of a very thin nucleation layer that has non-uniform or incomplete coverage, or this could simply be a function of the orientation of the nucleation site on the surface.

As has been observed recently, non-continuous ZnAc-derived seed layers result in vertically aligned nanofibers despite being grown from very thin nucleation layers.[81] In that study, the ZnAc layer was decomposed at a temperature of 350 °C for a period of 20 minutes, and atomic force microscopy (AFM) measurements confirmed that the nucleation sites were isolated on the surface. This is a good indication that the time is an important parameter in developing textured nucleation sites with proper orientation to support vertical growth of ZnO nanofibers. Additionally, ZnO nanofibers grown on ZnAc layers annealed at 250°C for 10 and 30 minutes have very similar morphologies, despite different anneal times. This indicates that an anneal time greater than 10 minutes may induce vertical nanowires growth. On the other hand, for anneal times less than 10 minutes and anneal temperatures less than the decomposition temperature of ZnAc, disordered ZnO fiber growth results.

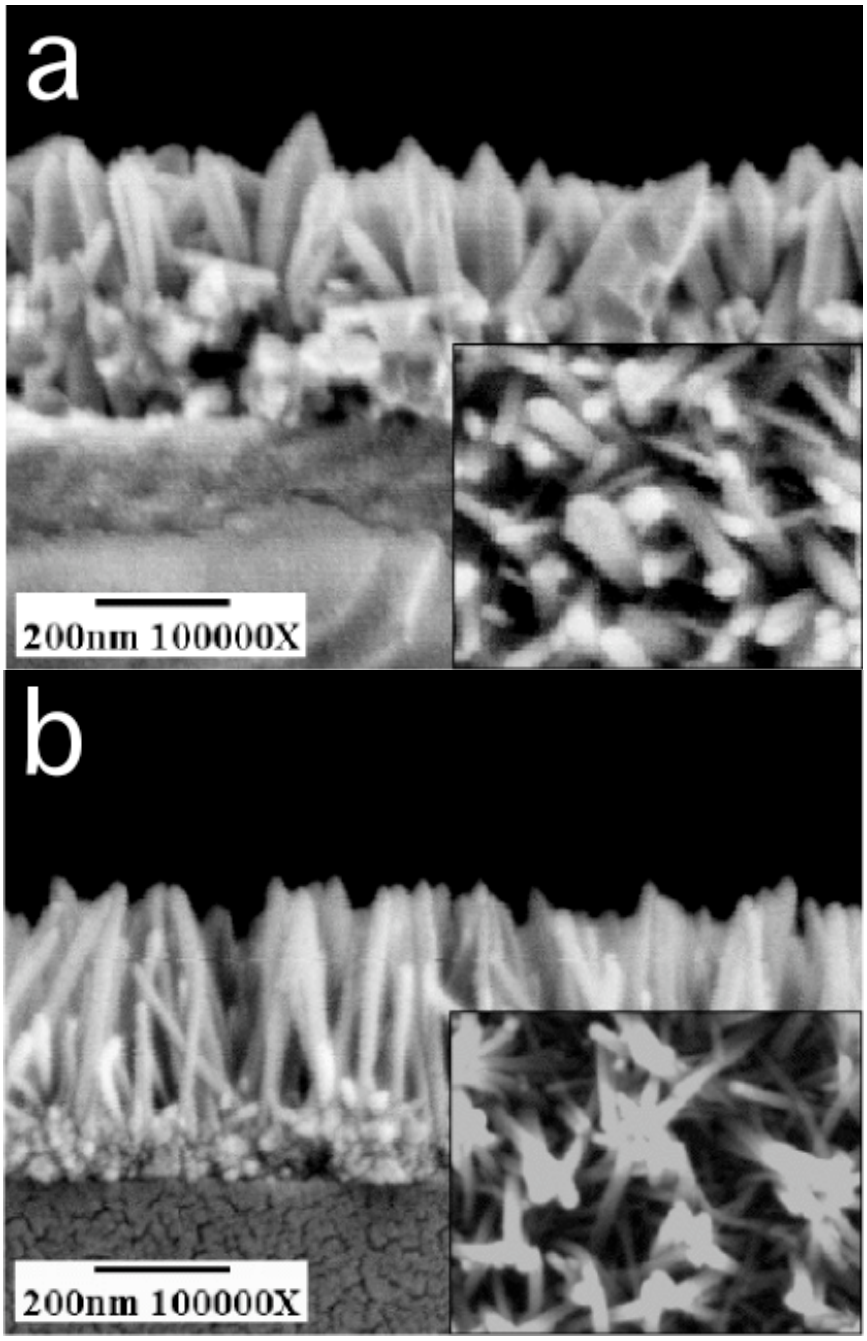
a
200nm 100000X
b
200nm 100000X

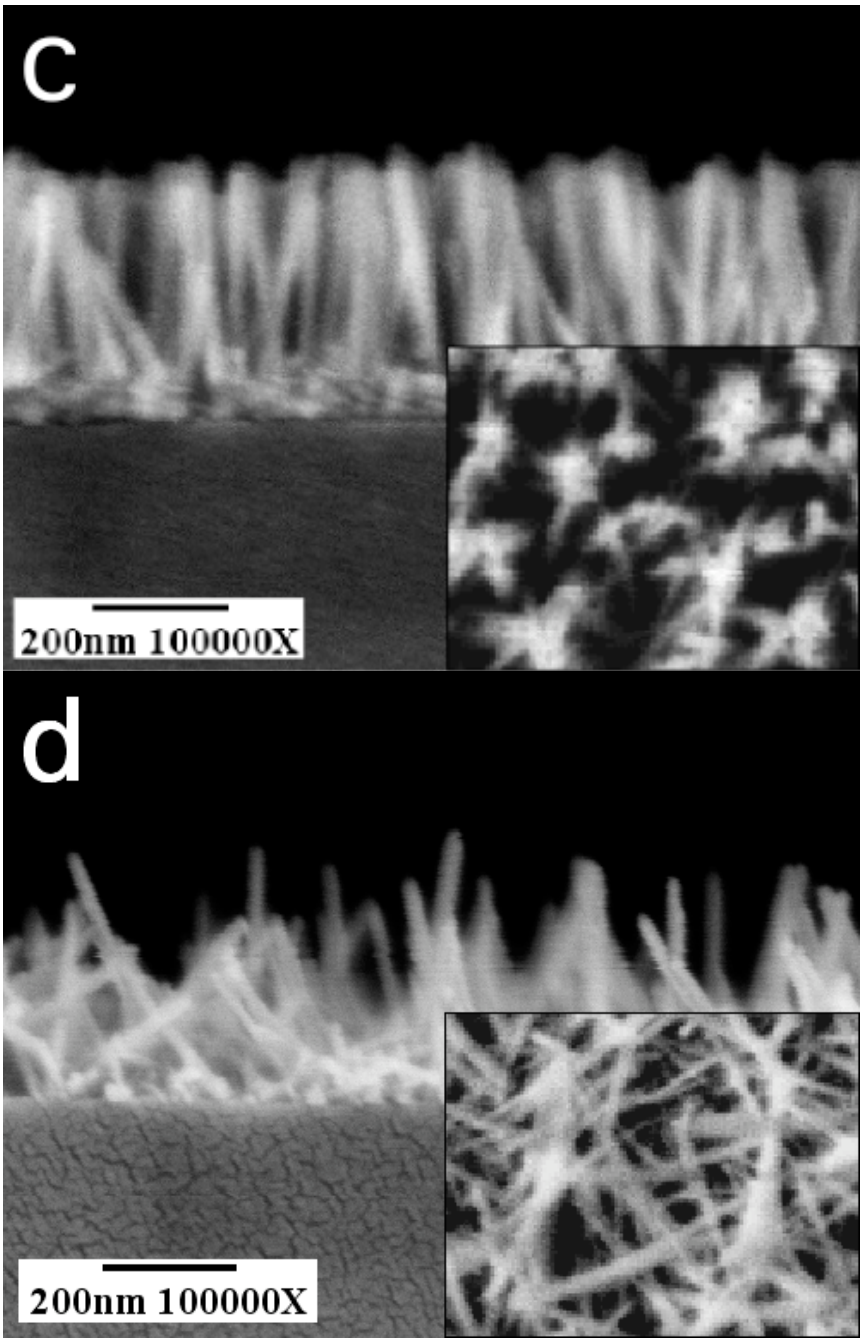
c
200nm 100000X
d
200nm 100000X

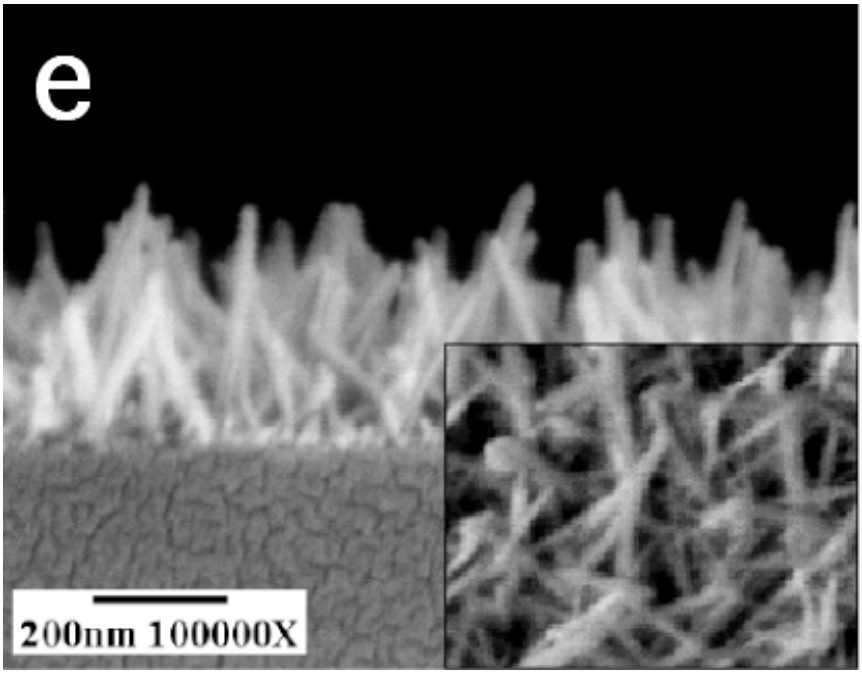

Figure 2.5 SEM images of ZnO fibers grown on annealed zinc acetate nucleation layers spin-coated onto glass substrates. Fibers were grown in a 1 mM zinc nitrate solution at pH 12 for a time of 20 minutes. The ZnAc nucleation layers are annealed at a) 500 ˚C for 60 minutes, b) 300 ˚C for 30 minutes, c) 240 ˚C for 10 minutes, d) 200 ˚C for 30 minutes, and e) 300 ˚C for 5 minutes.

2.5 Characterization of ZnO Nanofibers

The characterization of the ZnO nanofibers grown from a ZnAc nucleation layer is important for the development of ordered hybrid polymer/inorganic photovoltaic devices. Therefore the optical, structural, and defect properties of the ZnO nanofibers were studied to better understand the ZnO nanofiber material.

Fourier transform infrared (FT-IR) spectra of the ZnO films derived from the decomposition of ZnAc show no evidence of Zn-organic bands. It is concluded that the organic component was fully dissociated during the 300 ˚C anneal. The FT-IR spectra also confirmed the presence of ZnO in the nucleation layer and nanofiber film. The FT-

IR spectra also confirm the presence of hydroxyl groups absorbed on the surface of the ZnO. Bands associated with hydroxyl groups absorbed on the surface of ZnO were observed, which is expected based on the polar nature of the (0001) face in the ZnO crystal structure.[102]

The structural properties of the ZnO materials were characterized by X-ray diffraction (XRD) on a Bruker with a two-dimensional large area detector. The XRD data indicate that the ZnAc nucleation layer deposited on glass and annealed at 300 ˚C for 30 minutes is polycrystalline ZnO with a preferred orientation in the (0001) direction, also known more commonly as the (002) direction as seen in Figure 2.6. There are other crystal orientations present, but the dominant orientation is (002). This is the preferred orientation for vertical ZnO fiber growth. The nanofibers are crystalline ZnO with the wurzite crystal structure, and the fibers grow preferentially in the (002) direction, as seen in Figure 2.6. The nucleation layer in the film used to obtain Figure 2.6 was annealed for 30 minutes at 300 ˚C. The fiber length is estimated to be 500 nm based on the simultaneous growth of a sample used for SEM imaging.

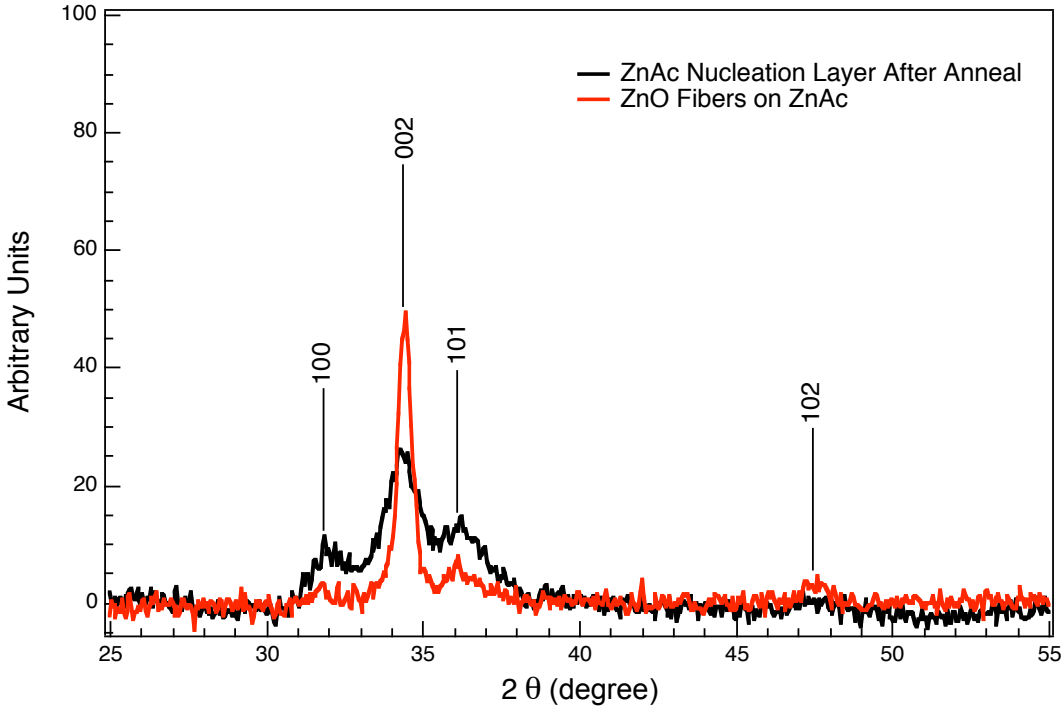

Figure 2.6 XRD data for ZnAc nucleation layer (black), and ZnO nanofiber film grown on ZnAc nucleation layer, intensity vs. angle. ZnO fibers were grown at pH 12, 70 °C for 20 minutes from a zinc acetate nucleation layer annealed at 300 °C for 30 minutes.

The optical absorption spectra of the ZnO materials were measured on a Hewlett Packard 8453 UV-vis spectrophotometer. For this study, the ZnAc-derived nucleation layers were deposited on quartz and annealed at 300 ˚C for 30 minutes. ZnO nanofibers were then grown on a nucleation layer for 20 minutes from the standard 1 mM zinc nitrate solution at 70 ˚C Both the nucleation layer and nanofibers indicate a band gap of about 3.2 eV as seen in Figure 2.7. The absorption of the ZnO nanofibers is higher than the ZnAc-derived nucleation layer, which is to be expected given the increased thickness of the ZnO film. However, there is little absorption beyond 400 nm where the conjugated polymer absorption begins. Visible absorption by the ZnO would help enhance the spectral response of these hybrid devices.

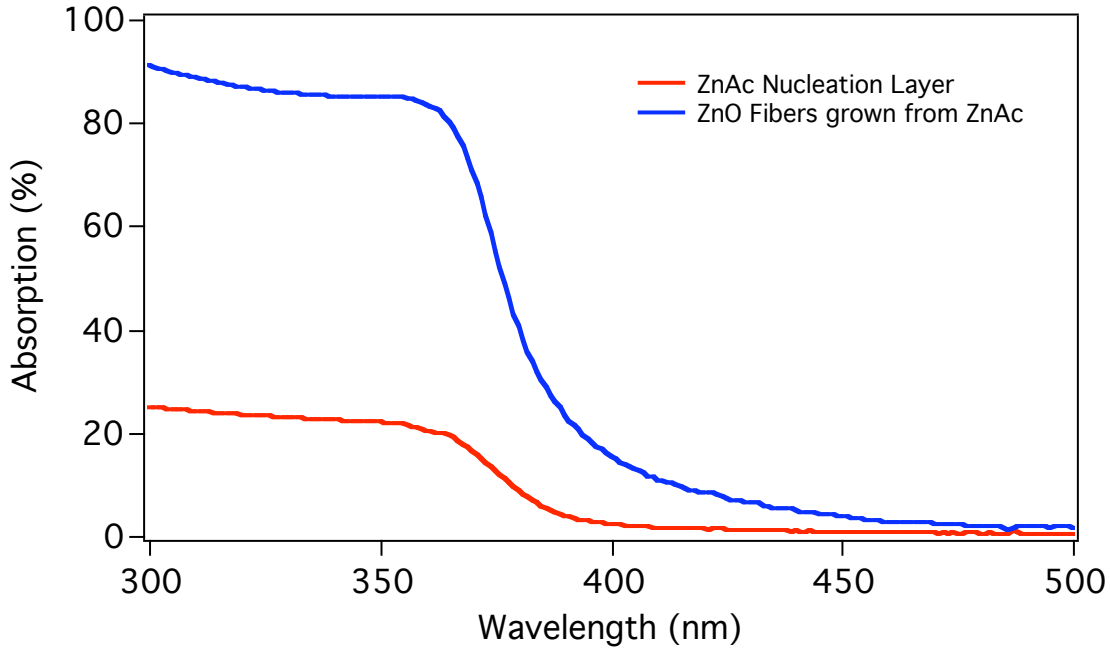

Figure 2.7 Absorption of ZnAc nucleation layer (red) and ZnO fibers grown from ZnAc nucleation layer vs. wavelength.

The defect structure of the ZnO films was investigated by photoluminescence (PL) using an excitation wavelength of 275 nm on a SPEX Flourolog with a Xenon arc lamp as the excitation source as show in Figure 2.8. The PL emission at about 430 nm seems to be an artifact of the substrate that is enhanced with the introduction of the ZnO films. The sharp emission peaks in the spectra are doubling of the excitation wavelength and other lines from the Xenon lamp that have made their way to the detector.

The PL emission spectra for the ZnO nucleation layer differs slightly from that of the ZnO fibers. The visible emission at about 650 nm from the ZnO nucleation layer is red shifted and is of lower relative intensity compared to the band edge emission. This sub band gap emission is probably defect related. The fact that the ZnO fibers have a much higher relative intensity of the visible emission at 620 nm, suggests a larger number

of defect states than the ZnO nucleation layer. The decreased relative intensity of the band edge emission is consistent with an increase in the number of surface defect states as observed previously by other groups looking at the size dependence of the ZnO fibers on the PL.[104] This may be important in device performance, as a higher number of surface defects in the ZnO could result in increased recombination. The defect-related emission located at 625 to650 nm is often associated with oxygen defects such as interstitials in the ZnO structure.[105] To reduce the relative intensity of the visible emission, the ZnO fibers can be annealed in a variety of reducing environments, leading to improved band edge emission.[106]

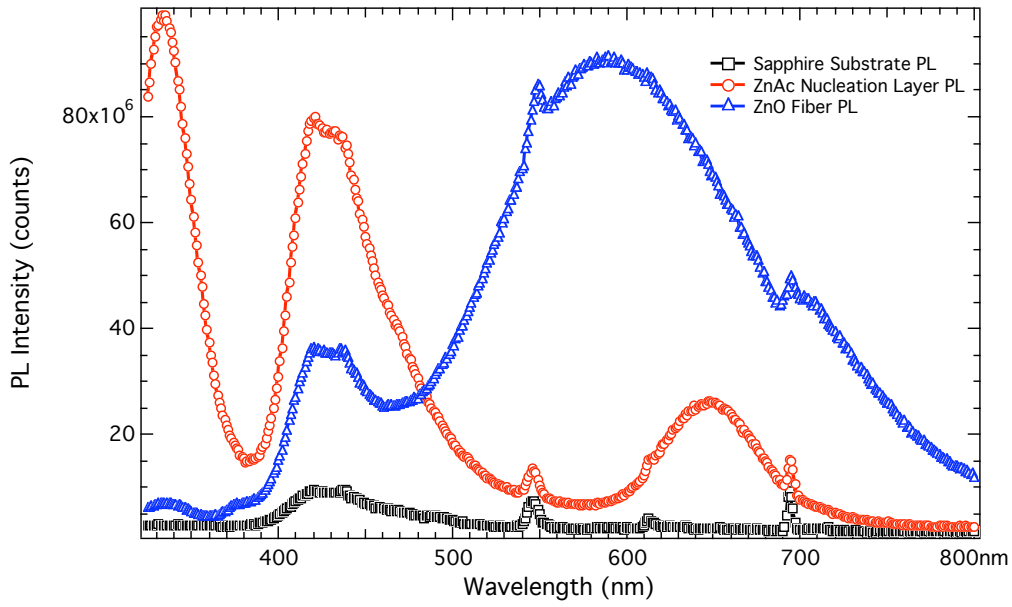

Figure 2.8 Photoluminescence spectra of ZnO fibers (open triangles), ZnO nucleation layer (open circles), and sapphire substrate (open squares). Zinc acetate layer annealed at 300 °C for 30 minutes, ZnO fibers grown at pH 12, 70 °C in a 1 mM zinc nitrate solution for 20 minutes.

2.6 Summary

The development of ZnO nanofiber films suitable for use in ordered hybrid polymer/ZnO photovoltaic devices has been presented. Hydrothermal growth of ZnO nanofibers from solution-based nucleation layers of ZnO nanostructures that are vertically aligned from the substrate has been demonstrated.

CHAPTER 3

ORDERED HYBRID POLY(3-HEXYLTHIOPHENE)/ZINC OXIDE NANOFIBER PHOTOVOLTAIC DEVICES

Abstract

This chapter presents results on the fabrication of a photovoltaic device consisting of poly(3-hexylthiophene) (P3HT) intercalated into a mesoporous structure of ZnO nanofibers. ZnO nanofibers were grown using the low temperature hydrothermal route described in Chapter 2. P3HT was spin coated on top of the structure, and intercalation into the voids between the nanofibers was induced with annealing. A silver electrode was used as the top contact. Fabrication, storage, and testing of the device were performed in air. These nanofiber devices exhibited a 4-fold increase in the short circuit current (2.17 mA/cm^2) compared to that for a planar ZnO-P3HT bilayer device (0.52 mA/cm^2) as a result of the increased donor-acceptor interfacial area. The efficiency of the nanofiber based device under 1-sun simulated solar illumination was 0.53% and was found to increase at higher incident light intensities, reaching a value of 0.61% at 2.5 suns. The inverted geometry of this device allows for the use of a silver top contact, making the device less susceptible to oxidation in the dark.

3.1 Introduction

Devices based on infiltrating conjugated polymers into mesoporous, nanostructured oxide semiconductor networks have demonstrated direct control of the

heterojunction interface[75, 76]. However, the reported efficiencies in these devices are presently limited by the disordered nature of the polymer in the very small pores in the polycrystalline metal oxide, and by the quality of the interfaces between the inorganic and organic materials.

To increase the efficiencies of these devices, a nanostructured oxide has been developed composed of ZnO nanofibers that are vertically aligned with respect to the substrate as described in the previous chapter. This has the advantages of both increasing the donor-acceptor interfacial area and creating high mobility electron transport pathways connected only to the negative electrode. The next step in device fabrication is intercalation of the conjugated polymer. This can be accomplished through the spin coating of the polymer onto the ZnO nanofiber film, followed by a low temperature annealing step to induce filling of the porous volume of the oxide. Finally, a top contact is deposited onto the conjugated polymer, and the devices are characterized as described in this chapter.

3.2 Fabrication of Hybrid Polymer/ZnO Photovoltaic Devices

Ordered hybrid polymer/ZnO devices were fabricated using the ZnO nanofiber films described in Chapter 2. The ZnO nanofibers must be grown on a transparent conductive oxide such as indium tin oxide (ITO) in order to contact the device. Devices were fabricated on patterned ITO coated glass substrates with a sheet resistance of 13 Ω/cm^2. The substrates were first cleaned by ultrasonic agitation in acetone, chloroform, and isopropanol for 10 minutes each. This cleaning eliminates any undissolved photoresist used in the patterning process, and dust and dirt from the surface that would reduce the device performance. This is followed by an oxygen plasma treatment for 5 minutes at a power of 150 watts and oxygen pressure of 500 mTorr. Next, a nucleation layer of ZnO is spin coated onto the ITO, which functions as the negative electrode. The

nucleation layer is deposited using the zinc acetate solution described in detail in Chapter 2. Following the spin coating, the ZnAc is removed from the contacts to the ITO electrode using a Q-tip wet with ethanol. The ZnAc must be removed prior to annealing to ensure that there is no barrier to electrical contact with the ITO during characterization. Next the ZnAc film is annealed for 5 to 30 minutes at 300 °C to form the ZnO nucleation layer. After annealing and cooling to room temperature the films are rinsed with DI water, acetone, and ethanol.

The ZnO nanofibers are then hydrothermally grown from the substrates coated with the ZnO nucleation layer using a 0.75 M zinc nitrate solution at 70 °C. The growth time is varied from 10 to 30 minutes leading to ZnO nanofiber lengths on the order of 200 to 500 nm. The fabrication of P3HT/ZnO fiber devices requires that a 200 nm layer of P3HT is deposited to cover the ZnO fibers to prevent shorting of the device. The polymer film can be deposited through spin coated from a 30 mg/ml chloroform solution. The fabrication of MDMO-PPV/ZnO devices requires an equivalent film thickness, which can be spin coated from a chlorobenzene solution. To intercalate the polymer properly into the ZnO nanofiber film, the samples are often thermally annealed at temperatures up to 200 ˚C for one minute under an argon atmosphere. Finally, a 90 nm silver top contact is deposited via thermal evaporation through a shadow mask to form the positive back electrode with active areas for each device of 0.1 cm^2.

For comparison of the nanostructured ZnO devices to planar devices, equivalent bilayer devices were fabricated in the same manner; however, ZnO fibers were not grown off of the nucleation layer. The ZnO nucleation layer itself was used as the acceptor with a planar heterojunction interface.

3.3 Intercalation of Polymer into ZnO Nanofiber Films

A number of challenges exist in the fabrication of ordered hybrid polymer/ZnO nanofiber photovoltaic devices. One of the main challenges is the intercalation of the polymer into the inorganic ZnO nanofiber films. As mentioned above, there are a number of nonpolar faces in the ZnO nanofibers and there is a polar top face. Initial studies of the intercalation of the polymer into ZnO fibers grown from a sputtered ZnO nucleation layer demonstrate that the nonpolar conjugated polymer interacts poorly with the polar top face of the ZnO fibers and favorably with the nonpolar vertical faces of the ZnO nanofibers as seen in Figure 3.1. In the cross-sectional SEM image, the polymer appears to be floating above the ZnO fibers with little to no contact to the top surfaces. However, it is clear that where there is room enough between ZnO fibers, the polymer can be seen to flow into the structure and to branch out and attach to the sides of the ZnO fibers. This indicates that either the fiber spacing needs to be increased or the interfacial interactions need to be enhanced through surface modification. As a result of this inability to successfully infiltrate the polymer into the ZnO film, devices based on such structures demonstrate little to no photovoltaic effect.

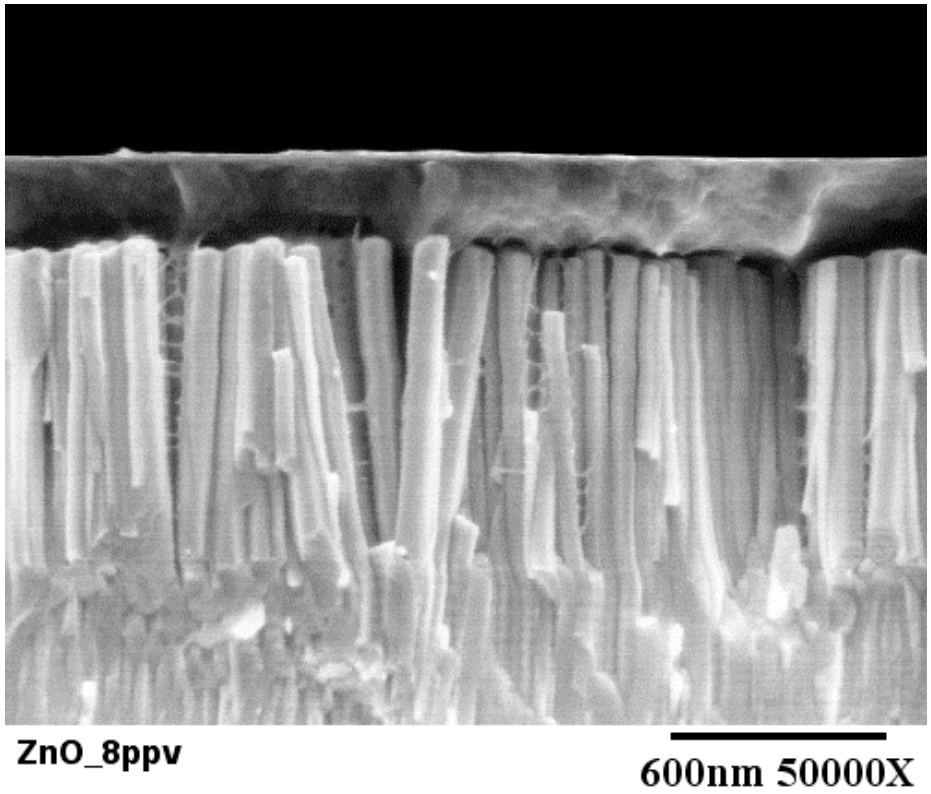

Figure 3.1 SEM image of MDMO-PPV spin coated onto ZnO nanofibers grown from a sputtered ZnO nucleation layer.

Poor device performance and polymer intercalation motivated the search for a method of fiber growth that might allow for more control of the ZnO nanofiber morphology. The development of the solution-based ZnO nucleation layer allows for more significant changes in nanofiber morphology as seen in Chapter 2. The spin coating of a 20 g/l P3HT solution in chloroform into ZnO nanofibers grown from ZnAc nucleation layers annealed for 5 minutes at 300 °C leads to significantly better intercalation as seen in Figure 3.2. The fiber spacing is much larger than in the previous example, which allows the polymer access to the nonpolar faces of the ZnO nanofibers, and in turn leads to increased intercalation of the polymer into the ZnO nanofiber film. Another important factor might be related to the disordered nature of the ZnO nanofibers.

If the polymer is presented with nonpolar faces instead of the polar top face of the ZnO fiber, the intercalation may be more favorable. In the polymer intercalated into ZnO nanofibers grown from sputtered ZnO, the polymer is only presented with the top polar faces of the ZnO fibers and intercalation is limited to areas of larger fiber spacing.

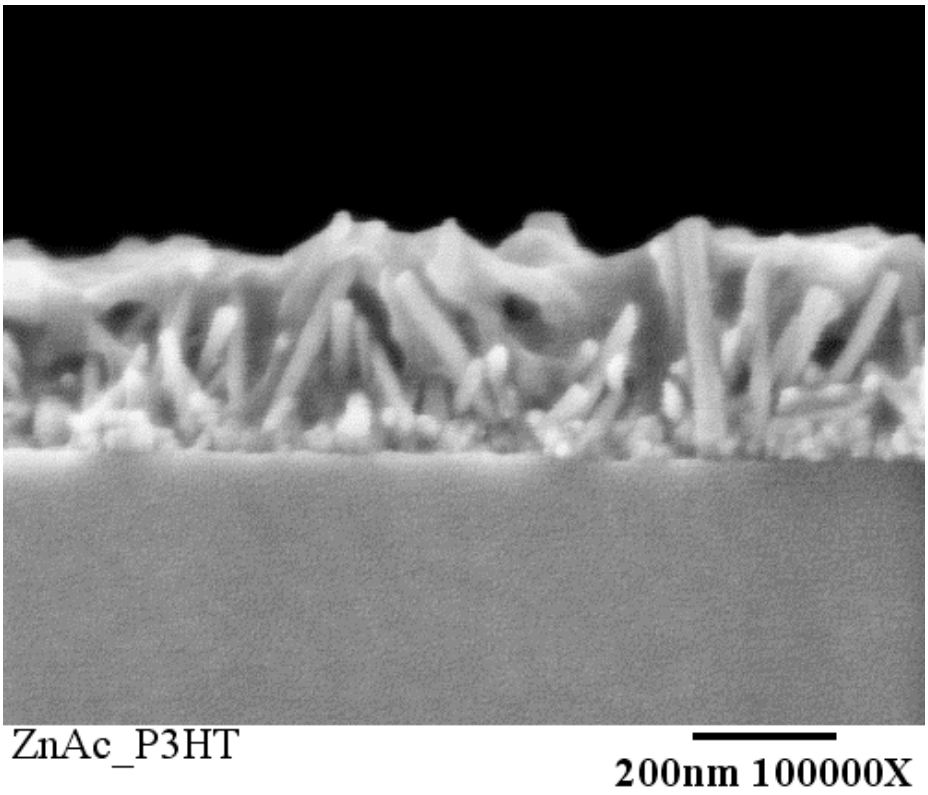

Figure 3.2 SEM image of P3HT spin coated onto ZnO nanofibers grown from a ZnAc nucleation layer annealed at 300 °C for 5 minutes.

The use of other surface treatments might help to improve the intercalation of the polymer into the ZnO nanofiber film. If the polymer were dissolved in a more polar solvent perhaps there would be improved interfacial interactions as well, due to

interactions of the polymer, the solvent, and the ZnO nanofibers. Polar solvents such as methanol can be added to chloroform solutions at low concentrations to maintain solvent miscibility. When methanol is added at 5 volume percent to a chloroform solvent, the new 20 g/l solution can be spin coated onto the ZnO nanofibers with success. There is increased intercalation of the polymer throughout the ZnO nanofiber film as seen in Figure 3.3. The polymer is also seen to intercalate deeper into the nanofiber film.

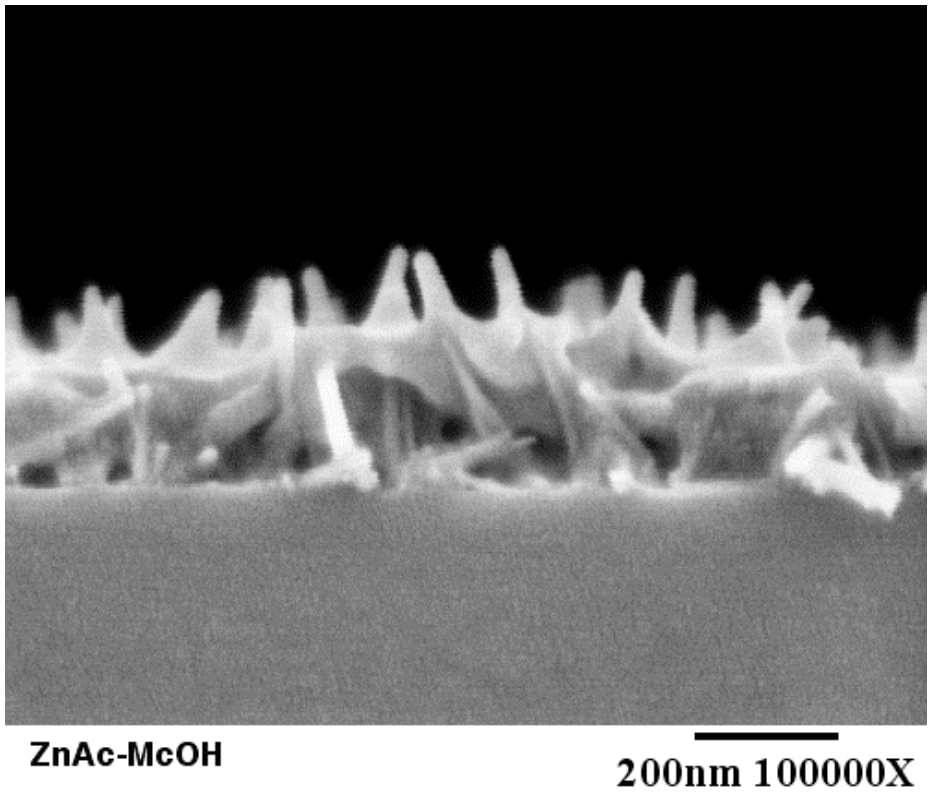

Figure 3.3 SEM image of P3HT solution in 5% methanol in chloroform spin coated onto ZnO nanofibers grown from a ZnAc nucleation layer annealed at 300 °C for 5 minutes.

The surface interaction between the polymer and the ZnO nanofibers can be significantly enhanced through surface modification of the ZnO with various wetting agents, such as chlorosilanes. Molecular treatments with chlorosilanes can create a covalently bonded monolayer on the surface of metal oxide materials through reaction with surface hydroxyl groups.[107] The chlorine atom will react with hydrogen creating HCl, which needs to be removed from the solution to minimize the HCl etching of the ZnO material. The result is a monolayer of the surface modifier with the silicon atom attached covalently to the oxygen atom on the surface of the metal oxide. If this were successful, the surface modifier would likely only bond to the top surface of the ZnO nanofibers, which are terminated with hydroxyl groups. This would leave the majority of the ZnO surface untreated while allowing enhanced polymer intercalation into the ZnO nanofiber film.

To treat the surface, the ZnO nanofiber sample was soaked in a dry 5% phenyltrichlorosilane solution in toluene followed by a toluene rinse. The P3HT was spin coated as above from a 20 g/l chloroform solution. The phenyltrichlorosilane treatment enhanced the degree of polymer intercalation substantially, as shown in Figure 3.4. The polymer is completely intercalated with few voids, indicating that the surface modification of the ZnO with phenyltrichlorosilane successfully tailors the interfacial interactions between the polymer and ZnO. Devices to date prepared with phenyltrichlorosilane-treated samples have, however, resulted in reduced photovoltaic performance. The devices pass no current through them, which could be the result of the formation of greater-than monolayer coverage on the ZnO surface. The ZnO could be etched by the HCl evolved from the reaction of the chlorosilane with the surface. However, devices exposed to HCl vapors resulted in increased current density and shorted devices. As such, the ZnO nanofiber devices presented hereafter do not use any chlorosilane-based wetting treatment.

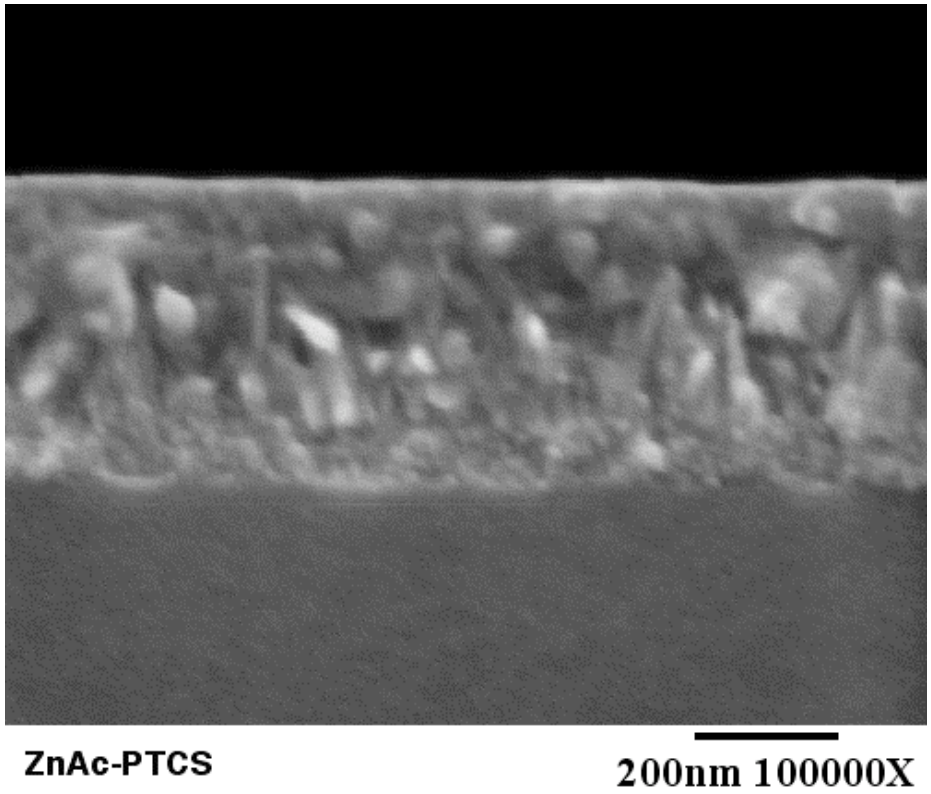

Figure 3.4 SEM image of P3HT intercalated into ZnO nanofibers treated with phenyltrichlorosilane. The ZnO nanofibers were grown from a ZnAc nucleation layer annealed at 300 °C for 5 minutes. The P3HT film was spin coated from a 20 g/l chloroform solution.

The charge transport properties of either material must not limit the device performance. The electron mobility in the single crystal ZnO nanofibers will be quite high (10 $cm^2\ V^{-1}\ s^{-1}$) as previously reported.[79, 80] However, the hole mobility in the conjugated polymer is of greater importance due to low hole mobilities ($<10^{-3}\ cm^2\ V^{-1}\ s^{-1}$) in available polymer donor molecules such as P3HT.[77] As mentioned previously, ordered polymer/inorganic devices can lead to reduced interchain ordering and hole mobility when confined in very small pores.[73, 75] Therefore, the absorption of the P3HT was measured in both an annealed film on glass and an annealed film intercalated into the

ZnO nanofiber film as seen in Figure 3.5. The interchain ordering in the P3HT film is maintained when intercalated into the nanostructured oxide acceptor, which is demonstrated by the shoulders in the absorption spectra at 560 and 600 nm. This is encouraging for devices fabricated from polymer/ZnO nanofiber composite devices, where hole transport will be important for increased device efficiency.

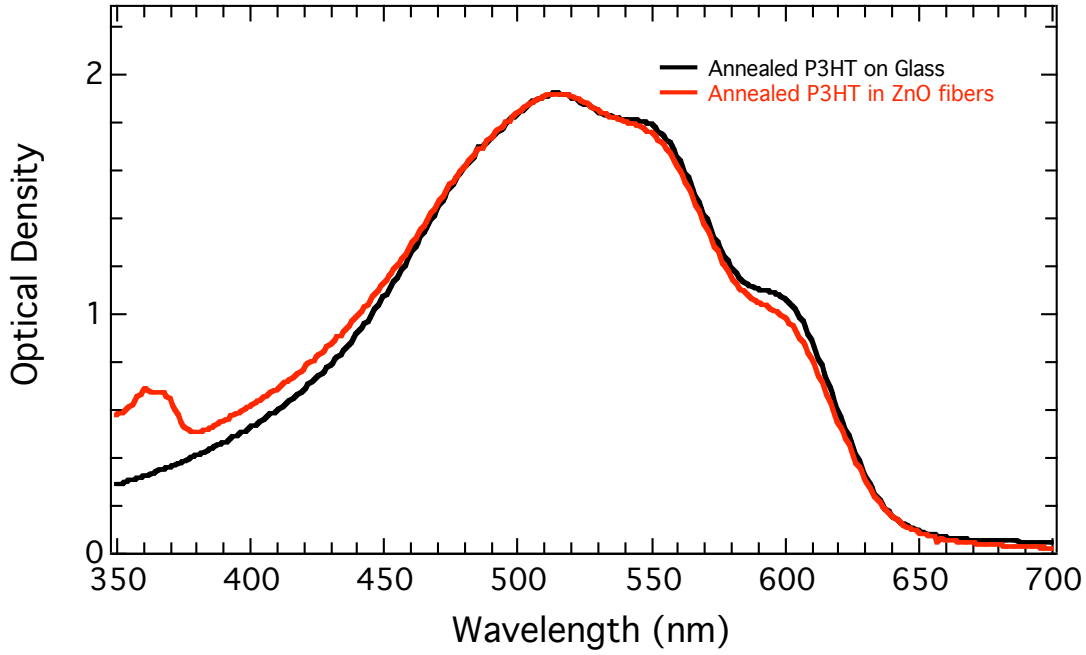

Figure 3.5 Absorption spectra for P3HT films spin coated on glass and intercalated into the ZnO nanofiber film grown from a ZnAc nucleation layer annealed at 300 °C for 5 minutes.

Ordered P3HT/ZnO nanofiber devices fabricated in this work do not yet demonstrate complete intercalation of the polymer into the ZnO nanofiber film. The

most successful intercalation has been the result of spin-coating the P3HT film on top of the ZnO nanofibers grown from a ZnAc nucleation layer annealed at 300 °C for 5 minutes. The polymer film was annealed at 200 °C for 2 minutes to melt the polymer and increase polymer intercalation. The device was completed by depositing a silver counter electrode on top. It was then tested and later used to gather cross-sectional SEM images as seen in Figure 3.6. Through this process the polymer is reasonably intercalated into the ZnO nanofiber film, though the nanostructured device does not demonstrate complete intercalation of the polymer into the ZnO pore structure. Nonetheless, functioning photovoltaic devices with good device performance were fabricated using this structure. This suggests that proper optimization of the interfacial interactions should increase performance beyond that obtained here.

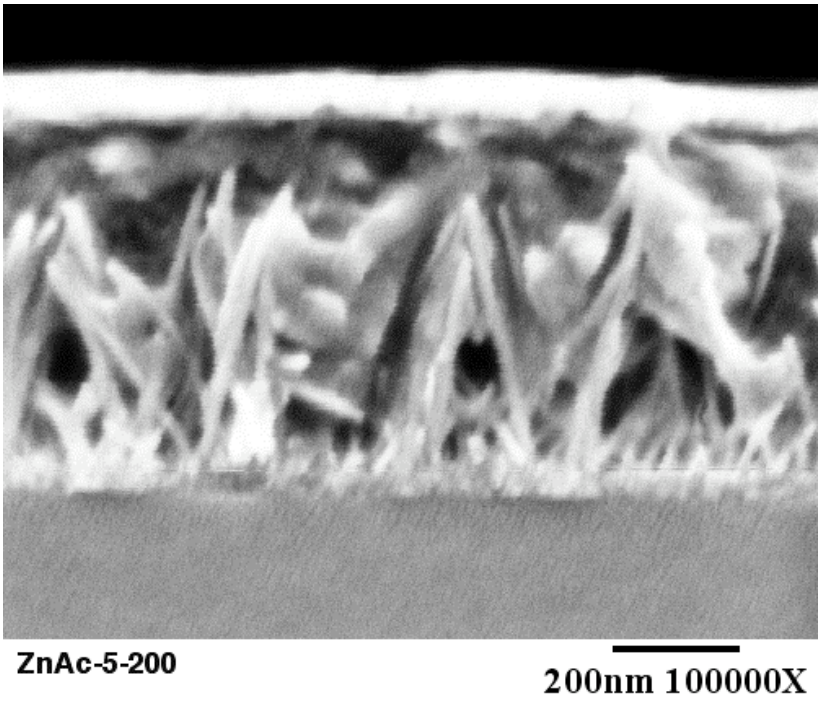

Figure 3.6 Cross sectional SEM image of ITO/ZnO/ZnO fiber/P3HT/Ag device.

3.4 Characterization of Solar Cell Performance

The photovoltaic performance of a solar cell can be evaluated by measuring the current-voltage characteristics in the dark and under illumination. A schematic plot of a current density (J) vs. voltage (V) curve is seen in Figure 3.7.

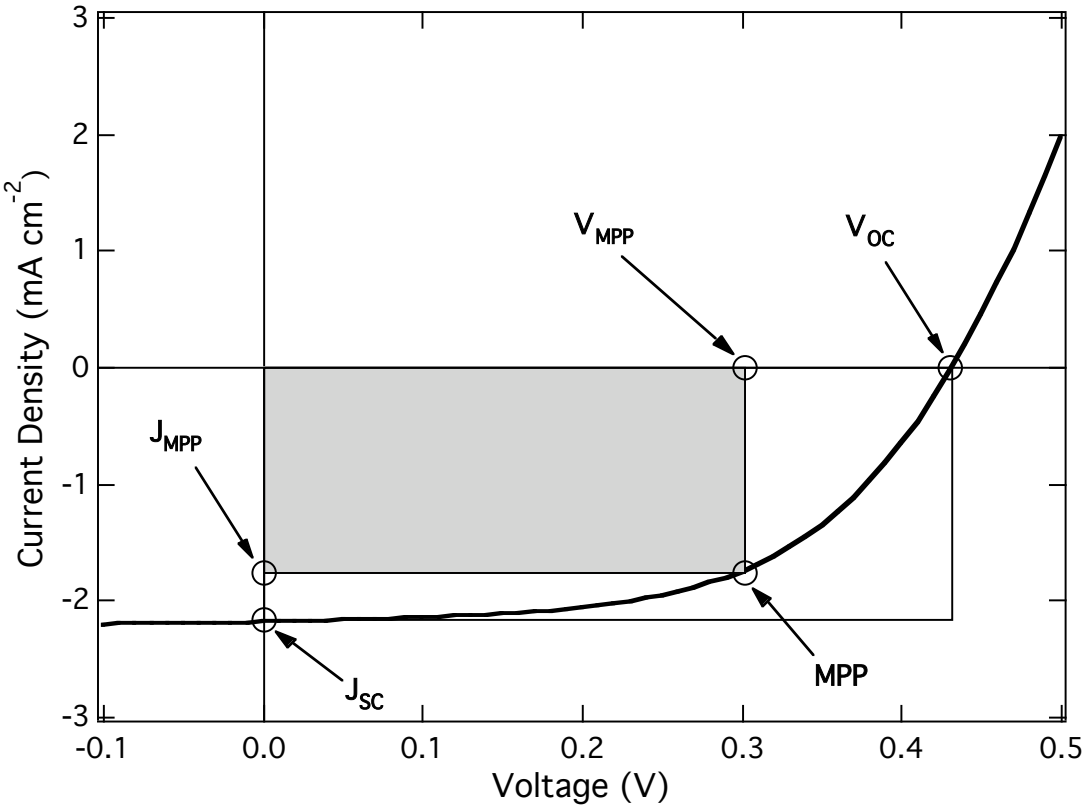

Figure 3.7 Schematic current density-voltage plot of a photovoltaic device under illumination, indicating several parameters that are important in the characterization the solar cells.

There are several important parameters that can be extracted from the J-V plot, from which the photovoltaic performance can be evaluated. The intersection of the J-V

curve with the horizontal axis is defined as the open circuit voltage (V_{OC}), the voltage at which the current density is zero. The V_{OC} can be related to the energy of the absorbed photon through $V_{OC} = V_{ph} - \Delta V$. Where ΔV is the voltage lost through the device operation. The intersection of the J-V curve with the vertical axis gives the short circuit current density (J_{SC}), the current density where the voltage is zero. The J_{SC} is directly related to both the overlap of the absorption spectrum of the device with the solar spectrum and the efficiency with which charges are generated and extracted from the device. Between the V_{OC} and the J_{SC}, there is one point where the power (J x V) is maximized. This point is the maximum power point (MMP), and is the reference point for the calculated maximum power or efficiency along the J-V curve. The fill factor (FF) can be defined as:

$$FF = \frac{J_{MPP} \times V_{MPP}}{J_{SC} \times V_{OC}} \tag{3.1}$$

The FF is related to the rectangle formed within the J-V curve with two of the edges lying along the axis. The corners are the origin, the MPP, the voltage at maximum power V_{MPP}, and the current density at maximum power J_{MPP}. The area of this rectangle is the numerator in the expression above. This is divided by the rectangle formed by the V_{OC} and J_{SC}. The resulting fraction or percent area is the FF. The FF characterizes how well the J-V curve allows for the extraction of charges from the device.

The efficiency (η) of the device is defined as:

$$\eta = 100 \times \frac{P_{out}}{P_{incident}} = 100 \times \frac{FF \times J_{SC} \times V_{OC}}{P_{incident}} \tag{3.2}$$

Where P_{out} is the power generated by the device at the MPP, and $P_{incident}$ is the power of the incident light in units of mW cm^{-2}, J_{SC} has units expressed in mA cm^{-2} and V_{OC} has units V. In a typical laboratory measurement, this value is an estimation of the actual "solar" efficiency because the incident power and emission spectra for any simulated light source are different from the solar spectrum. For purposes of comparing photovoltaic devices, standard solar spectra have been defined. For terrestrial applications, the solar spectrum is known as the AM1.5 spectrum. The AM1.5 (air mass 1.5) spectrum accounts for atmospheric absorption and screening and assumes the sun is at an angle of 41.8° above the horizon. This is equivalent to the light passing through atmosphere that is a factor of 1.5 thicker than when the sun is at a 90° angle to the horizon. The standard, 1-sun, intensity of the incident light on the device is 100 mW cm^{-2}. An accurate measurement of the AM1.5 efficiency requires a solar simulator with the proper spectrum and a calibrated photodiode as a reference for accurate measurement of the light intensity. A correction factor is necessary to account for the spectral mismatch between the device being measured, the absorption of the reference cell, the emission spectrum of the solar simulator and the actual AM1.5 spectrum.[108, 109]

Another important method for the characterization of photovoltaic devices is to measure the external quantum efficiency (EQE) or photoaction spectrum, which is also known as the incident photon to current conversion efficiency (ICPE). The EQE values are monochromatic efficiencies of the cell measured under short circuit conditions, which demonstrate the ratio of collected electrons out of the device to the number of incident photons at any given wavelength. The EQE can be measured as a function of wavelength and compared to the AM1.5 solar spectrum, as seen in Figure 3.8. It can be clearly observed that there is a great deal of the solar spectrum that the P3HT/PCBM system does not utilize.

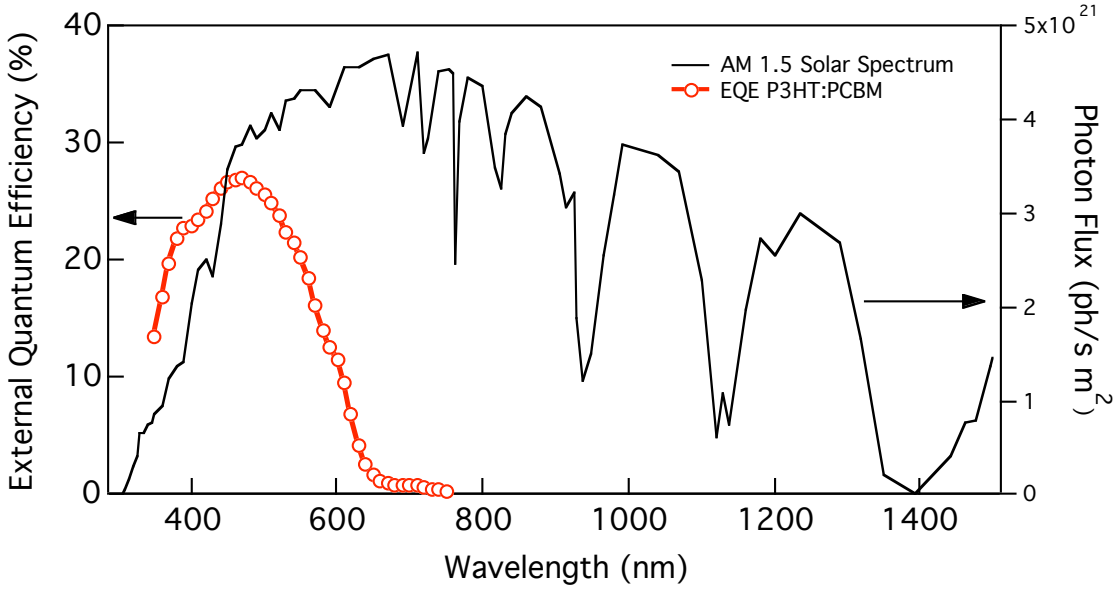

Figure 3.8 AM1.5 solar spectrum (solid) and EQE of P3HT/PCBM bulk heterojunction device (solid squares) as a function of wavelength. This device was prepared as part of the present study.

Photovoltaic measurements were carried out using our user facility Spectralab XT-10 solar simulator. It was calibrated for 100 mW cm^{-2} using a reference Si solar cell. The response of the reference cell is periodically calibrated against a P3HT-based organic solar cell that has been submitted to the NREL Measurements and Characterization division for certified measurement. This provides an approximate correction for the spectral mismatch factor,[108] but does not take into account day-to-day fluctuations in the lamp spectrum. Samples being tested were loaded into a device holder with a quartz window. The lamp intensity for the XT-10 measurements was set so that the reflection off the top surface of the window, which is approximately 9%, was taken into account, and the intensity of light incident on the surface of the device was 100 mW cm^{-2}. Measurements using the XT-10 used a 395 nm high pass UV filter, unless indicated otherwise, to eliminate unwanted photoexcitation of the ZnO with UV light.

Certified measurements performed by the NREL Measurements and Characterization division include a calculation of the spectral mismatch for each device measured. They do not take into account the reflection off the quartz window and do not use a 395 nm high pass filter. Current density–voltage (J–V) measurements were taken using a Keithley 238 high current source power meter. External quantum efficiency (EQE) spectra were determined using a calibrated Si photodiode reference, with a spot size smaller than the device area and intensity of 2 μW at 520 nm.

3.5 Selection of Counter Electrode for ITO/ZnO/P3HT/Metal Devices

The counter electrode must be a high work function metal in order to form an ohmic contact to the polymer. Both silver and gold have been used successfully as the anode in similar device configurations.[75, 76] To evaluate the performance of devices with a number of different anode materials, bilayer devices consisting of ITO/ZnO/P3HT/Metal were fabricated on the ZnAc nucleation layer without fibers grown. The metal contacts were all thermally evaporated in the same evaporator at 8 x 10^{-7} torr, with a deposition rate of 0.1 to 0.3 nm s^{-1} to a total thickness of 90 nm. In order to enhance the device performance, each of the devices was annealed at 120 °C for 10 minutes after fabrication in either argon (Al) or in air (Ag, Cu, and Au). In order to observe the effects of estimated work function on the device performance the metals employed in this study were Al, Ag, Cu, and Au with work functions of 4.28, 4.26, 4.65, and 5.1 eV respectively.[110-112] The J-V curves of these devices, as seen in Figure 3.9, demonstrate that Ag and Cu lead to the best performance, with Au performing well, and Al proving to be a poor contact to the polymer as anticipated. The performance of each of the devices with various metal anodes is summarized in Table 3.1. The Cu anode demonstrates a higher J_{SC} than Ag, however the lower V_{OC} compensates for this increase resulting in a similar efficiency. Based on the values of the work function, Au would be

expected to provide the best contact to the polymer, though this is not observed for these devices.

The work function might play less of a role in the device operation than anticipated, as there is little significant change in the device performance in going from the lower work function Ag anode to Cu, and the highest work function Au anode. The effect of dipoles at the metal/organic interface could help to explain the similar performance of the various metal electrodes, despite their differences in work function.[113] The high performance of the Ag and Cu materials, despite their relatively low reported work function values, might also be due to coordination of the metal with the sulfur atom in the thiophene ring.[114] The reaction of both Ag and Cu with the sulfur atom in the thiophene ring has been observed through x-ray photoelectron spectroscopy (XPS), with no reaction between the Au electrode and the sulfur.[114] It was observed that the greatest reaction occurs between Cu and the sulfur atom. Additionally, when the Cu or Ag electrode were heated at 150 °C for several hours, the signal for the reacted metal atoms increased dramatically indicating diffusion of the metal atoms into the polymer film. Based on these results, both Ag and Cu electrodes make excellent contact to the devices in this configuration. Due to the lower series resistance in these bilayer devices, Ag electrodes were used throughout the rest of this work.

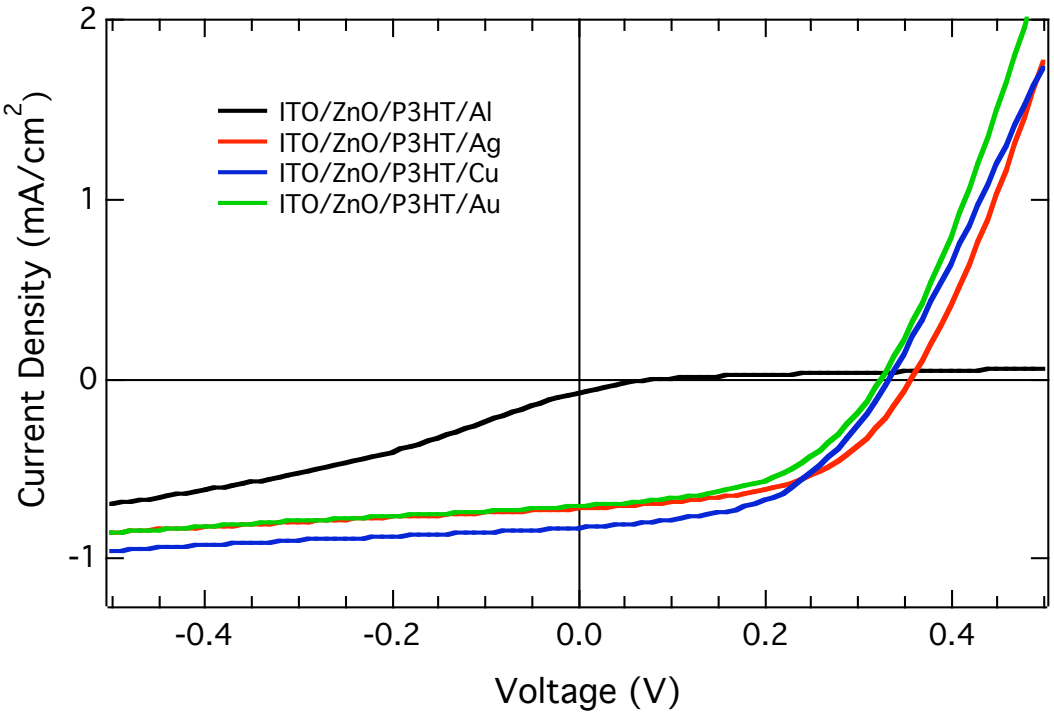

Figure 3.9 Current density versus voltage (J-V) for ITO/ZnO/P3HT/Metal bilayer devices for different metal anodes. Bilayer devices were under AM1.5 illumination, with Al anode (black), Ag anode (red), Cu anode (blue) and Au anode (green), respectively.

Table 3.1 Photovoltaic performance of bilayer devices based on ITO/ZnO/P3HT/Metal showing devices with Al, Ag, Cu and Au anodes.

Anode	V_{OC} (mV)	J_{SC} (mA cm^{-2})	FF (%)	η (%)
Al	**102**	**0.08**	**18**	**0.001**
Ag	**360**	**0.73**	**52**	**0.14**
Cu	**335**	**0.83**	**51**	**0.14**
Au	**327**	**0.71**	**50**	**0.12**

3.6 Effect of Atmosphere on Polymer/ZnO Nanofiber Device Performance

The photovoltaic performance of the polymer/ZnO nanofiber devices was observed to be dependent on the processing conditions and environments for this study. The P3HT/ZnO nanofiber devices were based on a ZnAc nucleation layer annealed at 300 ˚C for 5 minutes. ZnO fibers were then grown to a length of about 400 nm, rinsed, and dried at 200 ˚C for 30 minutes in air. The P3HT layer was spin coated in the glove box at 800 RPM from a 30 g/l P3HT solution in chloroform. The polymer film was then annealed at 200 ˚C for one minute followed by a 5 minute anneal at 120 ˚C. Finally, the Ag electrode was evaporated and the devices were characterized in argon. When the nanofiber devices were characterized through the measurement of J-V curves under illumination and without exposure to air, they were shorted with little diode effect.

After storing separate devices in argon and air for one day, the performance decreased for the device stored under argon and increased when stored under air as seen in Figure 3.10. After three days in argon, the device continued to decrease in performance. The performance of the device stored in air for three days, however, increased substantially. The J-V curves in Figure 3.10 indicate that the performance of the device stored in air increases through both an increase in the shunt resistance and a decrease in the series resistance, leading to increased FF and V_{OC} values. It is well known that oxygen vacancies are intrinsic electron donors in ZnO.[115, 116] These vacancies may be quenched when stored in air or pure oxygen, and the semiconductor properties improve as both the oxygen vacancy and carrier concentrations are reduced. Devices stored in argon would tend to increase in oxygen vacancy density, which would increase the carrier density in the ZnO nanofibers and reduce the device performance. This agrees with the reduction of the series resistance and a decrease in the shunt resistance in the J-V curves. When the ZnO nanofibers were annealed at 300 ˚C for one hour prior to the spin coating the polymer film, the behavior was similar to the 200 ˚C drying step used in the presented data.

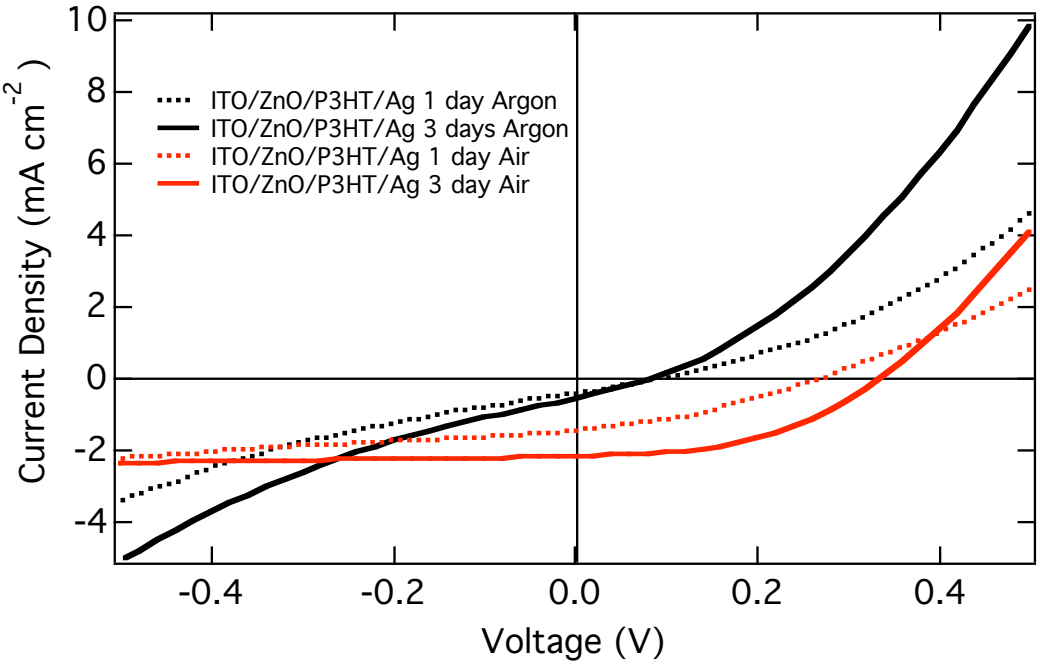

Figure 3.10 Current density versus voltage (J-V) for ITO/ZnO/ZnO fibers/P3HT/Ag devices aged in argon (black), and air (red). Aging in argon one day (black dot), argon three days (solid black), air one day (red dot), air three days (solid red).

When the polymer/ZnO nanofiber device is stored in air for longer periods of time, the performance increases dramatically. This is shown in Figure 3.11 for a single device measured after 3, 4, 5 and 6 days. The aging of the devices stored in air proved problematic as the device had to be characterized over the course of a week to determine the maximum performance. This input was needed before another set of processing conditions could be tested. To accelerate the aging process, the devices were annealed at various times and temperatures in air. Though the annealed devices improved from their as-deposited performance, they did not demonstrate improved performance over the devices aged at room temperature for six days.

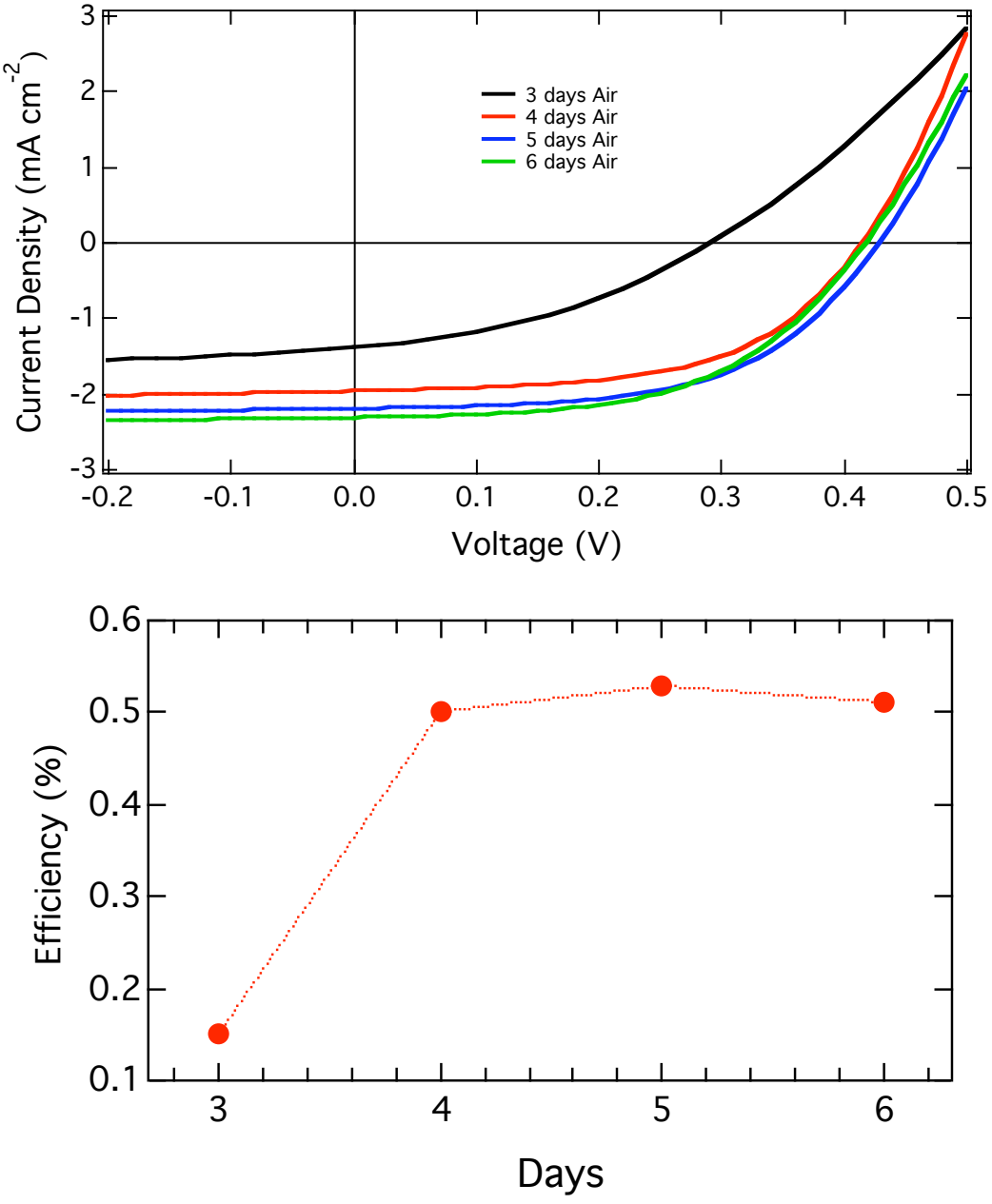

Figure 3.11 Current density versus voltage (J-V) for ITO/ZnO/ZnO fibers/P3HT/Ag device aged in air for 3 days (black), 4 days (red), 5 days (blue) and 6 days (green), top graph. Device efficiency versus aging time in air, bottom graph.

To determine if oxygen could be changing the metal back contact, devices were fabricated with both silver and gold counter electrodes. The Au electrode is not expected to react significantly with oxygen. However when exposed to air, Ag may form silver oxide. However, both the devices with Ag and Au demonstrate identical aging behavior when exposed to air. In addition, separate devices fabricated with either P3HT or MDMO-PPV demonstrate increased efficiency with aging in air. The doping of P3HT by oxygen has been observed,[117, 118] which could enhance the charge separation through the formation of a p-n junction at the interface with ZnO. This effect was not observed, and both polymer devices exhibited the same behavior with aging. These results support the argument that the reduction of oxygen vacancies in the ZnO material may lead to increased device performance.

A reduction of the oxygen vacancy defect density and corresponding decrease in the carrier density and conductivity in ZnO thin films has been observed previously after annealing the ZnO films in air or oxygen at elevated temperatures.[119] At high temperatures, the defects can diffuse rapidly, allowing their concentrations to reach equilibrium values. However, at room temperature this observation is particularly interesting and may be related to the increased surface area of the ZnO nanofiber films. The concentration of intrinsic donors, such as oxygen vacancies, depends on how the sample has been treated. The defect concentration is particularly sensitive to the temperature and the partial pressures of Zn(g) and O_2(g).[116] The oxygen in ZnO is in equilibrium with the partial pressure of oxygen and the concentration of oxygen vacancies:[116]

$$O_O^x \Leftrightarrow \frac{1}{2} O_2(g) + V_O^x. \qquad (3.3)$$

The rate constant for the process in equation (3.3) is:[116]

$$K_{O_2} = [V_O^x] p_{O_2}^{1/2} = 3.87 \times 10^{30} e^{-4.29\beta} (atm^{1/2} cm^{-3}), \quad (3.4)$$

where $[V_O^x]$ is the concentration of oxygen vacancies, p_{O_2} is the partial pressure of O_2 gas, and $\beta = (k_B T)^{-1}$ in units of $(eV)^{-1}$. Therefore, the concentration of oxygen vacancies is given by:[116]

$$[V_O^x] = K_{O_2} p_{O_2}^{-1/2} \quad (3.5)$$

Based on these calculations at room temperature in air with an oxygen partial pressure of 0.2 atm, the oxygen vacancy concentration in a pristine bulk ZnO material would be 470 cm^{-3}. However, the oxygen partial pressure is reduced to 10 mTorr (10^{-5} atm) when transferring the ZnO nanofiber films through the antechamber and into the glove box for spin coating of the polymer film. At room temperature and this oxygen partial pressure, the oxygen vacancy concentration increases over two orders of magnitude to 58,000 cm^{-3} for bulk ZnO. This increase in the oxygen vacancy concentration would lead to a dramatic increase in the carrier concentration and the conductivity in the ZnO nanofibers if the same change in two orders of magnitude was observed from the base level of the carrier density. The effect of the increased surface area of the ZnO nanofibers should make this a conservative estimate. The increase in carrier density could be related to surface defects. Surface area dependence of the defect density of ZnO nanofibers has been observed previously.[104] The green PL emission, which is associated with oxygen vacancies in ZnO,[115] increased dramatically as the ZnO fiber diameter was decreased from 250 nm to 50 nm.[104] Based on the calculations above for bulk ZnO, the observed effect of atmosphere on the ZnO nanofiber films may be explained by the exposure of the nanofibers to vacuum, which may be detrimental to the device performance.

Based on these observations, devices were fabricated by spin coating the polymer film onto the ZnO nanofiber film in air, outside of the glove box. This helps to eliminate

the delay between fabrication and characterization of the devices. The devices fabricated in air demonstrated higher performance as seen in Figure 3.12 for typical devices prepared in air and in argon. As a result, all of the devices presented subsequently have been fabricated, stored, and characterized in air unless otherwise noted.

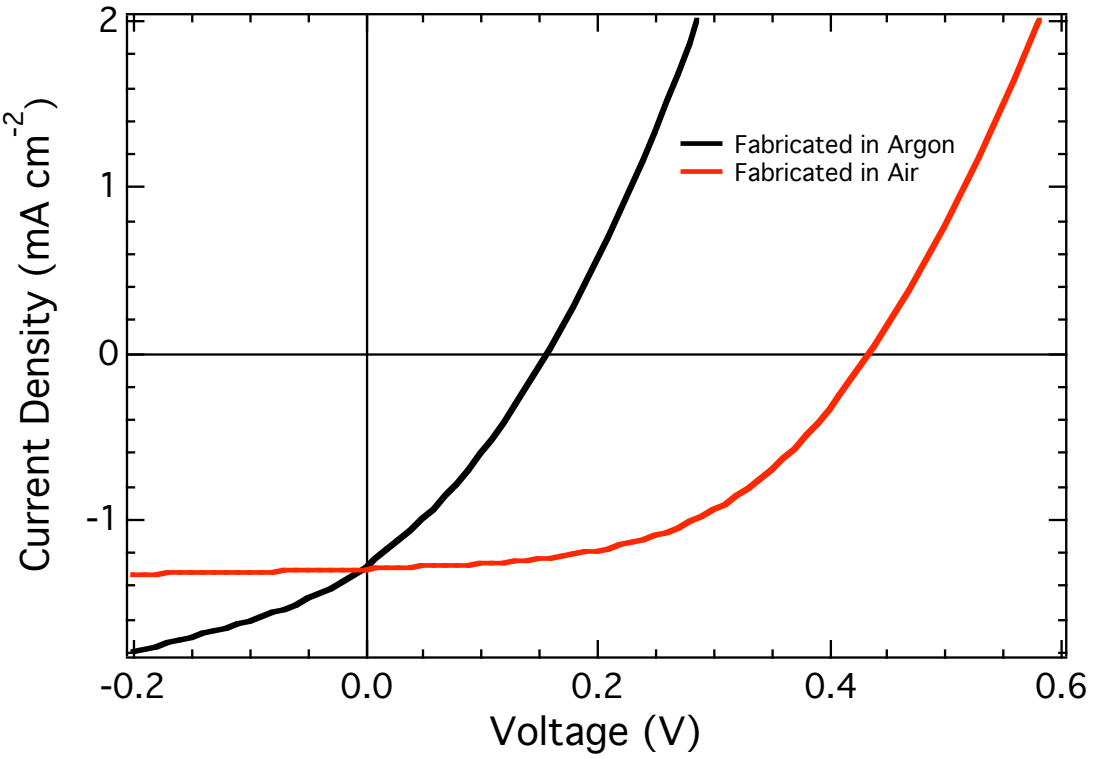

Figure 3.12 Current density versus voltage (J-V) for ITO/ZnO/ZnO fibers/P3HT/Ag devices spin coated in argon in (black) and in air (red).

3.7 Photovoltaic Performance of Bilayer vs. ZnO Nanofiber Device

In order to observe the effect of the nanostructured oxide interface on the photovoltaic device performance, the nanostructured hybrid device was compared to a planar (bilayer) device. The photovoltaic performance of the devices was characterized under simulated AM1.5 illumination using a Spectrolab XT-10 solar simulator. The measurement was made with a 395 nm high pass UV filter inserted in front of the device to prevent photoexcitation of the ZnO. J-V curves for both the bilayer and nanofiber ZnO devices are shown in Figure 3.13. The bilayer device of P3HT on the planar ZnO nucleation layer exhibited a V_{OC} of 501 mV, a J_{SC} of 0.52 mA/cm^2, a FF of 55%, and a η of 0.15%. The performance of the nanostructured hybrid device was significantly improved with values for the V_{OC}, J_{SC}, FF, and η of 440 mV, 2.17 mA/cm^2, 56%, and 0.53%, respectively. This represents more than a 3-fold increase in power conversion efficiency, which is largely related to the higher J_{SC}. A higher J_{SC} is expected as a result of increased interfacial area of the heterojunction between the ZnO and the P3HT.

The performance is improved compared to previous attempts by other groups using nanostructured TiO_2, where J_{SC} values were much smaller.[75, 76] To verify the efficiency of the nanostructured device, the nanostructured device was submitted to the NREL Measurements and Characterization group for certified measurement, the results of which are shown in the inset to Figure 3.13. These measurements do not take into account reflections off the face of a quartz window in our sample holder, which reflects approximately 9% of the incident light and does not use a UV filter to prevent photoexcitation of the ZnO. The results yield values for the V_{OC}, J_{SC}, FF, and η of 429 mV, 2.13 mA/cm^2, 48.4%, and 0.44%, respectively.

The certified measurement was performed without a UV filter, and the decreases in the V_{OC} and FF in the certified measurement are attributed to photoexcitation of the ZnO, which destabilizes the device. While the exact nature of this destabilization is unclear, a possible explanation is that photoexcitation of the ZnO leads to an increase of

the defect density on the surface of the ZnO that acts to increase carrier recombination at the ZnO/P3HT interface. These changes are reversible, however. Leaving the device in air in the dark for several hours restores the original V_{OC} and FF prior to UV exposure. Therefore, the photooxidation of the P3HT at the ZnO surface is not a reasonable explanation, since this would lead to permanent changes in device performance. Interestingly, the ZnO/P3HT bilayer devices do not show this sensitivity to UV exposure. This may be a result of the decreased surface area of the ZnO/P3HT interface, or the surface chemistries of the ZnO derived from a ZnAc precursor in the nucleation layer as opposed to the zinc nitrate precursor used in the nanofibers.

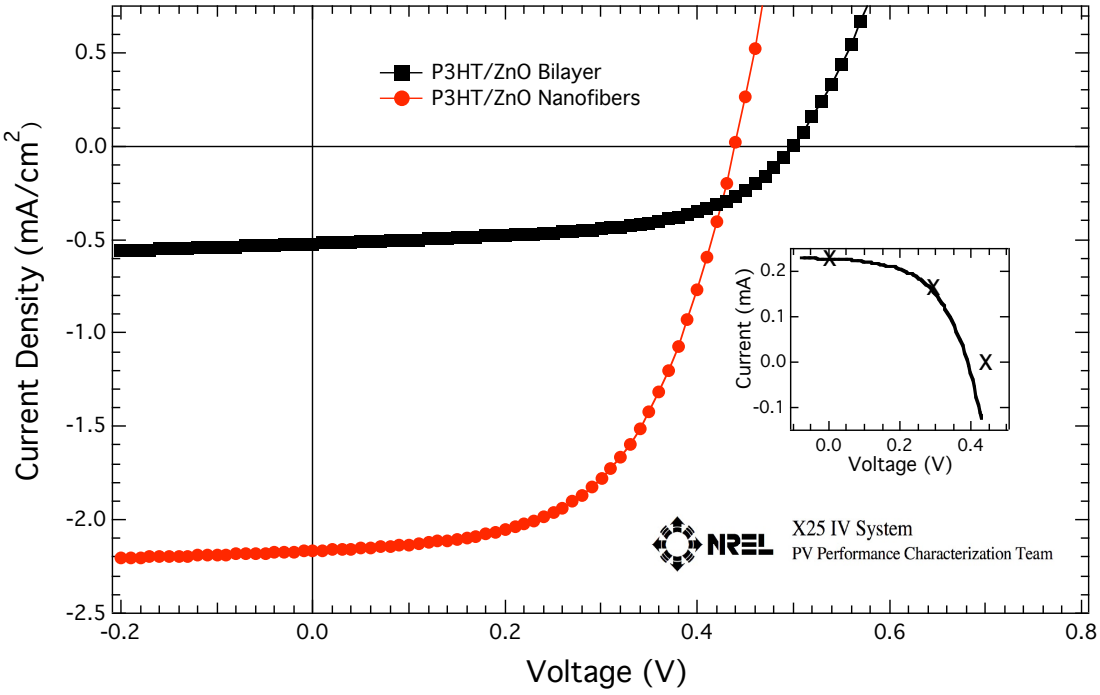

Figure 3.13 Current density versus voltage (J-V) for a typical ITO/ZnO/P3HT/Ag bilayer device (black squares) and ITO/ZnO fiber/P3HT/Ag device (red circles). Inset shows NREL certified measurement data.[120]

The external quantum efficiency (EQE) spectra for both the bilayer ITO/ZnO/P3HT/Ag and the nanostructured ITO/ZnO fibers/P3HT/Ag devices were measured and are compared to the absorption spectrum for a corresponding nanostructured composite film as seen in Figure 3.16. Both devices demonstrate overlap of the photoaction spectra with the absorption spectrum. However, the action spectra for both devices indicate that much of the light absorbed is not converted to charge carriers, likely due to the large spacing between fibers (100 nm) and the short exciton diffusion length found in P3HT (3-5 nm).[21] The bilayer device produced a maximum EQE of 6.2% at 510 nm, corresponding to a J_{SC} of 0.52 mA/cm^2. The nanostructured ZnO fiber device achieved a maximum EQE of 18.3% at 520 nm corresponding to 2.1 mA/cm^2. The peak in both EQE spectra at 360 nm is the result of UV light absorption by the ZnO and subsequent hole transfer to the P3HT, which demonstrates clear contributions to the photocurrent from light absorption in both the P3HT and ZnO materials. Integration of the measured spectral response of the nanostructured device with the AM 1.5 solar spectrum (100 mW/cm^2) results in an estimated J_{SC} of 2.06 mA/cm^2, which agrees very well with the observed white light J_{SC} above. The normalized EQE spectra of both devices indicate that there is a small red shift in the photoresponse of the nanostructured device as seen in the inset of Figure 3.16. This red shift in the EQE of polymer/ZnO nanofiber device could be due to increased molecular order of the P3HT chains along the vertical surface of the nanofibers.

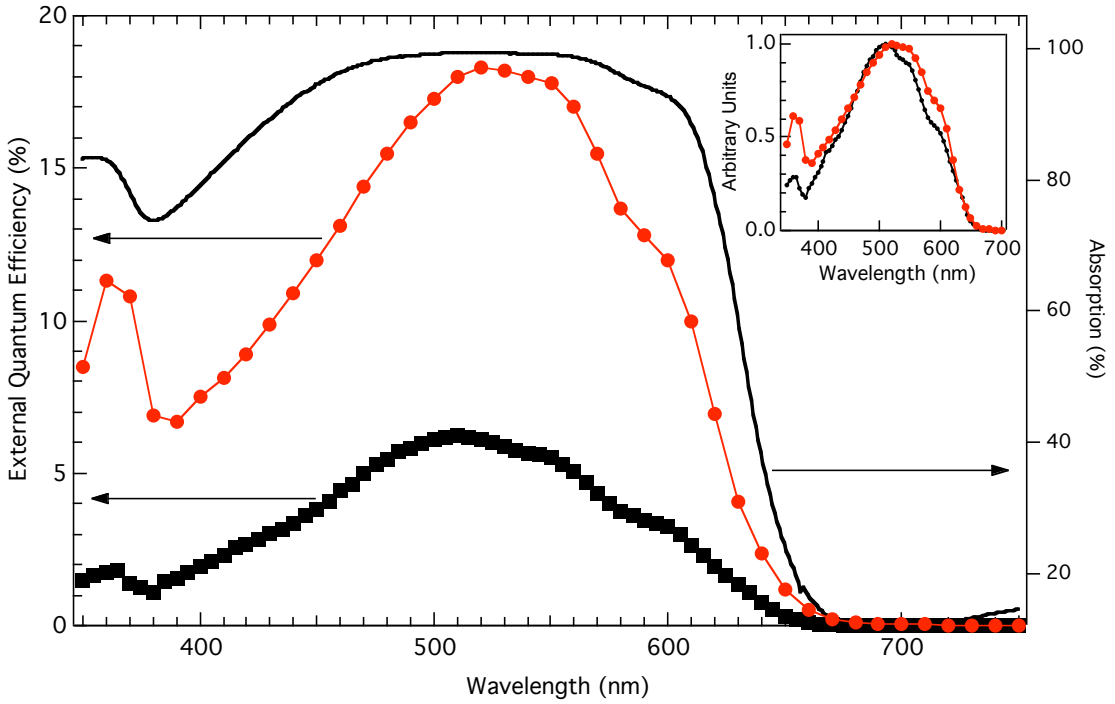

Figure 3.16 External quantum efficiency of ITO/ZnO/P3HT/Ag bilayer device (black squares), ITO/ZnO fibers/P3HT/Ag nanostructured device (red circles) and UV-vis absorption spectrum of the nanostructured device (solid line). Inset shows normalized spectra.[120]

There are several possible routes to improving the performance of the nanostructured devices. First, the V_{OC} is lower than expected from this donor–acceptor pair. Bulk heterojunction devices using a common donor polymer such as poly[2-methoxy-5-(3',7'-dimethyloctyloxy)-1,4-phenylene vinylene] (MDMO-PPV) blended with PCBM as an acceptor have demonstrated similar V_{OC} values to hybrid blend devices using ZnO nanoparticles.[35, 66] Devices consisting of blends of P3HT and PCBM have yielded a V_{OC} of approximately 600 mV, therefore a similar V_{OC} might be expected in these devices. The reason the V_{OC} seen in the device is substantially lower than this is not clear, but possible explanations include the presence of mid-gap states on the surface of the ZnO that pin the Fermi level; or that the electron mobility of the ZnO nanofibers

could actually be too high, resulting in increased carrier recombination at the ZnO/P3HT interface and a reduced V_{OC}. Further studies are necessary to better understand these phenomena.

Secondly, the spacing between the ZnO nanofibers as grown is on the order of 100 nm. This is substantially larger than the typical exciton diffusion length in P3HT, which is presumed to be less than 10 nm. It is not clear how ordering of the P3HT chains inside the pores of the ZnO may affect this. This suggests that closer spacing of the fibers may yield a larger J_{SC} and thereby increase the J_{SC} and EQE to values similar to present P3HT/PCBM bulk heterojunction devices.

3.8 Effect of ZnO Nanofiber Spacing and Length on Device Performance

To decrease the fiber spacing, the ZnAc nucleation layer can be annealed for 30 minutes, which results in more vertical ZnO nanofibers with decreased spacing. The decrease in the fiber spacing should be reflected in an increase in the heterojunction interfacial area, which will increase the J_{SC} in the device and lower the series resistance in the device. It was found, however, that devices made with fibers grown on ZnAc nucleation layers annealed for 30 minutes demonstrated reduced performance as seen in Figure 3.14, despite having a higher density of ZnO fibers than fibers. The V_{OC} is reduced more dramatically than the J_{SC} perhaps as a result of reduced surface state passivation by the intercalation of the polymer into the ZnO nanofiber film. This is believed to be a result of poor wetting by the P3HT in the case of more ordered fibers grown, as there was not wetting treatment used to enhance wetting of the polymer in the ZnO nanofiber film. This can be explained by the polarity of the ZnO fiber surfaces. As discussed in section 3.3, the top (002) surface of the fiber is polar, which is likely to inhibit polymer intercalation.

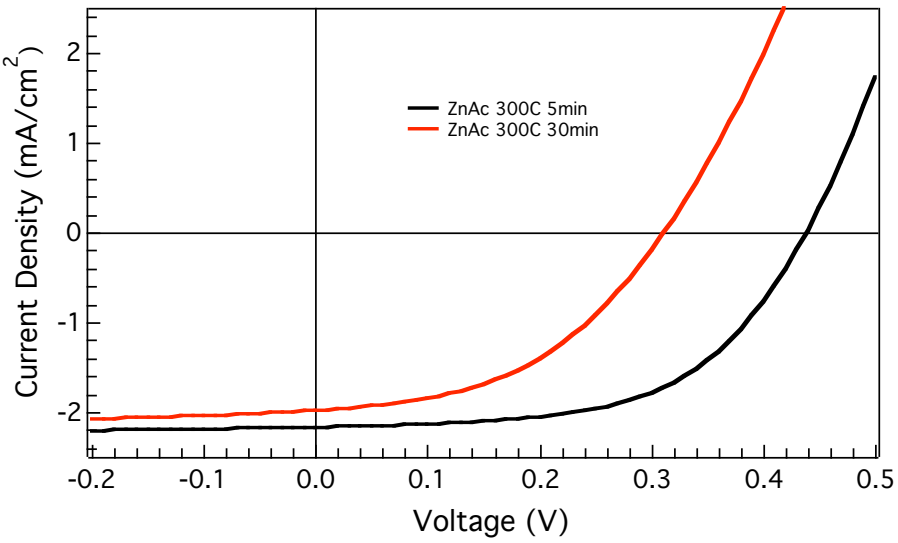

Figure 3.14 Current density versus voltage (J-V) for ITO/ZnO/ZnO fibers/P3HT/Ag with ZnO fibers grown for 20 minutes and ZnAc nucleation layer annealed at 300 °C for 5 minutes (black) and for 30 minutes (red).

Another way to improve performance involves modifying the ZnO nanofiber length to optimize the active layer thickness. In this study, devices were fabricated with ZnO nanofiber lengths of about 500 nm and 250 nm by decreasing the growth time from 20 minutes to 10 minutes, respectively. In polymer/fullerene blend devices, as the film thickness decreases, the optical density of the active layer decreases and there is a corresponding reduction in the J_{SC}. At the other extreme, as these blend devices increase in thickness to greater than 250 nm, efficiency is often limited by charge transport out of the device and, as a result, the efficiency will decrease. However, the ordered polymer/ZnO nanofiber devices increase in efficiency as the active layer thickness increases up to 500 nm, as seen in Figure 3.15. The J_{SC} increases from 1.29 mA cm^{-2} for the 250 nm ZnO nanofiber device to 2.17 mA cm^{-2} for the 500 nm ZnO nanofiber device.

The J_{SC} increases despite the charges needing to travel greater distances before being extracted from the device. This is not a general observation for ordered

polymer/inorganic devices. In fact, for devices based on P3HT and mesoporous TiO_2, the opposite was observed at very low optical densities.[75] Efficient charge transport out of the P3HT/ZnO nanofiber device could be related in part to the increased electron mobility in the ZnO nanofibers. However, the hole mobility of the polymer should be the limiting factor. One would expect that increasing the hole mobility of the polymer would increase the device performance. Improved charge transport has been observed, as noted earlier, in composite devices of P3HT intercalated into vertical pores in Al_2O_3, where the polymer chains are aligned preferentially in the direction of charge transport. The hole mobility of the polymer may be enhanced through this process in the polymer/ZnO nanofiber composites as well. This might lead to the observed increase in performance with the relatively thick active layers used in this study.

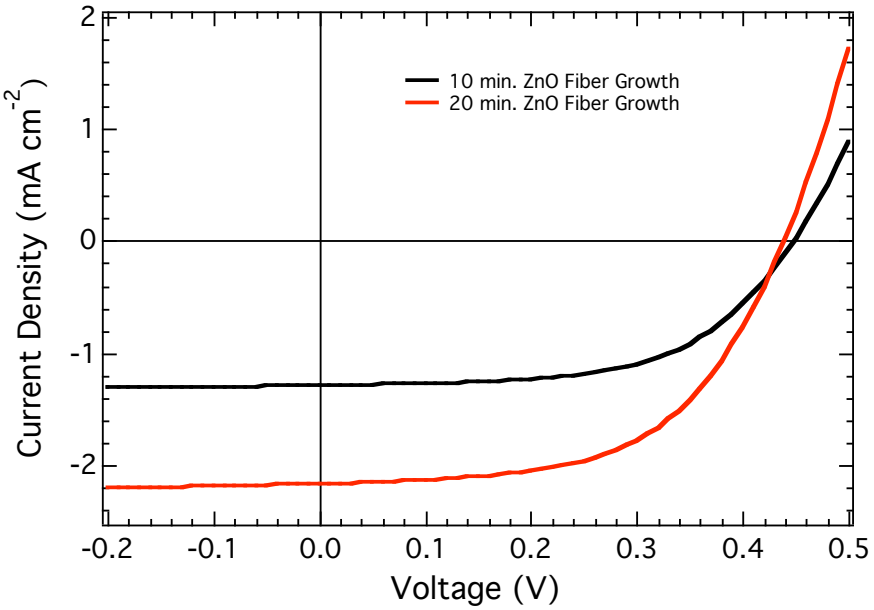

Figure 3.15 Current density versus voltage (J-V) for ITO/ZnO/ZnO fibers/P3HT/Ag with ZnAc nucleation layer annealed at 300 °C for 5 minutes and ZnO nanofibers grown for 10 minutes (black) and for 20 minutes (red).

3.9 Dependence of Photovoltaic Performance on Light Intensity

Additional, J-V measurements were taken at light intensities ranging from 0.25 suns (25 mW/cm^2) to 2.5 suns (250 mW/cm^2) as seen in Figure 3.17. In this typical device, the data indicate that the efficiency increased from 0.40% to 0.61% at 0.25 and 2.5 suns, respectively. The short circuit current density increases linearly with intensity up to 200 mW/cm^2 ($J_{SC} \propto I^{\sim 1}$), indicating that charge carrier losses are dominated by monomolecular recombination. However, above 200 mW/cm^2 the relationship between J_{SC} and intensity becomes super linear. The increase in V_{OC} is greater than the logarithmic relationship that is anticipated. These observations might be explained through increased trap filling at higher light intensities or through tunneling, or potential drops at the interfaces. The direction of the measurements was from low to high intensity, but the same observations were seen in measurements made from high to low intensity. Increased efficiencies at higher light intensities have been demonstrated in small molecule-based photovoltaic devices when the series resistance is carefully minimized.[121] However, this observation is rare for polymer photovoltaic devices, which often exhibit their best efficiency at intensities of about 1-sun (100 mW/cm^2), indicating a possible advantage in this hybrid device architecture.

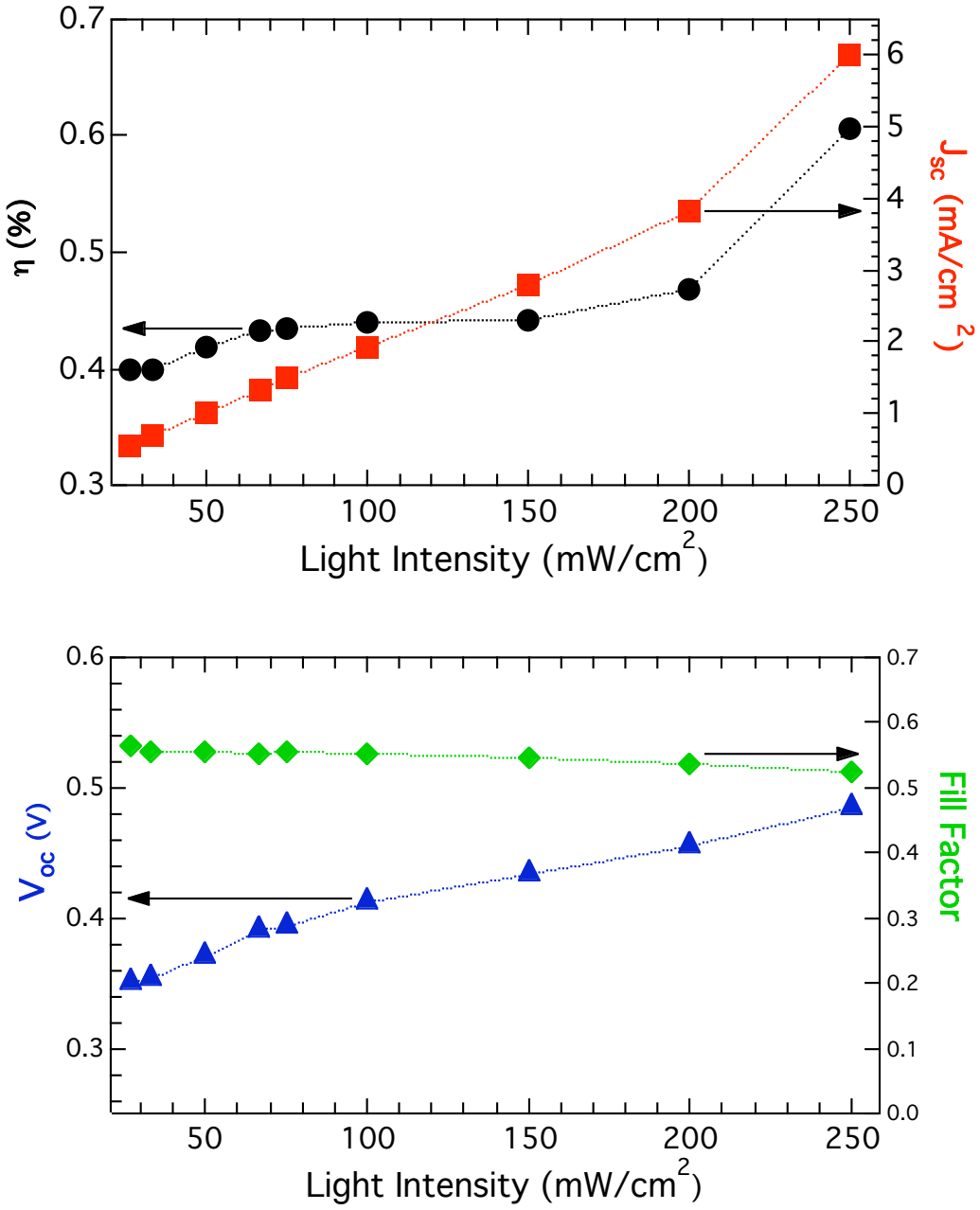

Figure 3.17 Photovoltaic performance vs. illumination intensity of the nanostuctured hybrid device. Power conversion efficiency and short circuit current vs. intensity (top), open circuit voltage and fill factor vs. intensity (bottom). Intensity was varied by changing the distance from the lamp on a Spectralab XT-10 solar simulator (AM 1.5).[120]

3.10 Increasing Exciton Dissociation Through P3HT:PCBM/ZnO Nanofiber Devices

In order to dissociate more of the photogenerated excitons in the film and increase the J_{sc} of the cell, a blend of P3HT and PCBM was intercalated into the ZnO nanofiber structure. The resulting device resembles the commonly studied polymer/fullerene device, except that the device structure is inverted in terms of current collection relative to standard polymer/fullerene devices. ZnO nanofibers also penetrate into the blend morphology. The device was fabricated on ZnO nanofibers grown from a ZnAc nucleation layer annealed at 300 °C for 5 minutes. After drying of the nanofiber films, a 40 g/l solution of a 1:1 chloroform:chlorobenzene solvent mixture with a 1:1 ratio of P3HT to PCBM by weight was spin coated onto the substrates at 750 RPM. The devices were then annealed in air at 110 °C for 10 minutes and aged in air for several days prior to characterization. The performance of the ITO/ZnO/ZnO fiber/P3HT:PCBM/Ag device was significantly better than for similar devices without PCBM, demonstrating values for the V_{oc}, J_{sc}, FF and h of 475 mV, 10.0 mA/cm^2, 0.43, and 2.0%, respectively. The J-V curves are shown in Figure 3.18. The incorporation of PCBM into the P3HT results in efficient exciton dissociation and nearly a factor of five increase in J_{sc} over the device with neat P3HT.

Since there is an electron transfer step from the PCBM to the ZnO, the V_{OC} would likely decrease due to the additional loss of potential. However, an increase in the V_{OC} is observed in the P3HT:PCBM/ZnO nanofiber device. The defects in the ZnO may not be able to serve as recombination centers when dissociation does not take place at the ZnO surface. This result demonstrates efficient electron transfer from PCBM to ZnO, as there are no direct pathways for electrons to be transferred from PCBM to the underlying ITO without first being transferred to either the ZnO nucleation layer or the ZnO nanofibers. Studies of P3HT:PCBM blends deposited onto planar ZnO nucleation layers grown from the ZnAc precursor (as discussed below) have shown efficient electron transfer from PCBM to this layer. At the moment, it is not certain that the electrons are transferred

from PCBM to the ZnO fibers, since the fibers and the nucleation layer may have different electronic properties on their surfaces owing to the different precursors used in their growth. Future studies of this issue are necessary for confirmation of the mechanism for electron transport out of the device. Interestingly, with the overall performance improved with added PCBM, the fill factor of the device is negatively affected, which is likely related to the blend morphology not being optimized.

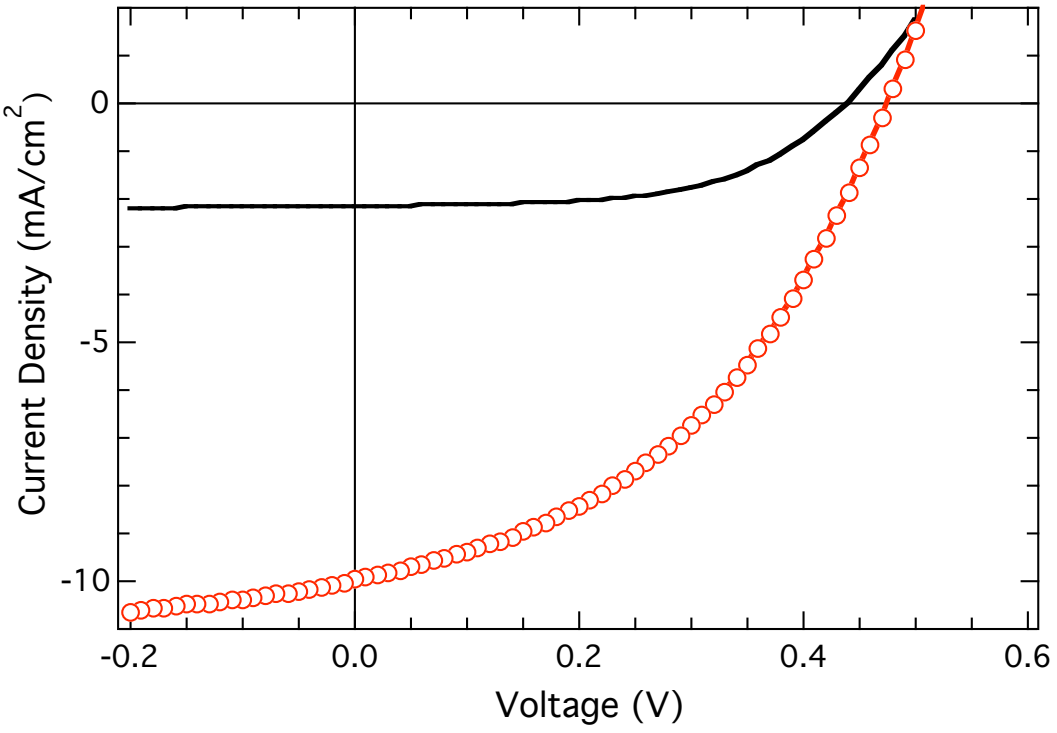

Figure 3.18 Current density versus voltage for typical ITO/ZnO/ZnO fibers/P3HT/Ag device (solid) and ITO/ZnO/ZnO fibers/P3HT:PCBM blend/Ag device (open circles).[122]

The EQE of both the ITO/ZnO/ZnO fibers/P3HT/Ag and ITO/ZnO/ZnO fibers/P3HT:PCBM blend/Ag devices are shown in Figure 3.19. When the blend is incorporated into the nanofibers, the EQE increases to a value greater than 57% at 515 nm. This is likely the result of enhanced exciton dissociation in the blend, where the distance between donor and acceptor materials is effectively reduced. The EQE response is red shifted compared to the device without PCBM, which is due to weak absorption of PCBM at 700 nm that increases the overlap with the solar spectrum. The EQE spectrum of the ITO/ZnO fiber/P3HT:PCBM blend/Ag device does not show a peak at 380 nm from hole transfer from ZnO. Both PCBM and ZnO demonstrate significant absorption below 400 nm and may contribute equally to the spectral response in this region.

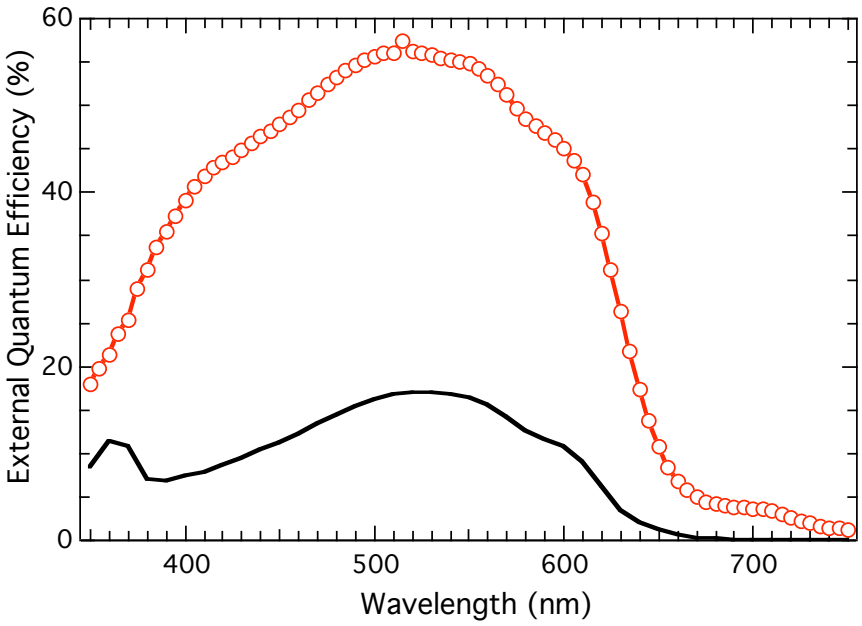

Figure 3.19 External quantum efficiency of ITO/ZnO/ZnO fibers/P3HT/Ag device (solid) and ITO/ZnO/ZnO fibers/P3HT:PCBM blend/Ag device (open circles).[122]

3.11 Inverted P3HT:PCBM Bulk Heterojunction Devices Based on ZnO

The introduction of PCBM as an additional acceptor species into the P3HT/ZnO nanofiber device results in a substantial increase in performance. However, similar performance can be observed when the P3HT:PCBM blend is spin coated onto a planar ZnO nucleation layer, indicating perhaps the negligible effect of the ZnO nanofibers on the performance of the previous device geometry. In fact, a device fabricated on the planar ZnO nucleation layer results in a 10% increase in the power conversion efficiency than one utilizing the ZnO nanofibers. The V_{OC}, FF and η increase to 529 mV, 53.6% and 2.28% respectively in the device without ZnO nanofibers as seen in Figure 3.20. The increased performance could be related to either improved P3HT:PCBM blend morphology or the elimination of the defects associated with the ZnO nanofibers that may serve as recombination sites. The J_{SC} increases from 8.05 to 9.9 mA cm^{-2} in the nanofiber device, which might be due to increased carrier collection from the ZnO nanofibers. These devices were tested under illumination without the UV filter, which degrades the performance of the device utilizing ZnO nanofiber. When the nanofiber device was measured using a UV filter, the J_{SC} was measured to be 8.0 mA cm^{-2} and V_{OC} was 518 mV. The UV excitation of the ZnO nanofiber device dramatically enhanced the J_{SC} at an illumination intensity of 100 mW cm^{-2}.

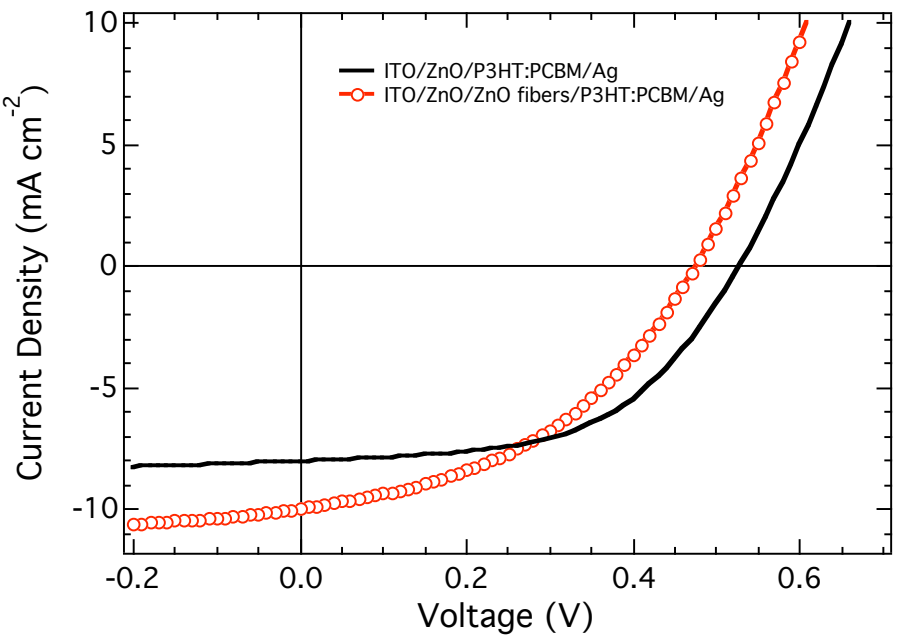

Figure 3.20 Current density versus voltage for typical ITO/ZnO/P3HT:PCBM blend/Ag device (solid) and ITO/ZnO/ZnO fibers/P3HT:PCBM blend/Ag device (open circles).

The EQE spectra were measured to evaluate the charge collection efficiency of the two device geometries as seen in Figure 3.21. It is clear from the photoaction spectra that the maximum charge collection efficiency is lower in the ZnO nanofiber device. This is not anticipated based on the J_{SC} being larger in the nanofiber device. However, the EQE spectra were measured using an intensity of 2 μW at 520 nm for the device area of 0.1 cm^2. This incident light intensity is more than three orders of magnitude smaller than the 100 mW cm^{-2} intensity light used for the J-V measurements above. Therefore, the EQE spectra may not accurately depict the device response at 100 mW cm^{-2} where the response may be much greater in the UV region. The charge collection efficiency is greater in the UV region at these low intensities, which may be the result of enhanced absorption by the ZnO nanofibers. The maximum EQE of 65% for the inverted P3HT/PCBM blend device is encouraging for the development of this device geometry.

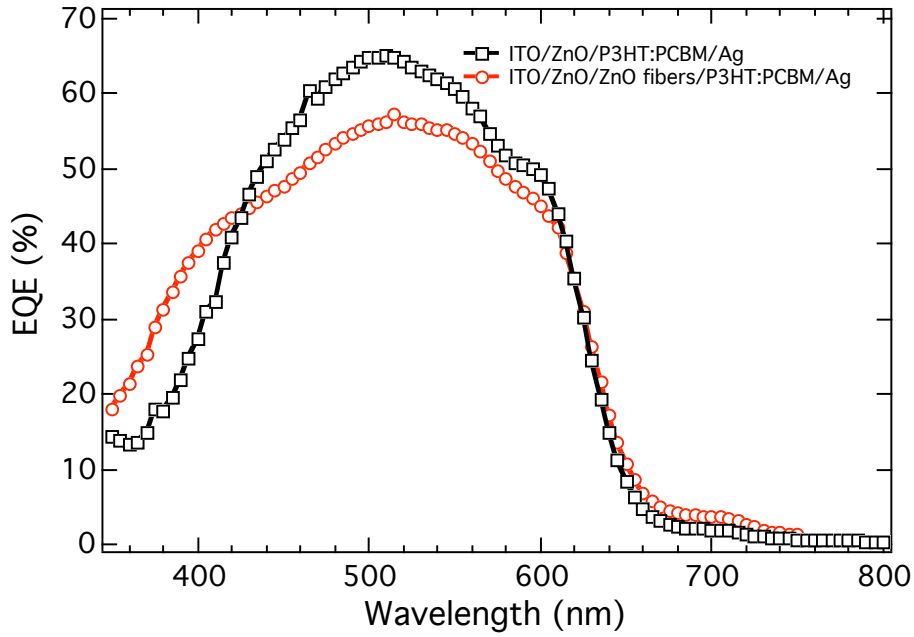

Figure 3.21 External quantum efficiency of ITO/ZnO/P3HT:PCBM blend/Ag device (open squares) and ITO/ZnO/ZnO fibers/P3HT:PCBM blend/Ag device (open circles).

The inverted P3HT:PCBM bulk heterojunction device may prove invaluable for the development of devices with increased stability. The inverted device geometry allows for the elimination of the low work function counter electrode required in traditional polymer/fullerene bulk heterojunction devices. Low work function metals have a large affinity for oxygen, resulting in the formation of an insulating oxide barrier. As a result, this may be a major degradation mechanism in these devices. Figure 3.22 compares the J-V curves under illumination for both the traditional ITO/PEDOT/P3HT:PCBM/Al device design fabricated in a glove box in an argon atmosphere and the inverted ITO/ZnO/P3HT:PCBM/Ag device design fabricated in air and developed here. These devices prepared in the same manner, one in the glove box and one in air, clearly demonstrate that comparable performance is possible with the

inverted device configuration. In fact, the performance of the inverted device is higher despite the device being processed in air, which historically has been strictly avoided in polymer/fullerene bulk heterojunction devices. While initial stability results have been inconclusive, the ability of inverted devices to be fabricated in air and still perform remarkably well is an indication that the configuration might lead to increased long-term device stability.

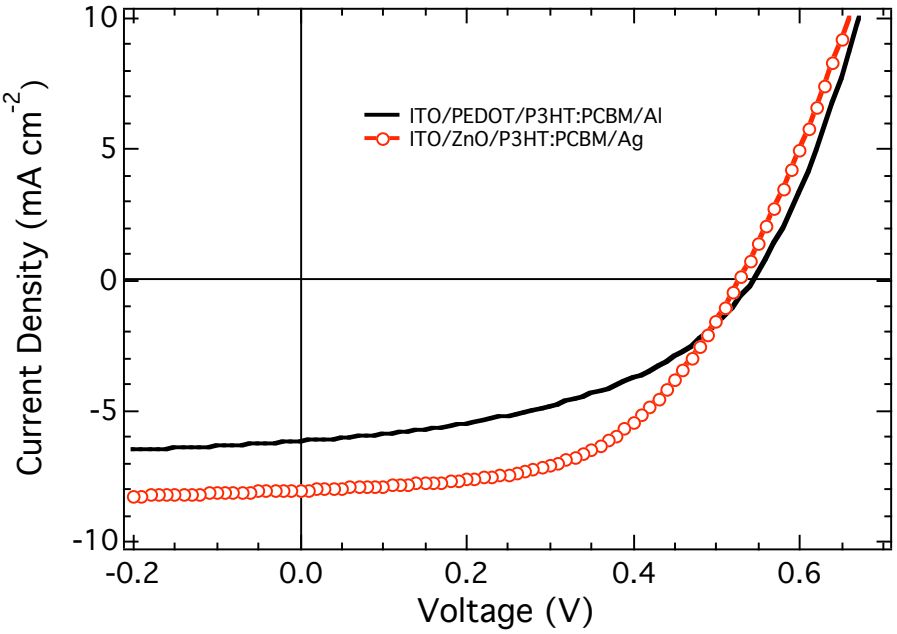

Figure 3.22 Current density versus voltage for typical ITO/PEDOT/P3HT:PCBM blend/Al device (solid) and ITO/ZnO/P3HT:PCBM blend/Ag device (open circles).

3.12 Effect of Surfactants and Interface Modifiers on Photovoltaic Performance

During the course of this work, a variety of surfactants and surface modifiers were employed in hopes of improving both the polymer intercalation into the ZnO nanofiber film and the photovoltage to the expected value. Surface treatments such as hexamethyldisilazane (HMDS), pentathiophene carboxylic acid, a carboxylic acid substituted C_{60}, ethane thiol, *p*-phenylene diamine, and pyridine all resulted in reduced performance. However, there were a few notable exceptions that may prove important for improved device performance. As described in Chapter 2, a phenyltrichlorosilane treatment of the ZnO nanofibers prior to spin coating of the P3HT film resulted in improved polymer intercalation. The device performance, however, was reduced substantially leading to insulating devices without measurable V_{OC}'s or J_{SC}'s. The device performance might be increased through careful selection of a different molecule that might improve the intercalation while having less of an effect on the electrical properties. This may be accomplished through substitution of the phenyl group or through a decreased concentration of the silane in the reaction solution, which would allow for reaction only on the tips of the ZnO fibers where the hydroxyl groups should be located.

Another surface treatment that improved the ZnO nanofiber device performance was methanol. The ZnO nanofibers substrates were spin coated with methanol at 4,000 RPM. Following this treatment, the polymer film was spin coated and the device was finished with the Ag counter electrode. Methanol treatment of the polymer/ZnO nanofiber devices showed reduced degradation of V_{OC} under UV illumination. The enhanced UV stability could be a result of surface state passivation by the methanol pretreatment. There was little overall improvement in the photovoltaic performance of the P3HT/ZnO nanofiber device. However, the methanol treatment had a much more substantial effect on the P3HT:PCBM blend/ZnO nanofiber device. While the same UV stability was observed, there was a corresponding increase in the V_{OC}. When compared to the P3HT:PCBM/ZnO nanofiber device without methanol treatment, the V_{OC} increased

from 475 mV to greater than 560 mV under illumination without the UV filter as seen in Figure 3.23. There was a decrease in the J_{SC} and little change in the overall conversion efficiency. Unlike the methanol treated device, the untreated device was not stable under UV illumination with its performance degrading rapidly with each consecutive exposure.

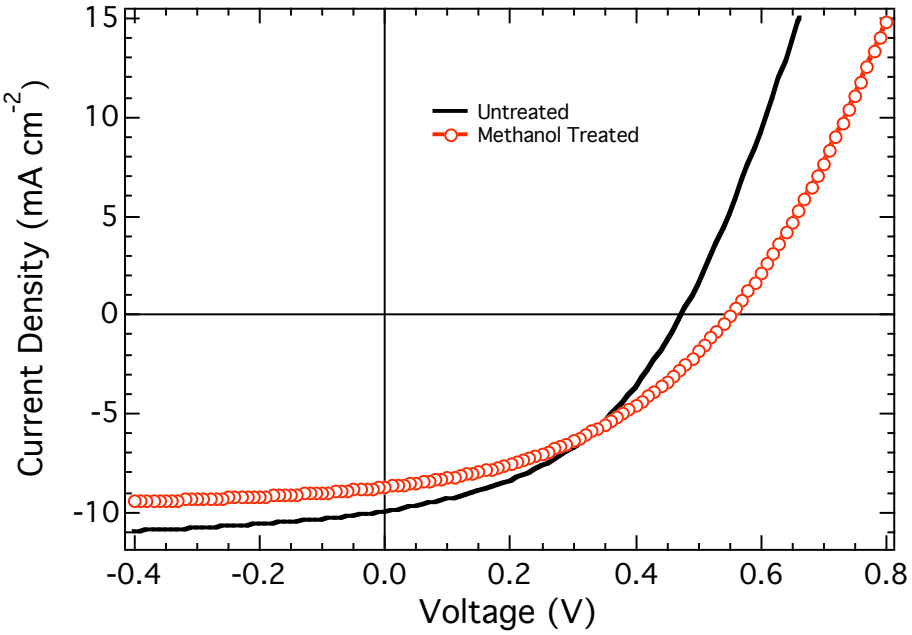

Figure 3.23 Current density versus voltage for typical ITO/ZnO/ZnO fibers/P3HT:PCBM blend/Ag device (solid) and ITO/ZnO/ZnO fibers/Methanol/P3HT:PCBM blend/Ag device (open circles).

In P3HT/ZnO nanofiber devices, the treatment of the ZnO nanofiber surface with ethylene glycol increased the J_{SC} by 10% without a high temperature anneal for polymer intercalation as seen in Figure 3.24. A 10% solution of ethylene glycol dissolved in methanol was spin coated at 4,000 RPM onto the ZnO nanofiber films prior to the

deposition of P3HT. Devices spin coated with pure ethylene glycol resulted in poor film quality and reduced performance due to its high viscosity. The performance of the 10% ethylene glycol in methanol was compared to a device pretreated with methanol only to observe the effects of the ethylene glycol pretreatment as seen in Figure 3.24. The increased J_{SC} could be the result of either more complete intercalation or the formation of a surface dipole at the interface between the P3HT and ZnO. The latter explanation might be better suited to the J-V data that indicate a corresponding decrease in the V_{OC} and concomitant increased J_{SC}.[14] In addition, the UV stability observed with the methanol pretreatment was also present in the ethylene glycol treated device, indicating a change in the surface states or the interfacial chemistry between the polymer and ZnO.

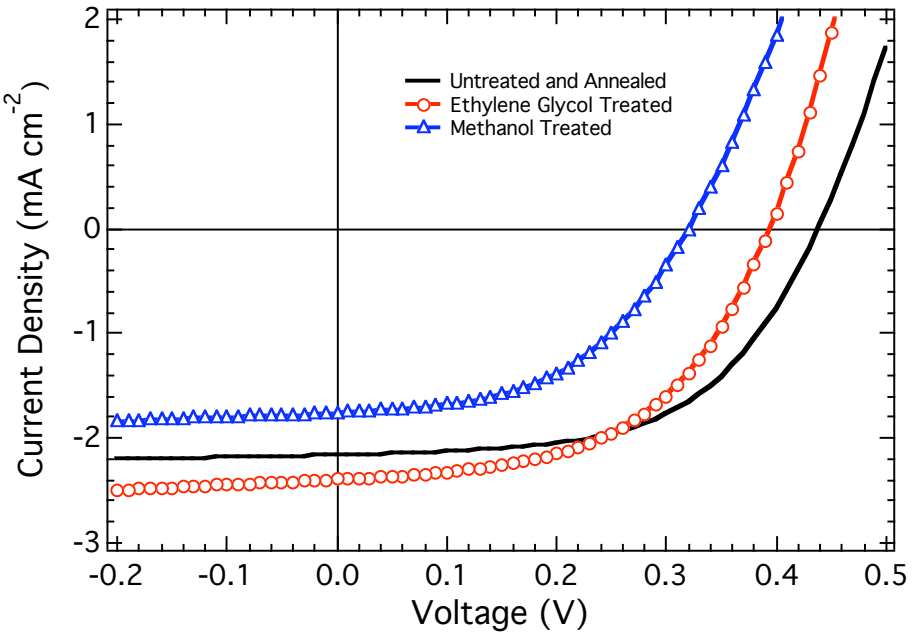

Figure 3.24 Current density versus voltage for typical ITO/ZnO/ZnO fibers/P3HT Annealed/Ag device (solid), ITO/ZnO/ZnO fibers/Ethylene Glycol/P3HT/Ag device (open circles), and ITO/ZnO/ZnO fibers/Methanol/P3HT/Ag device (open triangles).

The EQE was measured to observe the increased current collection efficiency of the ethylene glycol pretreated device as seen in Figure 3.25. The maximum EQE increased by 20% to a value of 21.8% compared to the untreated device, perhaps indicating better intercalation of the polymer into the ZnO nanofiber film. The inset shows the normalized spectral response for both devices and indicates similar behavior devices. This suggests there is little change in polymer chain order, indicating the increase in J_{SC} may result from enhanced intercalation of the polymer.

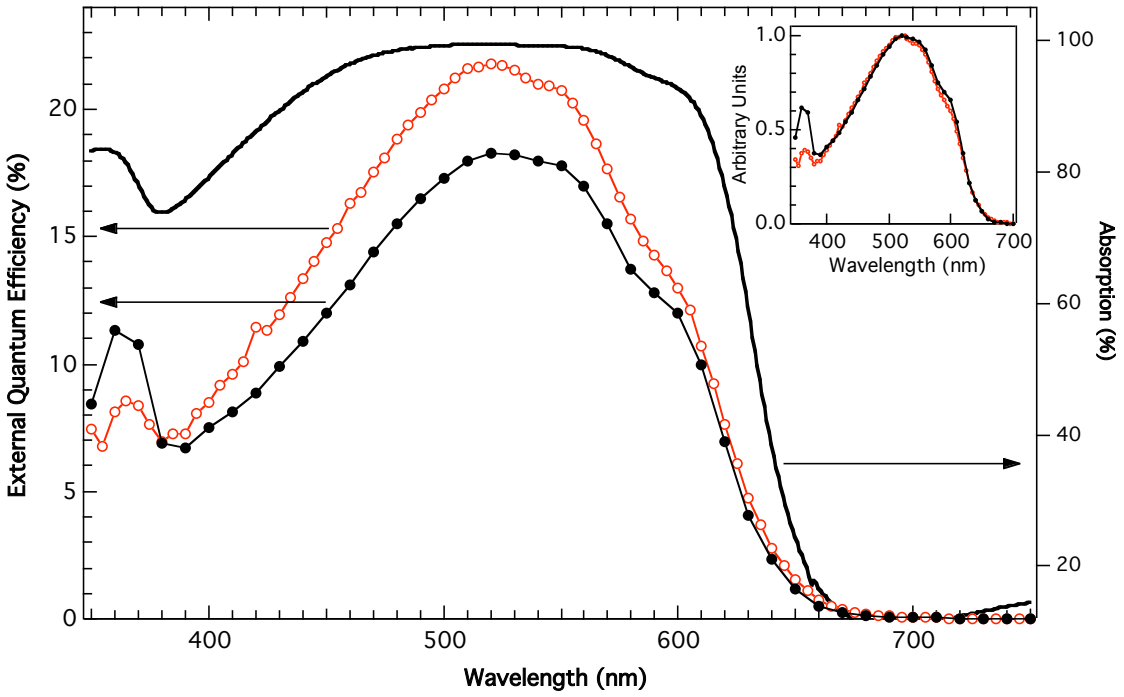

Figure 3.25 External quantum efficiency of ITO/ZnO/ZnO fibers/P3HT/Ag device (solid circles) and ITO/ZnO/ZnO fibers/Ethylene Glycol/P3HT/Ag device (open circles). The absorption spectrum (solid line) of the untreated device is included for reference. Inset shows normalized spectra.

Another successful pretreatment was nonionic polyethylene glycol (PEG). Improved performance in OLEDs has been observed using PEG either blended into the electroluminescent layer (EL) or at the interface between the EL and the cathode.[123, 124] Polyoxyetholene(12) tridecyl ether ($P_{12}TE$) was dissolved in methanol at a concentration of 5 g/l. The $P_{12}TE$ solution was spin coated at 4,000 RPM onto the ZnO fibers. The $P_{12}TE$ device was compared to methanol treated devices. Devices pretreated with $P_{12}TE$ demonstrated higher V_{OC} values. The increase in V_{OC} in the ZnO nanofiber device was great enough to offset the decreased J_{SC} and lead to a power conversion efficiency equal to that of the untreated annealed device as seen in Figure 3.26. This could be attributed to either the addition of an insulating layer between the donor and acceptor pair, or could be the result of a surface dipole to increase the V_{OC} in the device.

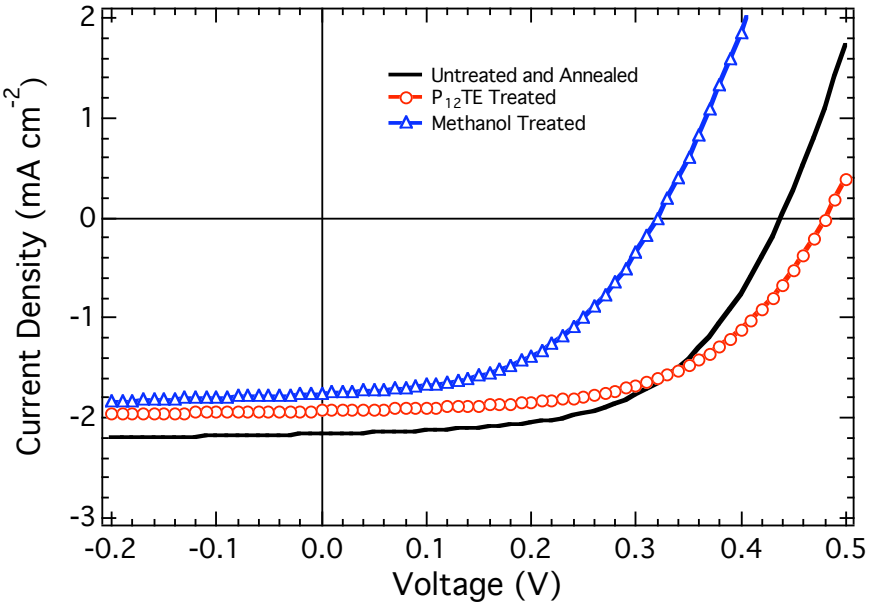

Figure 3.26 Current density versus voltage for typical ITO/ZnO/ZnO fibers/P3HT Annealed/Ag device (solid), ITO/ZnO/ZnO fibers/$P_{12}TE$/P3HT/Ag device (open circles), and ITO/ZnO/ZnO fibers/Methanol/P3HT/Ag device (open triangles).

The effect of the $P_{12}TE$ pretreatment on P3HT/ZnO bilayer devices was much more significant. The V_{OC} increased dramatically from 401 mV to 683 mV for a bilayer device treated with $P_{12}TE$ as seen in Figure 3.27. However, the J_{SC} is reduced from 0.78 mA cm^{-2} to 0.36 mA cm^{-2}.

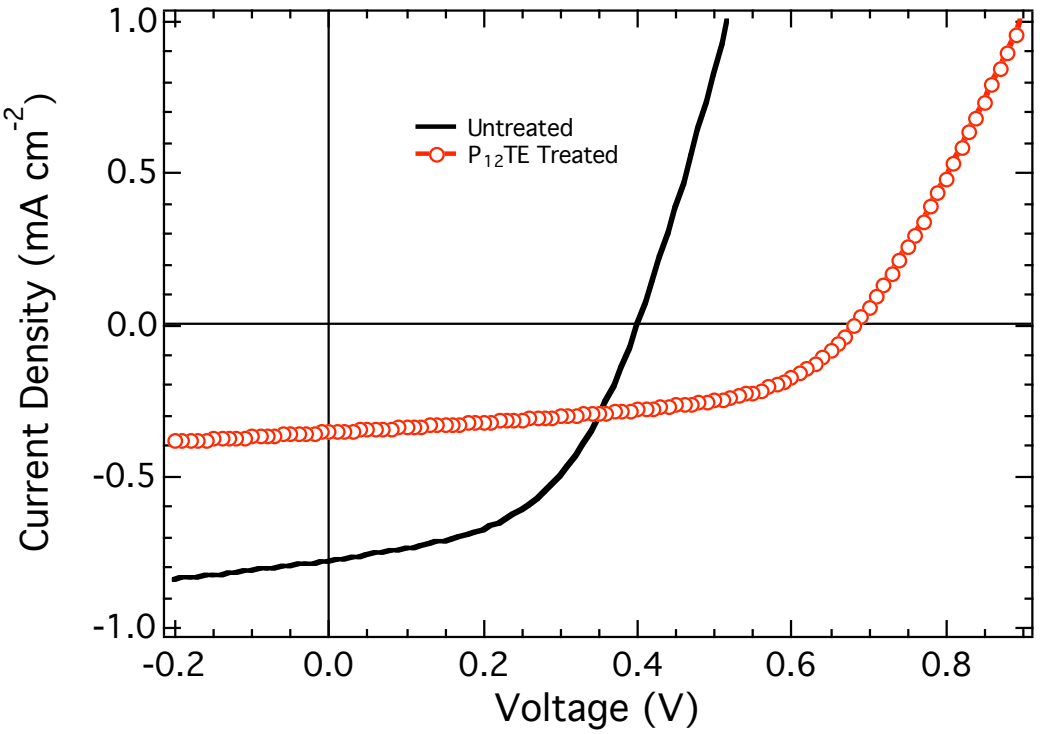

Figure 3.26 Current density versus voltage for typical ITO/ZnO/P3HT/Ag device (solid), and ITO/ZnO/$P_{12}TE$/P3HT/Ag device (open circles).

To observe the effect of $P_{12}TE$ thickness on device performance, devices using lower concentration $P_{12}TE$ solutions were fabricated. In addition, to see if the effect was selective to the polymer itself, bilayer MDMO-PPV/ZnO bilayer devices were fabricated. Increasing concentration of $P_{12}TE$ from the untreated device to pretreatment with a 0.5

g/l, 2.5 g/l and 5 g/l leads to a systematic increase in V_{OC}, with a systematic reduction in the J_{SC} with $P_{12}TE$ coverage as seen in Figure 3.27. Again, this could be due to increased thickness as an insulator with increased concentration, or could be due to the increase in coverage with increased concentration. Further investigation is needed to determine the mechanism for increased V_{OC}. Additionally, the effect is not unique to the P3HT/ZnO system, as demonstrated in the PPV/ZnO device below.

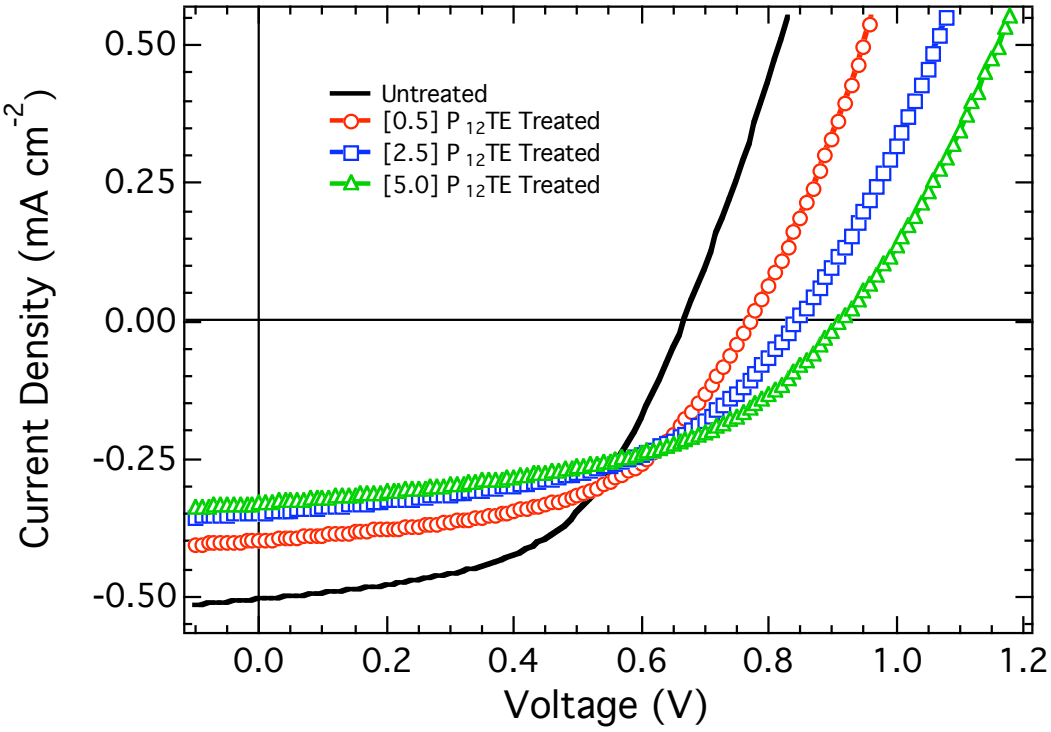

Figure 3.27 Current density versus voltage for typical ITO/ZnO/PPV/Ag device (solid), ITO/ZnO/[0.5] $P_{12}TE$/PPV/Ag device (open circles), ITO/ZnO/[2.5] $P_{12}TE$/PPV/Ag device (open squares), and ITO/ZnO/[5.0] $P_{12}TE$/PPV/Ag device (open triangles).

3.13 Summary

Hybrid photovoltaic devices made with a P3HT/ZnO nanofiber composite structures have yielded an efficiency of 0.53% under AM1.5 illumination, significantly greater than that of similar bilayer devices. An increased efficiency of 0.61% was observed at higher light intensities, indicating the possible advantage in using high mobility electron transport pathways. While these efficiencies are still lower than other hybrid organic photovoltaic devices, there are clear limitations in the current device architecture and several paths are being pursued that might lead to higher efficiencies. The inverted device architecture allows for device fabrication and storage in air, which is prohibited in the majority of organic photovoltaic devices.

CHAPTER 4

ENHANCED OPEN CIRCIUT VOLTAGE IN POLYMER/OXIDE SOLAR CELLS THROUGH BAND OFFSET ENGINEERING

Abstract

Current polymer photovoltaic devices are limited in efficiency by both low photocurrents and photovoltages. The loss in photovoltage originates from large band offsets between the donor and acceptor species, leading to a loss in energy for the extracted charges by a factor of approximately 2-3 compared to the energy of the incoming photon. This chapter reports on the substitution of magnesium into the zinc oxide acceptor resulting in a systematic increase in the open circuit voltage of planar devices using poly(3-hexylthiophene). Substitution of magnesium to yield $Zn_{1-x}Mg_xO$ reduces the band offset between donor and acceptor, leading to open circuit voltages in excess of 900 mV and concomitant increases in overall device efficiency. This work provides an important new tool for understanding and optimizing the photovoltage in hybrid photovoltaics.

4.1 Introduction

In previous chapters we have discussed the fabrication of bulk heterojunction polymer devices for low cost manufacturing. As a review, photovoltaic researchers are pursuing a variety of approaches directed toward making photovoltaics cost-effective as a large-scale, renewable energy resource. Solution-based approaches in particular are

intrinsically low-cost due to the low temperatures and atmospheric processing conditions used. Ultimately the goal of these approaches is to enable roll-to-roll fabrication on flexible substrates resulting in low balance-of-system costs for the entire photovoltaic module. Polymer-based solar cells have the potential to be a viable pathway to this vision.[2, 125, 126] One of the most successful approaches to date has been a bulk heterojunction device that is based on blending a conjugated polymer with a fullerene derivative. Devices have been successfully fabricated from a number of different polymers. Results show that the short circuit current density (J_{SC}) is dependent on the exact composition and morphology of the phase separated system. Enhancements in photocurrents in such devices have been demonstrated upon improvements of the blend morphology in poly(phenylyene vinylene)-based devices,[44] as well as due to improved molecular ordering, increased polymer ratio in the blend and a modest reduction in optical band gap for poly(3-hexylthiophene) (P3HT) based devices.[41] Further reductions in the series resistance have resulted in documented power conversion efficiencies approaching 5% for bulk heterojunction devices.[42, 127] These developments in devices using P3HT and [6,6]-phenyl-C_{61}-butyric acid methyl ester (PCBM) have helped to optimize both the J_{SC} and the fill factor (FF) with a corresponding increase in the conversion efficiency (η). Few efforts, however, have significantly improved the open circuit voltage (V_{OC}) in polymer photovoltaic devices. Typical values for the V_{OC} in P3HT/PCBM devices are ~ 0.60 V, whereas the lowest energy photons absorbed by P3HT are approximately 1.9 eV. A conventional diode model yields a $V_{OC}^{MAX} = 1.5V$ for a band gap of 1.9 eV. Thus 60% of the energy of an incoming photon is immediately lost to thermalization and can not contribute to the power conversion efficiency of the device.

The V_{OC} in an "excitonic" solar cell is fundamentally determined by the effective electronic band gap of the donor-acceptor system.[128] This is given by the difference between the thermalized potential energies of the electron in the conduction band or lowest unoccupied molecular orbital (LUMO) in the acceptor and the hole in the valence band or highest occupied molecular orbital (HOMO) of the donor as seen in Figure 4.1.

The actual V_{OC} in the device will be less than this value due to the exciton binding energy and carrier recombination either in the bulk or at the electrodes.[6, 32] Additionally, the V_{OC} can be reduced by chemical potential pinning to poorly optimized electrodes.[129] Variation of the work function of either the positive or negative electrode has been demonstrated to influence the V_{OC} in polymer PV devices.[32, 130, 131] Also, interface dipoles at the electrode can play an important role in determining the V_{OC}.[113] That the V_{OC} is directly controlled by the effective electronic band gap of the donor-acceptor system has been demonstrated as well as through alteration of the fullerene component to change its reduction potential and therefore the band offset with respect to the electron-donating polymer.[32] In this case, the V_{OC} decreased as a result of an increased band offset. Similarly, changes in V_{OC} have been observed by varying the oxidation potential of the electron-donating polymer.[132] When the oxidation potential was increased in a range of polythiophenes blended with PCBM, a corresponding increase in the V_{OC} was observed. These results provide a good indication that the HOMO level in the donor molecule in part determines the V_{OC}. Similar results have been observed for poly(2-methoxy-5-(3',7'-dimethyloctyloxy)-1,4-phenylenevinylene) (MDMO-PPV) blended with fullerene acceptors with reduced electron affinities indicating that the other major component in determining the V_{OC} is the LUMO level of the electron acceptor.[32] Solvation effects have also demonstrated a reduction of the J_{SC} and an increase in the V_{OC} through changes in morphology in a bulk heterojunction device.[133] Generally this is a relatively small effect, where V_{OC} increases with the level of molecular disorder in the film, which is likely due to a shift of the HOMO level of the donor molecule away from vacuum. This can often be seen with an accompanying blue shift in the absorption spectra.

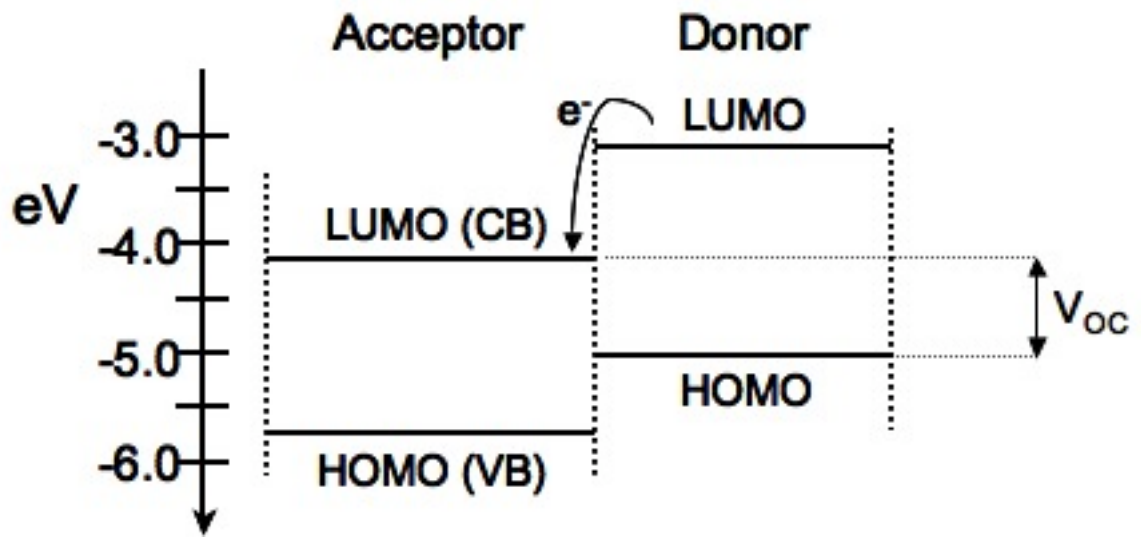

Figure 4.1 Band diagram of donor-acceptor pair with V_{OC} as determined by band offset.

While changes in V_{OC} have been observed through modifying either the donor or acceptor molecules, the attained V_{OC}'s lie well below the theoretically possible values. Reduction of the donor-acceptor band offset, while maintaining sufficient driving force necessary for efficient electron transfer and slow recombination kinetics, should minimize the energy loss and allow for higher V_{OC}'s. Thus higher device efficiencies can be obtained through the proper design and selection of donor-acceptor materials.

Hybrid devices based on polymer/zinc oxide (ZnO) nanoparticle blends have successfully demonstrated attractive efficiencies comparable to early bulk heterojunction devices.[35, 66] As discussed in Chapters 2 and 3, other hybrid devices based on polymer/ZnO nanofibers and polymer/mesoporous titanium dioxide (TiO_2) composites have been developed though they are presently limited in efficiency by low J_{SC} values.[73, 75, 76, 120, 122] If the conduction band is moved closer to vacuum then it would be expected that V_{OC} would increase as seen in Figure 4.2.

In this chapter a model system for an inorganic electron acceptor has been investigated in which substitutional doping can easily modify the band gap and electron mobility. Significant increases in the V_{OC} were observed when the gap increased reflecting the observed change in the conduction band position.

4.2 The Substitutional Doping of ZnO

It has been demonstrated that the band gap of ZnO can be altered by substitution of divalent cations for the Zn. Mg substitution has been shown in pulsed laser deposition (PLD) experiments to increase the band gap,[134] whereas Cd has been shown to reduce it.[135] These appear to be true solid solution systems showing very small structural changes to the ZnO wurtzite structure. Additionally, the samples can be doped in the conventional fashion with Al, Ga or In giving rise to the potential for independently controlling the gap and doping level in the metal oxide.[136] Thin films of $Zn_{1-x}Mg_xO$ have been fabricated through a sol-gel deposition method with Mg content up to an x value of 0.36. An increase in the band gap from 3.4 to 3.93 eV was observed with no phase separation through annealing up to 700 °C.[137] Recent studies have shown that much of that increase should be in the conduction band, which agrees with the common anion rule.[138] For the purposes of this study, such a high temperature anneal would dramatically reduce the conductivity of the underlying indium tin oxide (ITO) electrode. Therefore, the film synthesis was adapted to be compatible with our standard bilayer device fabrication techniques. The V_{OC} could be increased by changing the conduction band level in such a film of $Zn_{1-x}Mg_xO$ as seen in Figure 4.2.

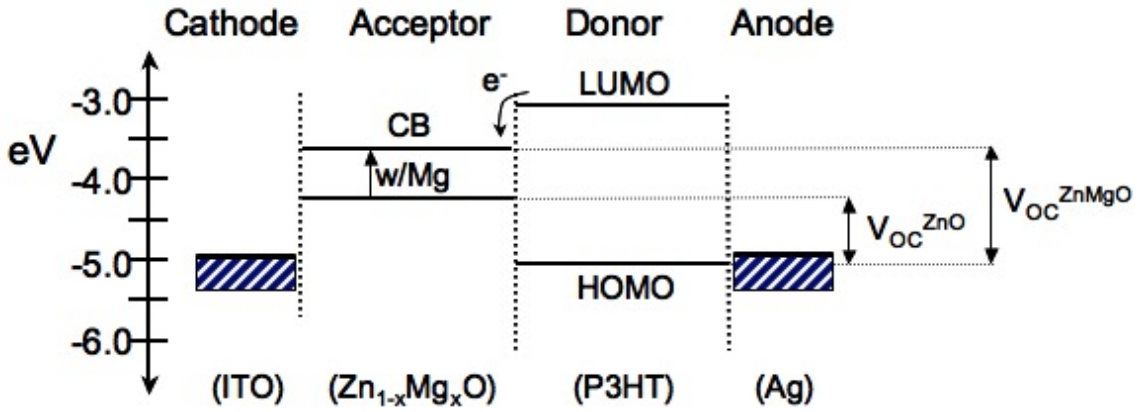

Figure 4.2 Band diagram of ITO/$Zn_{1-x}Mg_xO$/P3HT/Ag hybrid polymer/metal oxide device.

4.2 The Synthesis and Characterization of $Zn_{1-x}Mg_xO$ Films from Solution

The $Zn_{1-x}Mg_xO$ thin films were fabricated by spin coating from a solution of zinc and magnesium acetates at the proper molar ratio, similar to methods used for nucleation layer films made in previous studies. $Zn_{1-x}Mg_x$Acetate solutions were prepared in the proper molar ratio from zinc acetate 2·hydrate and magnesium acetate 4·hydrate ratio as indicated dissolved in a mixture of ethanol amine in 2-methoxyethanol. The ratio of ethanol amine to total metal acetate was 1.0 and the total concentration of metal acetate was 0.75 M. After thermal annealing the zinc/magnesium acetate film for 5 minutes at 300 ˚C in air, the $Zn_{1-x}Mg_xO$ film was rinsed with deionized water and ethanol. The $Zn_{1-x}Mg_xO$ film thickness was measured as 50 – 80 nm. The film thicknesses were measured on a Dektak 3 profilometer. The alloy composition of the film deposited on glass was confirmed by inductively coupled plasma analysis (ICP) with very good agreement with the calculated composition based on the metal content in the original solution. ICP measurements were made using a Varian ICP 100. The $Zn_{1-x}Mg_xO$ films deposited on

glass were investigated with x-ray diffraction (XRD) to determine the phase and also the maximum Mg content before phase separation occurred. XRD measurements shown in Figure 4.3, were performed on a Bruker D8 with a two-dimensional large area detector and an x-y sample positioning stage. Each sample was measured for two hours to increase the signal to noise ratio. With increasing Mg content the films remain in the wurzite-type ZnO phase without any impurity phase until x = 0.45 when there is phase separation to include the cubic MgO phase. The maximum Mg content is significantly larger than the thermodynamic limit of x = 0.04.[84] Incorporation of Mg into the ZnO phase does decrease the crystallinity of the film, with the (100), (002), and (101) peaks becoming weaker and broadening with increasing Mg at the anneal temperatures employed here. There is not a dramatic shift in peak position, indicating that Mg is incorporated without significant strain on the lattice, which would be expected based on ionic radii of Zn^{2+} and Mg^{2+} (0.60 and 0.57 Å, respectively). The XRD study indicates that for PV devices, phase separation limits usable Mg contents to less than x = 0.45. As such, the x = 0.45 Mg film is not employed in other measurements mentioned below.

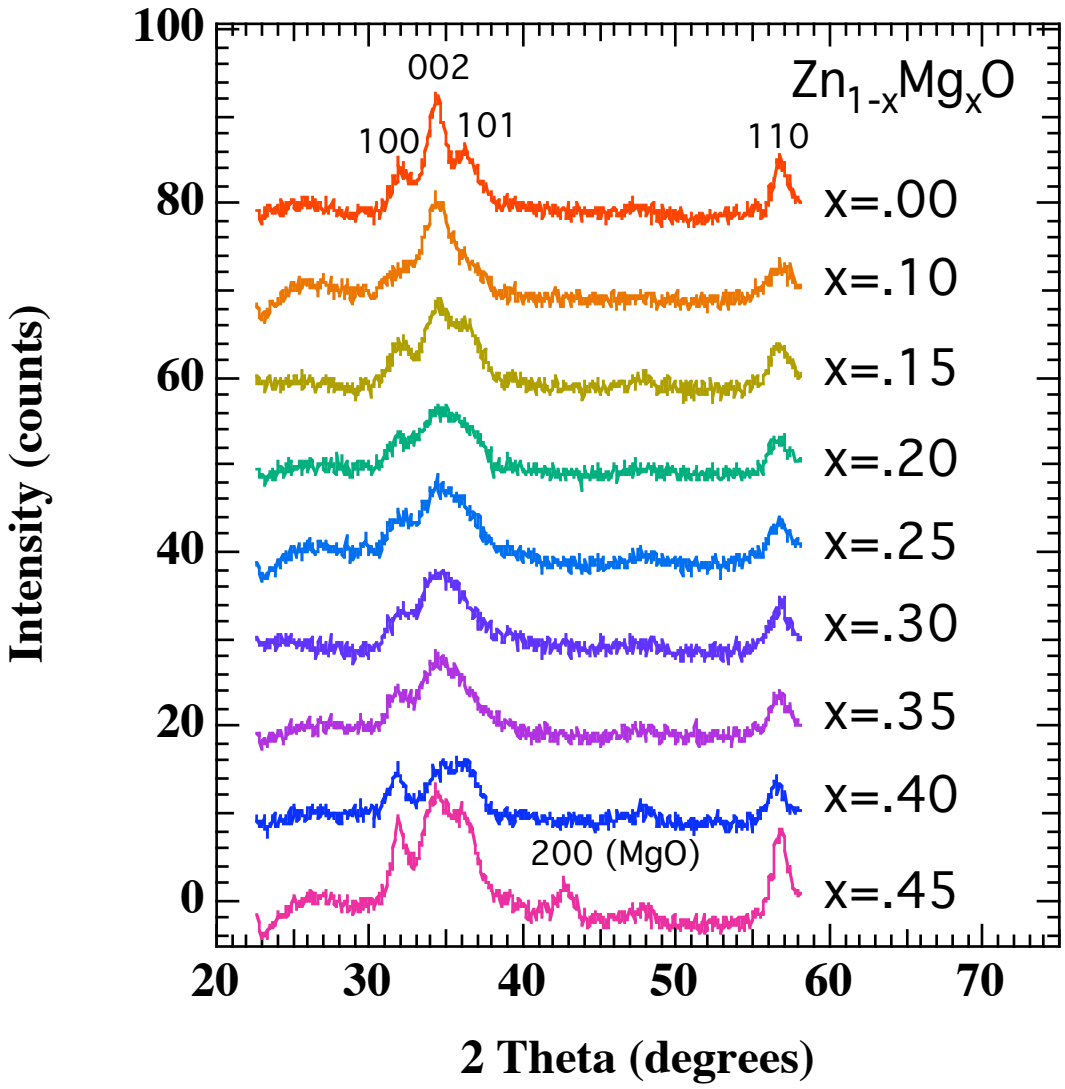

Figure 4.3 XRD θ-2θ scans for $Zn_{1-x}Mg_xO$ films ($0 < x < 0.45$) deposited on glass.

Spectra of $Zn_{1-x}Mg_xO$ films ($0<x<0.40$) deposited on quartz substrates were measured using UV-Vis absorption on a Hewlett Packard 8453 UV-vis spectrophotometer. It is assumed that the $Zn_{1-x}Mg_xO$ material is a direct band gap semiconductor based on its efficient PL, and that ZnO itself is a direct band gap

semiconductor being developed for UV-LEDs.[139, 140] All of the samples are transparent in the visible region from 400-800 nm, with an absorption edge in the UV region. Optical band gaps were calculated using the Urbach model by fitting the absorption coefficient α to the equation $\alpha = A^*(h\nu - E_g)^{1/2}$, where A* is a constant related to the refractive index and the electron/hole effective masses. A plot of α^2 vs. $h\nu$ (photon energy) was used to estimate the band gap of the $Zn_{1-x}Mg_xO$ films. The band gap increases linearly from ~3.2 to 4.0 eV with Mg composition up to x = 0.40, as seen in Figure 4.4, indicating that Mg is effectively incorporated into the ZnO lattice.

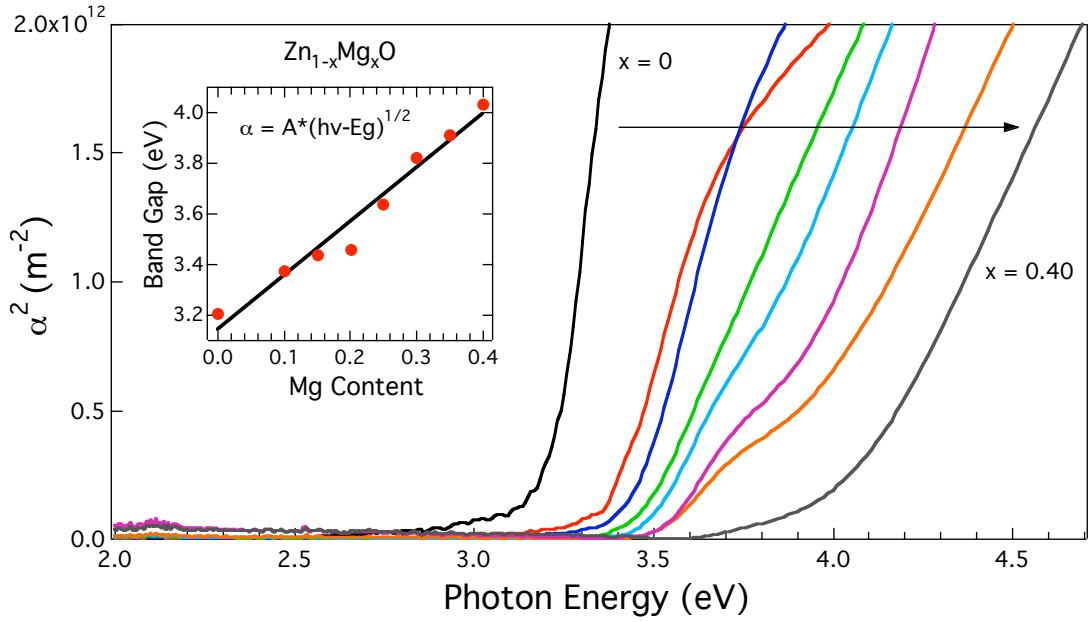

Figure 4.4 Absorption coefficient (α^2) vs. photon energy ($h\nu$) for $Zn_{1-x}Mg_xO$ films ($0 < x < 0.40$) deposited on quartz. Inset shows increase in band gap with Mg composition.

The work function, or the Fermi energy, of the $Zn_{1-x}Mg_xO$ films deposited on ITO was estimated by Kelvin probe contact potential measurements of the surface potential difference with respect to a stainless steel reference. The work function measurements were performed using a McAllister Technical Services KP6500 Kelvin probe under flowing N_2 or air. Since ZnO grown as described here is typically an n-type semiconductor, it is assumed that the Fermi energy will be close to the conduction band energy. Therefore the change in work function with composition gives an estimate for the change in the conduction band position with Mg content. The Kelvin probe data suggest that the work function is reduced with increasing Mg composition, as seen in Figure 4.5, which indicates a shift in the conduction band closer to vacuum. It is interesting to note that when measured in air instead of N_2, the work function increases with Mg content, perhaps indicating more absorption of water or hydroxyl ions on the surface of films with higher Mg content. As a result the prepared devices were quickly removed from the hotplate and cooled under flowing nitrogen gas prior to spin coating of the polymer in air.

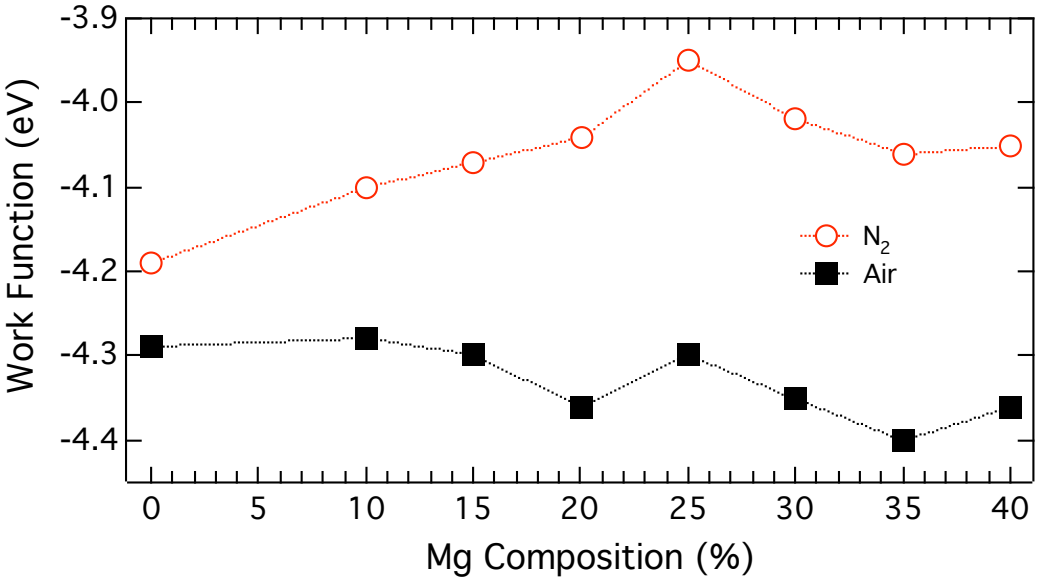

Figure 4.5 Work function of for $Zn_{1-x}Mg_xO$ films ($0 < x < 0.40$) deposited on ITO. Work function was measured in nitrogen (open circles) and in air (solid squares) by Kelvin probe with respect to a calibrated stainless steel reference.

4.3 The Increase of the V_{OC} with Mg Content in Polymer/$Zn_{1-x}Mg_xO$ Bilayer Devices

To observe the effects of varied band offsets on the V_{OC}, hybrid P3HT/$Zn_{1-x}Mg_xO$ bilayer devices were prepared. Bilayer devices were chosen here to demonstrate the concept, though nanostructured $Zn_{1-x}Mg_xO$ materials will ultimately be required for higher efficiency devices. Devices were fabricated on $Zn_{1-x}Mg_xO$ films deposited on ITO coated glass. After thermal annealing the $Zn_{1-x}Mg_xO$ films were dried in air for 20 minutes at 200 ˚C. The films were removed from the hotplate and cooled in flowing N_2 gas, and a 200 nm layer of P3HT was spin-coated from a 30 mg/ml chlorobenzene solution on top of this structure. A 90 nm silver top contact was thermally evaporated through a shadow mask to form the positive back electrode with active areas for each device of 0.1 cm^2. This was followed by another thermal anneal at 120 ˚C for ten

minutes in air prior to measurement. Devices were subsequently stored in air in the dark. All photovoltaic characterizations were performed in air without the use of UV filters to observe the affects of the increased acceptor material band gap on the UV stability of the device. The devices were characterized by current density-voltage (J-V) measurements. Measurements were made under simulated AM1.5 illumination (100 mW cm^{-2}) corrected for spectral mismatch, by comparison with a standard device measured by the Measurements and Characterization group at the National Renewable Energy Laboratory (NREL). The J-V curves for the P3HT/ $Zn_{1-x}Mg_xO$ bilayer devices are shown in Figure 4.6. The substitution of Mg into the ZnO acceptor results in a systematic increase in the V_{OC} from 500 mV for $Zn_{1.0}Mg_{0.0}O$ to greater than 900 mV for $Zn_{0.65}Mg_{0.35}O$ as seen in Figure 4.7. When the Mg composition increased to x = 0.40, the V_{OC} drops dramatically. Similarly, the JSC and η increase with increasing Mg content as well, though they begin to fall off above x = 0.25 as seen in Figure 4.7. These observations might indicate that the band offset is not great enough to efficiently separate charges at that Mg substitution level, or that the series resistance in the device is too high to allow efficient transport of the charges out of the device.

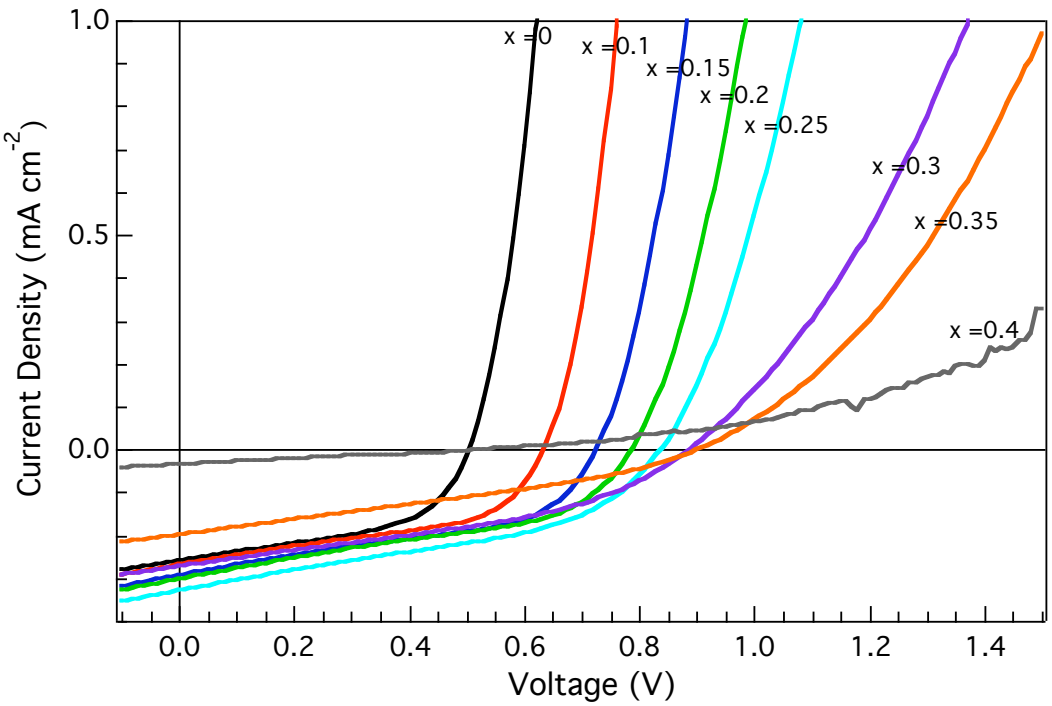

Figure 4.6 Current density vs. voltage P3HT/ $Zn_{1-x}Mg_xO$ devices ($0 < x < 0.40$).

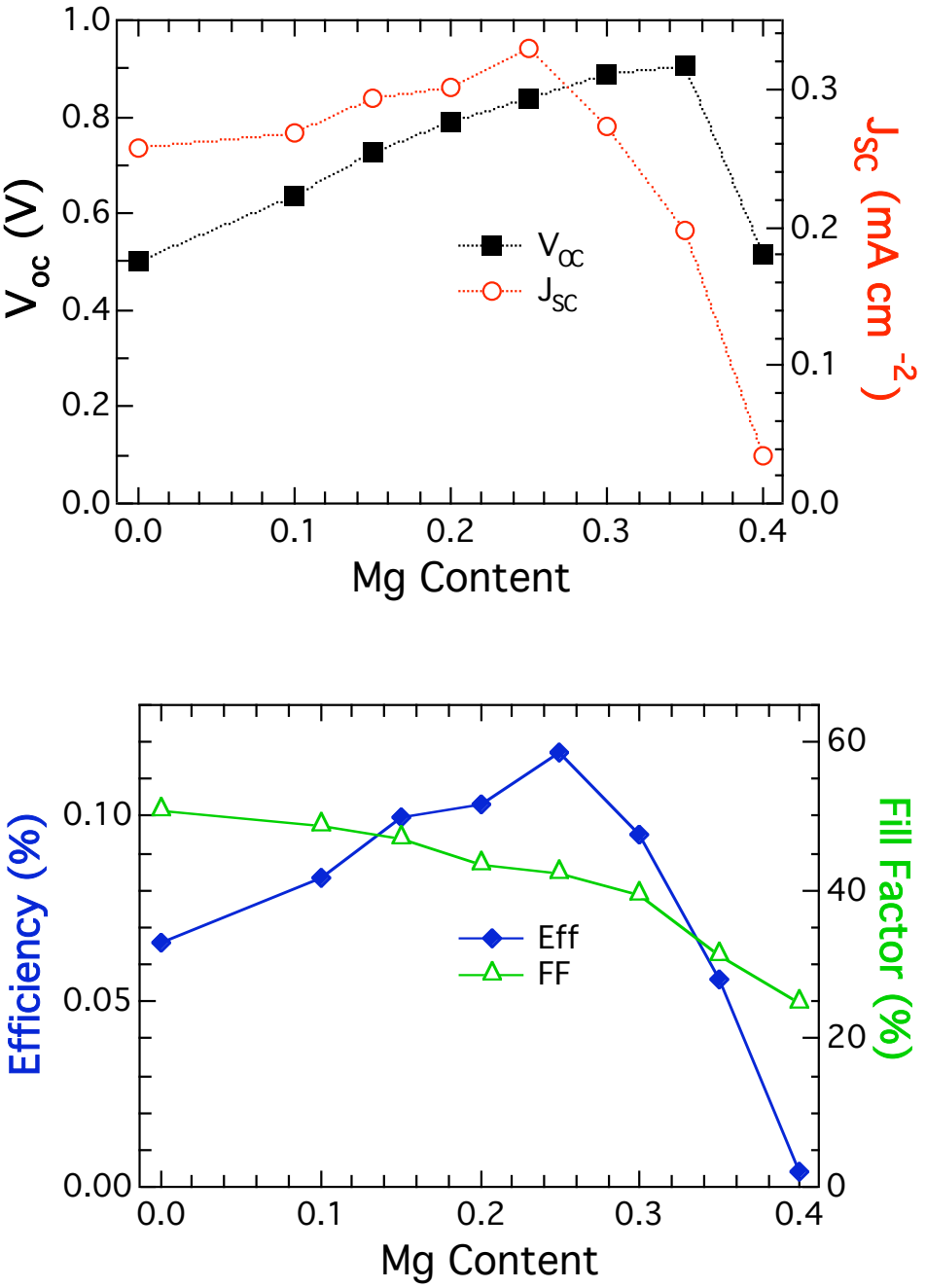

Figure 4.7 Photovoltaic performance of synthesized P3HT/ $Zn_{1-x}Mg_xO$ devices ($0 < x < 0.40$). Top, V_{OC} (solid squares) and J_{SC} (open circles) vs Mg content. Bottom, Efficiency (solid diamonds) and FF (open triangles) vs. Mg content.

The V_{OC} is observed to increase linearly with band gap of $Zn_{1-x}Mg_xO$ with a slope of 1.0 up to $Zn_{0.80}Mg_{0.20}O$, above which the slope decreases to 0.25 as seen in Figure 4.8. As the conduction band level moves closer to vacuum there is a corresponding increase in the V_{OC}, indicating that the increased band gap results in a shift of the conduction band of the $Zn_{1-x}Mg_xO$ acceptor.

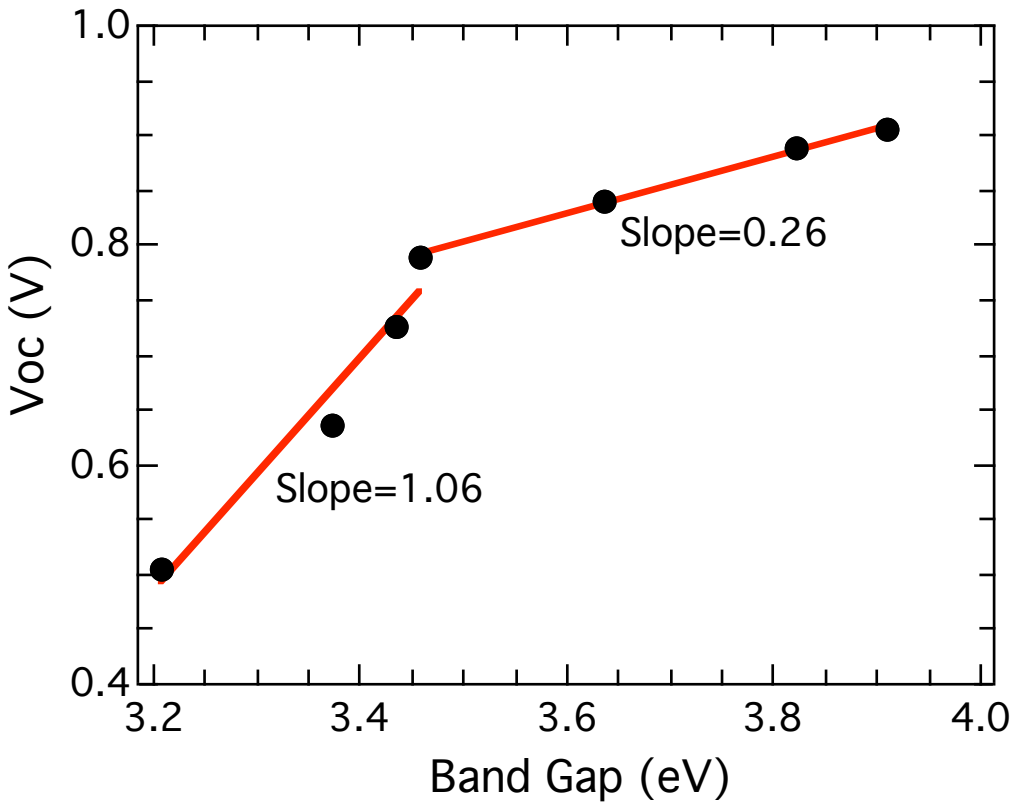

Figure 4.8 V_{OC} vs. $Zn_{1-x}Mg_xO$ band gap.

The series resistance in these devices increases exponentially from 4.2 to 72 Ω cm^2 with increasing Mg content as see in the inset in Figure 4.9. This agrees with preliminary time resolved microwave conductivity (TRMC) measurements,[21] shown in Figure 4.9, which indicate that increasing Mg content results in an exponential decrease of the mobility from almost 3 x 10^{-2} to less than 4 x 10^{-4} cm^2 V^{-1} s^{-1}.[141] The carrier lifetime in the $Zn_{1-x}Mg_xO$ films remains constant throughout the series. These observations suggest that the Mg atoms do not act as trap defects but rather as scattering centers that reduce the carrier mobility. The increase in the series resistance should lead to a decrease in the performance of the device. However despite the increase in series resistance, the J_{SC} actually increases by 25% up to $Zn_{0.75}Mg_{0.25}O$. This could be explained by several possible mechanisms, including an increase in surface roughness leading to increased interfacial area between polymer and oxide which will be discussed later, a change in the intrinsic carrier concentration in the $Zn_{1-x}Mg_xO$, an alteration of the chemistry of the interface leading to different exciton dissociation or carrier recombination rate, or a balancing of the electron and hole mobilities (time of flight mobility measurements for P3HT indicate a mobility of 4 x 10^{-4} cm^2 V^{-1} s^{-1})[142] that reduces recombination in the device.[42]

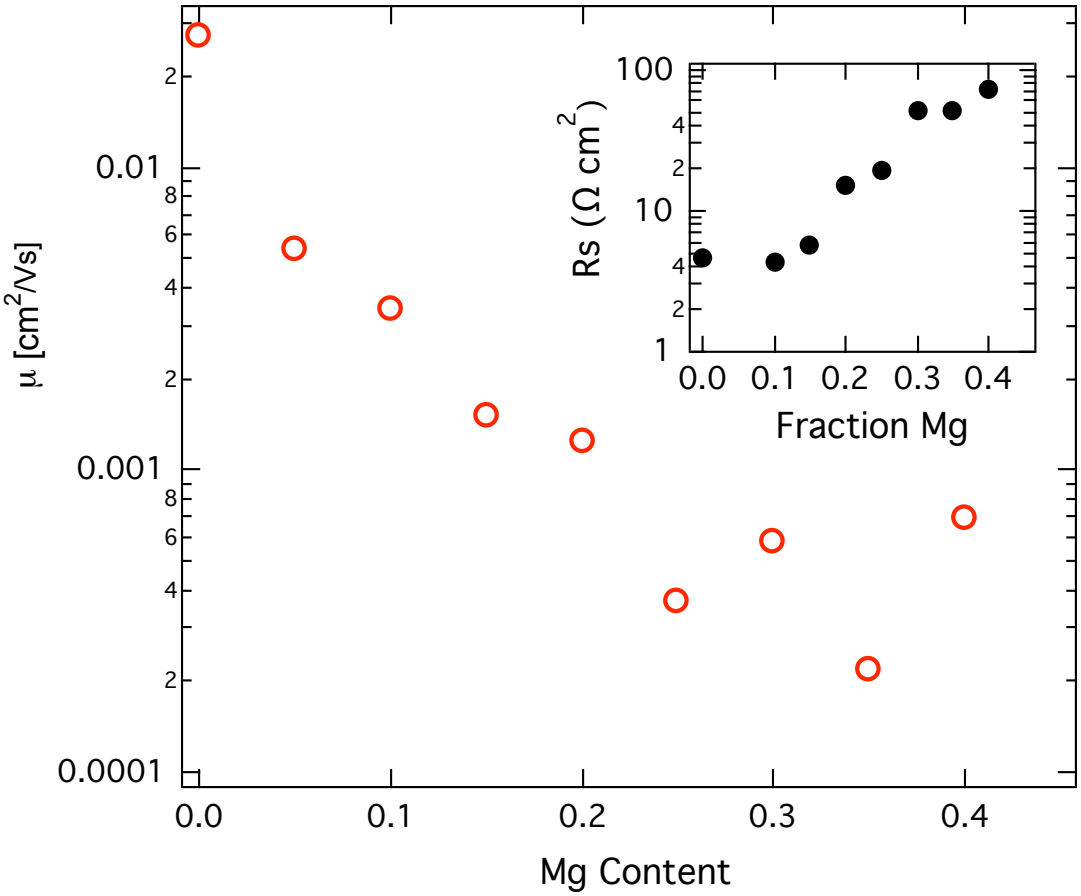

Figure 4.9 Time resolved microwave conductivity (TRMC) data showing the mobility of synthesized $Zn_{1-x}Mg_xO$ films ($0 < x < 0.40$) as a function of Mg content. Inset shows the series resistance of the device as a function of Mg content.

Two sources of P3HT were used to verify the observed trend, one synthesized in house, and another as purchased from Rieke Metals. The synthesized polymer was prepared from 2,5-dibromo-3-hexylthiophene via the Grignard metathesis or GRIM method.[143] Purification was by precipitation into methanol followed by soxhlet fractionation using initially methanol and then chloroform. The chloroform fraction was precipitated into methanol to give the desired polymer. The efficiency of devices made from the synthesized P3HT is seen to increase with Mg content up to an alloy

composition of $Zn_{0.75}Mg_{0.25}O$, after which the series resistance limits further improvement. Similar results are observed for the Rieke P3HT, though the J_{SC} values were dramatically higher with moderately lower V_{OC} values and dramatically reduced device performance above $Zn_{0.75}Mg_{0.25}O$ as seen in Figure 4.9. Though the trend of increased V_{OC} with increasing Mg content is the same for both polymers studied, the point at which the device efficiency begins to decrease is slightly different.

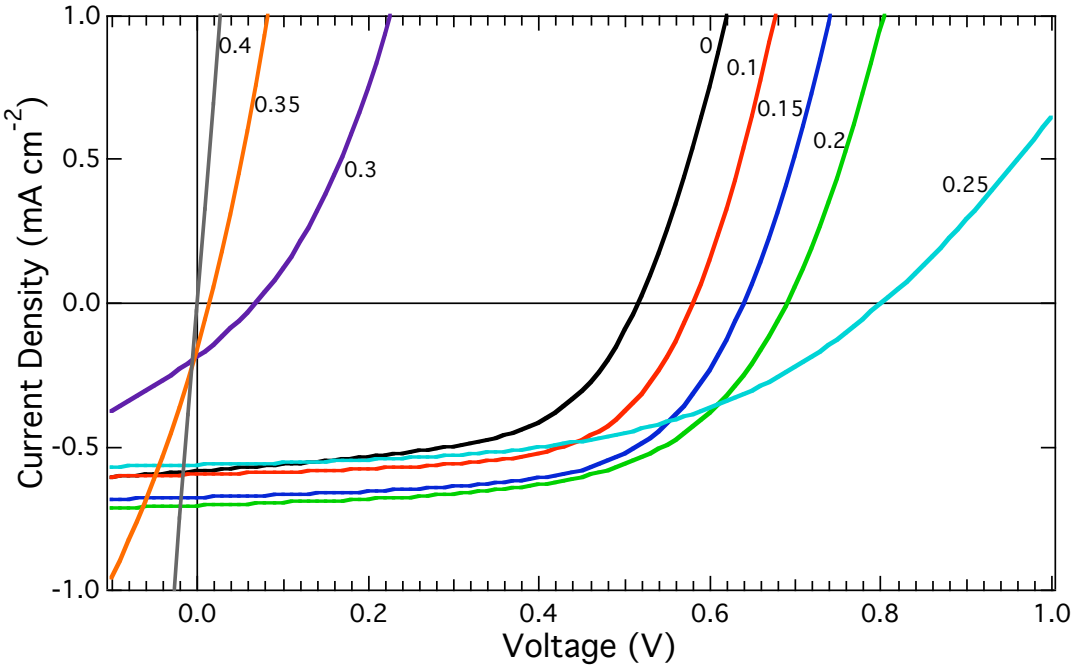

Figure 4.9 Current density vs. voltage of Rieke P3HT/ $Zn_{1-x}Mg_xO$ devices ($0 < x < 0.40$).

Lower series resistance values are observed in the devices incorporating the Rieke polymer, and as a result the FF is higher for these devices with values greater than 60%.

As mentioned above, the Rieke polymer shows an enhanced J_{SC} and reduced V_{OC} compared to the in-house P3HT. This result is interpreted as an increase in the disorder in the synthesized polymer film as can be inferred from the absorption spectra for the two films in Figure 4.10, which may result in a slight increase in the band gap and V_{OC}, as well as a reduction in the J_{SC} due to poor charge transport through the disordered polymer film. As the band gap increases the relative positions of the HOMO and LUMO of the polymer are likely to change to allow for increased V_{OC}. Similar results have been observed for polymer/fullerene bulk heterojunction devices.[133]

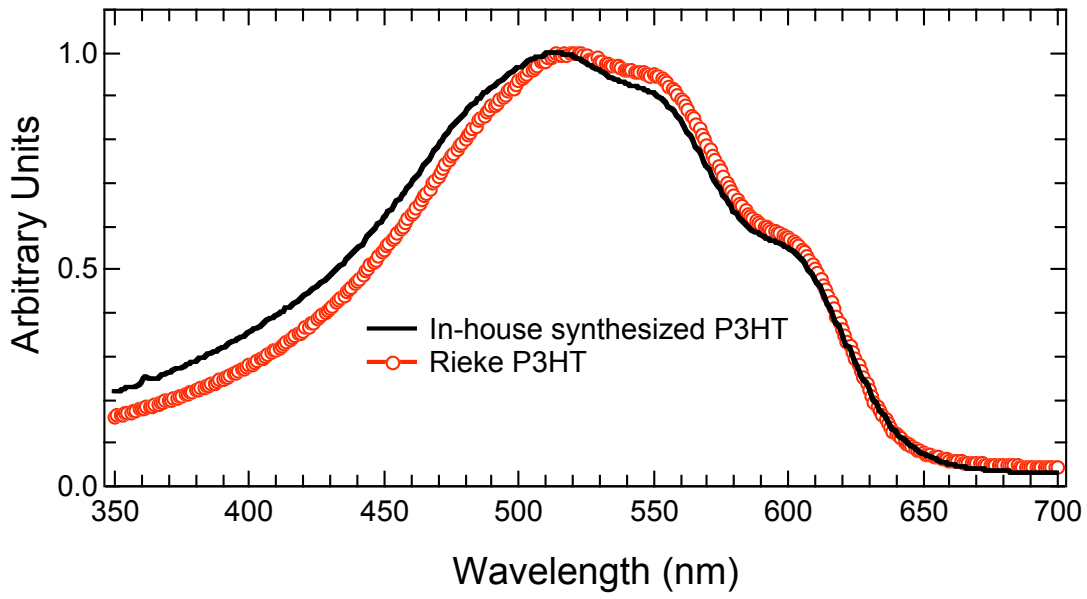

Figure 4.10 Normalized absorption spectra from thin films of synthesized P3HT (black line) and Rieke P3HT (open circles). Films were spin coated from 30 g/l chloroform solutions. The blue shift of the in-house synthesized P3HT relavtive to the Rieke material suggests greater disorder.

The $Zn_{1-x}Mg_xO$ devices demonstrate a moderate increase in J_{SC} for up to x = 0.20 in the case of the Rieke P3HT and x = 0.25 for the in-house P3HT. A separate set of $Zn_{1-x}Mg_xO$/P3HT devices were fabricated to look at the change in surface roughness with Mg content. Atomic force microscopy (AFM) revealed that the surface roughness of the films increased by a factor of two from 0 - 0.25 Mg. A similar trend was observed in the J_{SC} values. A likely explanation for the larger photocurrents is an increased interfacial area between the P3HT and $Zn_{1-x}Mg_xO$. Devices fabricated on $Zn_{0.75}Mg_{0.25}O$ using the Rieke P3HT exhibited a V_{OC} of 700 mV, a J_{SC} of 1.27 mA cm^{-2}, a FF of 56%, and a power conversion efficiency of 0.5% as seen in Figure 4.11. Similar efficiencies were observed in hybrid P3HT/ZnO nanofiber composite devices, where the interfacial area was much larger.

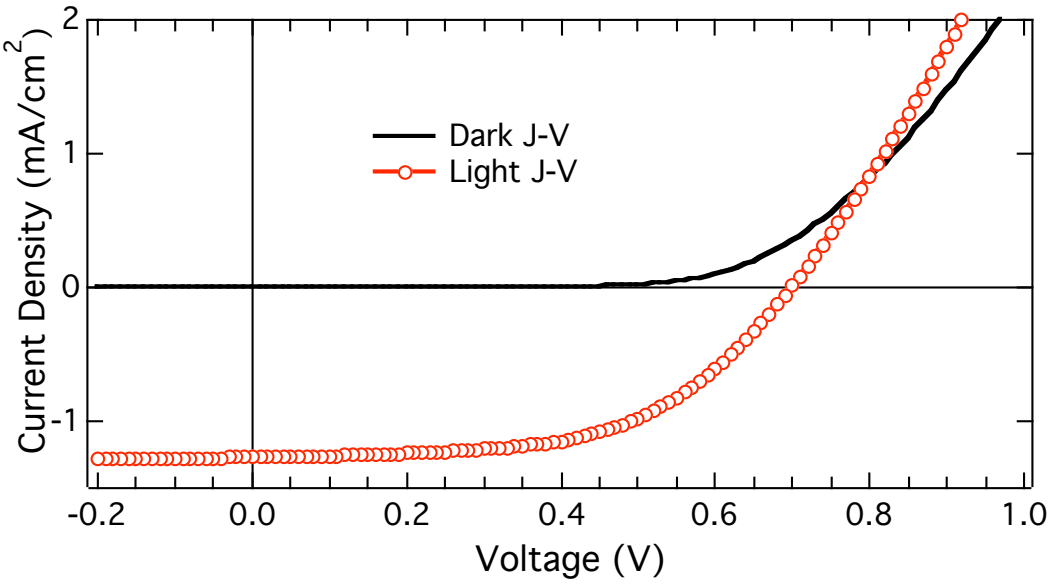

Figure 4.11 Current density vs. voltage of an increased surface roughness $Zn_{75}Mg_{25}O$/Rieke P3HT device. Dark J-V (black line), light J-V (open circles).

4.4 Summary

These results for P3HT/$Zn_{1-x}Mg_xO$ indicate that moving the conduction band of the electron acceptor closer to vacuum yields a systematic increase of V_{OC} as anticipated. The ability to easily tune the band offsets in hybrid polymer/ $Zn_{1-x}Mg_xO$ devices provides a tool for investigating the fundamental nature of the generation of photovoltage in these devices and provides a potential pathway to higher device efficiencies.

CHAPTER 5

CONCLUSIONS AND OUTLOOK

5.1 Conclusions

In this thesis, the aqueous solution growth of ZnO nanostructures that are vertically aligned from the substrate has been demonstrated. The ZnO nanofibers can be grown from a variety of nucleation layers including sputtered ZnO as well as ZnO grown from an annealed film of ZnAc deposited from solution. The morphology of the ZnO nanofibers is well suited for their incorporation into ordered hybrid polymer/ZnO solar cells.

Ordered hybrid polymer/ZnO nanofiber photovoltaic devices have been developed based on these ZnO nanofiber films. Results from hybrid photovoltaic devices made with P3HT/ZnO nanofiber composite structures have yielded an efficiency of 0.53% under AM1.5 illumination, significantly greater than that of similar bilayer devices. The increased efficiency is attributed to an increase in the area of the heterojunction interface in the P3HT/ZnO nanofiber device. Additionally, an increased efficiency of 0.61% was observed at higher light intensities, indicating the possible advantage of using high mobility electron transport pathways.

While these efficiencies are still lower than other hybrid organic/inorganic blend photovoltaic devices, there are clear limitations in the current device architecture, and several pathways can be pursued that may lead to higher efficiencies. The P3HT/ZnO nanofiber device was limited in photocurrent due to the large spacing between the ZnO fibers and poor polymer intercalation. Through the use of surface modifiers, the stability and performance were improved. In this work, this was overcome by blending PCBM

into the P3HT film. The enhanced exciton dissociation and efficient electron transfer from PCBM to the ZnO led to a very high photocurrent and a conversion efficiency in excess of 2% in the P3HT:PCBM/ZnO nanofiber device. The inverted device architecture allows for device fabrication and storage in air, which is largely prohibited in the majority of organic photovoltaic devices. As a result inverted P3HT:PCBM devices prepared in air demonstrated similar performance to non-inverted devices fabricated under an inert atmosphere.

The V_{OC} was further enhanced through the substitution of Mg into the ZnO crystal structure, which results in a material with an increased band gap. As a result of the increased band gap, the electron affinity was effectively reduced. The substitution of Mg for Zn in ZnO thereby decreases the band offset between the LUMO of the polymer donor and the conduction band of the acceptor metal oxide material. The V_{OC} was increased from 500 to 900 mV in the P3HT/$Zn_{1-x}Mg_xO$ devices through the substitution of Mg into ZnO. This is the highest published V_{OC} to date for P3HT based devices. The results for the bilayer devices indicate that moving the conduction band of the electron acceptor closer to the vacuum level yields a subsequent increase of the V_{OC} as anticipated, based on the accepted mechanism for determining V_{OC}. The ability to easily tune the band offsets in hybrid polymer/$Zn_{1-x}Mg_xO$ devices provides a tool for investigating the fundamental nature of the generation of photovoltage in these devices and provides a pathway to higher device efficiencies.

The band gap of the polymer absorber needs to be reduced to significantly increase the light absorption and overlap with the solar spectrum while maintaining or improving the charge transport properties of current polymers, as discussed in Chapter 1. The optimal band gap for a single junction solar cell is ~1.4 eV, which is still well below the band gap of polymers presently used in organic photovoltaic devices. If the band gap of the nanostructured accepter could be reduced while maintaining the proper band offset, the J_{SC} could be further improved while conserving V_{OC}. At present, such materials have

yet to be developed. Through their realization, additional gains in performance could be possible.

From this work, it can be concluded that ordered hybrid polymer/ZnO nanofiber composites might provide a path towards the realization of an inexpensive, large area solar cell technology. The nanostructured ZnO acceptor has improved charge collection over a planar ZnO acceptor. With proper optimization of the ZnO nanofiber morphology and the interfacial interactions between the polymer and oxide, devices with equivalent performance to the 5% polymer/fullerene bulk heterojunction devices should be observed. The improved charge transport characteristics of the ZnO nanofibers should provide the means to increase the active layer thickness and efficiency beyond what has been observed. Finally, the ability to adjust the band offset and increase the V_{OC} in hybrid polymer/inorganic devices should allow for dramatically higher efficiencies than established in present polymer solar cell technologies.

The most important outcome of this thesis is the understanding that has been gained of the problem at hand. Though these results have introduced more questions than answers, the paths toward improving the device performance have become more apparent.

5.2 Future Directions

Much work is still required in order to improve the performance of these devices. The reduction of the ZnO nanofiber spacing should lead to increased current density values. As demonstrated in this work and recently in other studies, ZnO nanofibers can be grown with closer spacing than were utilized in the optimized hybrid devices in this study. A simple reduction in the fiber spacing may not initially lead to increased performance, however, due to incomplete intercalation of the polymer into the ZnO nanofiber film. It then becomes necessary to study and optimize the interfacial

interactions between the polymer and inorganic semiconductor surface. This might be improved with surface modifiers as discussed in Chapter 3. Indeed, the most important interaction might be that of the top surface of the ZnO nanofiber with the polymer. If the vertical surfaces of the ZnO nanofibers are nonpolar and the top surfaces are polar and terminated in hydroxyl groups, then the reaction of a molecule such as a silane with only those hydroxyl groups may prove very beneficial to the device performance. This process could enhance the intercalation of the polymer dramatically, as the polymer has been shown to wet the vertical surface of the ZnO nanofibers very well.

Also, the ordered hybrid polymer/inorganic device might benefit from the incorporation of other metal oxides or nanostructured inorganic materials. For the immediate future, it is readily apparent that the device efficiency would be dramatically improved with the incorporation of $Zn_{1-x}Mg_xO$ nanofiber composites. It is anticipated that increasing the P3HT/$Zn_{1-x}Mg_xO$ interfacial area, for instance through nanostructuring of the $Zn_{1-x}Mg_xO$ material, would significantly enhance J_{SC} and thus produce dramatic increases in efficiency for hybrid polymer/nanostructured metal oxide solar cells. When the increased V_{OC} of the polymer/$Zn_{1-x}Mg_xO$ bilayer devices is combined with the enhanced J_{SC} of the polymer/ZnO nanofiber devices, the performance will certainly increase substantially above that presented in this study, as suggested by Figure 5.1 below.

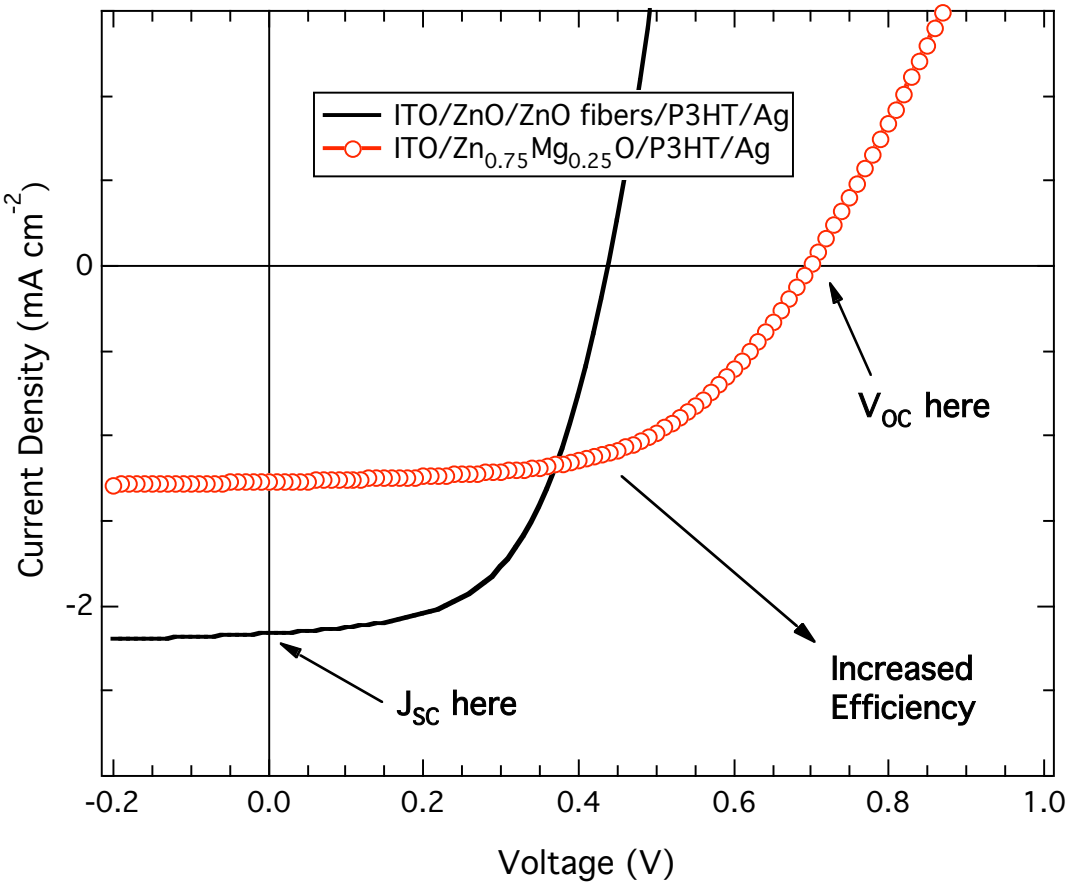

Figure 5.1 Current density vs. voltage curves for both the P3HT/ZnO nanofiber device (solid line) and the P3HT/$Zn_{75}Mg_{25}O$ device (open circles).

All of these steps should lead to improved performance in these ordered hybrid polymer/inorganic devices, and ultimately result in low-cost photovoltaic technology that could be manufactured via large-scale, roll-to-roll printing techniques. In addition, when combined with organic materials with improved charge transport properties and absorption spectra that are optimized for better overlap with the solar spectrum, the ultimate efficiency of these devices could potentially rival that of traditional solar cell technologies.

CHAPTER 6

REFERENCES

1. Margolis, R. M. Photovoltaic technology experience curves and markets. *NCPV and Solar Program Review* Denver, CO, (2003).

2. Shaheen, S. E., Ginley, D. S. and Jabbour, G. E. Organic-based photovoltaics: toward low-cost power generation. *MRS Bulletin* **30**, 10-15 (2005).

3. Shockley, W. and Queisser, H. J. Detailed balance limit of efficiency of p-n junction solar cells. *Journal of Applied Physics* **32**, 510-519 (1961).

4. Shaheen, S. E., Radspinner, R., Peyghambarian, N. and Jabbour, G. E. Fabrication of bulk heterojunction plastic solar cells by screen printing. *Applied Physics Letters* **79**, 2996-2998 (2001).

5. Brabec, C. J., Hauch, J. A., Schilinsky, P. and Waldauf, C. Production aspects of organic photovoltaics and their impact on the commercialization of devices. *MRS Bulletin* **30**, 50-52 (2005).

6. Gregg, B. A. and Hanna, M. C. Comparing organic to inorganic photovoltaic cells: theory, experiment, and simulation. *Journal of Applied Physics* **93**, 3605-3614 (2003).

7. Schweitzer, B. and Bässler, H. Excitons in conjugated polymers. *Synthetic Metals* **109**, 1-6 (2000).

8. Gregg, B. A. Bilayer molecular solar cells on spin-coated TiO_2 substrates. *Chemical Physics Letters* **258**, 376-380 (1996).

9. Gregg, B. A., Fox, M. A. and Bard, A. J. Photovoltaic effect in symmetrical cells of a liquid crystal porphyrin. *Journal of Physical Chemistry* **94**, 1586-1598 (1990).

10. Costa, P. G. d. and Conwell, E. M. Excitons and the band gap in poly(phenylene vinylene). *Physical Review B* **48**, 1993-1996 (1993).

11. Marks, R. N., Halls, J. J. M., Bradley, D. D. C., Friend, R. H. and Holmes, A. B. The photovoltaic response in poly(p-phenylene vinylene) thin-film devices. *Journal of Physics: Condensed Matter* **6**, 1379-1394 (1994).

12. Popovic, Z. D., Hor, A.-m. and Loutfy, R. O. A study of carrier generation mechanism in benzimidazole perylene/tetraphenyldiamine thin film structures. *Chemical Physics* **127**, 451-457 (1988).

13. Barth, S. and Bässler, H. Intrinsic photoconduction in PPV-type conjugated polymers. *Physical Review Letters* **79**, 4445-4448 (1997).

14. Liu, Y. Using resonance energy transfer to improve exciton harvesting in organic-inorganic hybrid solar cells. Ph.D.; Stanford University: Palo Alto, CA, (2005).

15. Peumans, P. Organic thin-film photodiodes. Ph.D.; Princeton University: Princeton, New Jersey, (2004).

16. Borsenberger, P. M., Pautmeier, L. and Bässler, H. Charge transport in disordered molecular solids. *Journal of Chemical Physics* **94**, 5447-5454 (1991).

17. Bässler, H. Charge transport in disordered organic photoconductors. *Physica Status Solidi (b)* **175**, 15-56 (1993).

18. Gartstein, Y. N. and Conwell, E. M. High-field hopping mobility in disordered molecular solids: A Monte Carlo study of off-diagonal disorder effects. *Journal of Chemical Physics* **100**, 9175-9180 (1994).

19. Lee, M.-T., Chen, H.-H., Liao, C.-H., Tsai, C.-H. and Chen, C. H. Stabe styrylamin-doped blue organic electroluminescent device based on 2-methyl-9,10-di(2-naphthyl)anthracene. *Applied Physics Letters* **85**, 3302-3304 (2004).

20. Burlakov, V. M., Kawata, K., Assender, H. E., Briggs, G. A. D., Ruseckas, A. and Samuel, I. D. W. Discrete hopping model of exciton transport in disordered media. *Physical Review B* **72**, 075206 (2005).

21. Kroeze, J. E., Savenije, T. J., Vermeulen, M. J. W. and Warman, J. M. Contactless determination of the photconductivity action spectrum, exciton diffusion length, and charge separation efficiency in pholythiophene-sensitized TiO2 bilayers. *Journal of Physical Chemistry B* **107**, 7696-7705 (2003).

22. Pettersson, L. A. A., Roman, L. S. and Inganäs, O. Modeling photocurrent action spectra of photovoltaic devices based on organic thin films. *Journal of Applied Physics* **86**, 487-496 (1999).

23. Savenije, T. J., Warman, J. M. and Goossens, A. Visible light sensitisation of titanium dioxide using a phenylene vinylene polymer. *Chemical Physics Letters* **287**, 148-153 (1998).

24. Halls, J. J. M., Pichler, K., Friend, R. H., Moratti, S. C. and Holmes, A. B. Exciton diffusion and dissociation in a poly(p-phenylenevinylene)/C_{60} heterojunction photovoltaic cells. *Applied Physics Letters* **68**, 3120-3122 (1996).

25. Mollay, B., Lemmer, U., Kersting, R., Mahrt, R. F., Kurz, H., Kauffmann, H. F. and Bässler, H. Dynamics of singlet excitations in conjugated polymers: Poly(phenylenevinylene) and poly(phenylphenylenevinylene). *Physical Review B* **50**, 10769-10779 (1994).

26. Turro, N. J. Modern Molecular Photochemistry. Benjamin/Cummings Publishing, Menlo Park, CA, (1978).

27. Förster, T. Transfer mechanisms of electronic excitation. *Discussions of the Faraday Society* **27**, 7-17 (1959).

28. Sariciftci, N. S., Smilowitz, L., Heeger, A. J. and Wudl, F. Photoinduced electron-transfer from a conducting polymer to buckminsterfullerene. *Science* **258**, 1474-1476 (1992).

29. Brabec, C. J., Zerza, G., Cerullo, G., Silvestri, S. D., Luzzati, S., Hummelen, J. C. and Sariciftci, S. Tracing photoinduced electron transfer process in conjugated polymer/fullerene bulk heterojunctions in real time. *Chemical Physics Letters* **340**, 232-236 (2001).

30. Nogueira, A. F., Montanari, I., Nelson, J., Durrant, J. R., Winder, C., Sariciftci, N. S. and Brabec, C. Charge recombination in conjugated polymer/fullerene blended films studied by transient absorption spectroscopy. *Journal of Physical Chemistry B* **107**, 1567-1573 (2003).

31. Al-Ibrahim, M., Roth, H.-K., Zhokhavets, U., Gobsch, G. and Sensfuss, S. Flexible large area polymer solar cells based on poly(3-hexylthiophene)/fullerene. *Solar Energy Materials & Solar Cells* **85**, 13-20 (2005).

32. Brabec, C. J., Cravino, A., Meissner, D., Sariciftci, N. S., Fromherz, T., Rispens, M. T., Sanchez, L. and Hummelen, J. C. Origin of the open circuit voltage of plastic solar cells. *Advanced Functional Materials* **11**, 374-380 (2001).

33. Arango, A. C., Carter, S. A. and Brock, P. J. Charge transfer in photovoltaics consisting of interpenetrating networks of conjugated polymer and TiO2 nanoparticles. *Applied Physics Letters* **74**, 1698-1700 (1999).

34. Shirakawa, T., Umeda, T., Hashimoto, Y., Fujii, A. and Toshino, K. Effect of ZnO layer on characteristics of conducting polymer/C60 photovoltaic cell. *Journal of Physics D: Applied Physics* **37**, 847-850 (2004).

35. Beek, W. J. E., Wienk, M. M., Kemerink, M., Yang, X. and Janssen, R. A. J. Hybrid Zinc Oxide conjugated polymer bulk heterojunction solar cells. *Journal of Physical Chemistry B* **109**, 9505-9516 (2005).

36. Tang, C. W. Two-layer organic photovoltaic cell. *Applied Physics Letters* **48**, 183-185 (1986).

37. Sariciftci, N. S., Braun, D., Zhang, C., Srdanov, V. I., Heeger, A. J., Stucky, G. and Wudl, F. Semiconducting polymer-buckminsterfullerene heterojunctions: diodes, photodiodes, and photovoltaic cells. *Applied Physics Letters* **62**, 585-587 (1993).

38. Yu, G., Gao, J., Hummelen, J. C., Wudl, F. and Heeger, A. J. Polymer photovoltaic cells: enhanced efficiencies via a network of internal donor-acceptor heterojunctions. *Science* **270**, 1789-1791 (1995).

39. Peumans, P., Yakimov, A. and Forrest, S. R. Small molecular weight organic thin-film photodetectors and solar cells. *Journal of Applied Physics* **93**, 3693-3723 (2003).

40. Forrest, S. R. The limits to organic photovoltaic cell efficiency. *MRS Bulletin* **30**, 28-32 (2005).

41. Padinger, F., Rittberger, R. S. and Sariciftci, N. S. Effects of postproduction treatment on plastic solar cells. *Advanced Functional Materials* **13**, 85-88 (2003).

42. Li, G., Shrotriya, V., Huang, J., Yao, Y., Moriarty, T., Emery, K. and Yang, Y. High-efficiency solution processable polymer photovoltaic cells by self-organization of polymer blends. *Nature Materials* **4**, 864-868 (2005).

43. Ma, W., Yang, C., Gong, X., Lee, K. and Heeger, A. J. Thermally stable, efficient polymer solar cells with nanoscale control of the interpenetrating network morphology. *Advanced Functional Materials* **15**, 1617-1622 (2005).

44. Shaheen, S. E., Brabec, C. J., Sariciftci, N. S., Padinger, F., Fromherz, T. and Hummelen, J. C. 2.5% efficient organic plastic solar cells. *Applied Physics Letters* **78**, 841-843 (2001).

45. Hoppe, H., Niggemann, M., Winder, C., Kraut, J., Hiesgen, R., Hinsch, A., Meissner, D. and Sariciftci, N. S. Nanoscale morphology of conjugated polymer/fullerene-based bulk-heterojunction solar cells. *Advanced Functional Materials* **14**, 1005-1011 (2004).

46. Duren, J. K. J. v., Yang, X., Loos, J., Bulle-Lieuwma, C. W. T., Sieval, A. B., Hummelen, J. C. and Janssen, R. A. J. Relating the morphology of poly(p-phenylene vinylene)/methanofullerene blends to solar-cell performance. *Advanced Functional Materials* **14**, 425-434 (2004).

47. Chirvase, D., Parisi, J., Hummelen, J. C. and Dyakonov, V. Influence of nanomorphology on the photovoltaic action of polymer-fullerene composites. *Nanotechnology* **15**, 1317-1323 (2004).

48. Zhao, Y., Yuan, G. X., Roche, P. and Leclerc, M. *Polymer* **36**, 2211 (1995).

49. Brown, P. J., Thomsa, D. S., Köhler, A., Wilson, J. S., Kim, J.-S., Ramsdale, C. M., Sirringhaus, H. and Friend, R. H. Effect of interchain interactions on the absorption and emission of poly(3-hexylthiophene). *Physical Review B* **67**, 064203 (2003).

50. Salaneck, W. R., Inganäs, O., Thémans, B., Nilsson, J. O. and Sjögren, B. Thermochromism in poly(3-hexylthiophene) in the solid state: a spectroscopic study of temperature-dependent conformational defects. *Journal of Chemical Physics* **89**, 4613-4619 (1988).

51. Roux, C. and Leclerc, M. Rod-to-coil transition in alkoxy-substituted polythiophenes. *Macromolecules* **25**, 2141-2144 (1992).

52. Yang, C., Orfino, F. P. and Holdcroft, S. A phenomenological model for predicting thermochromism of regioregular and nonregioregular poly(3-alkylthiophenes). *Macromolecules* **29**, 6510-6517 (1996).

53. Theander, M., Svensson, M., Ruseckas, A., Zigmantas, D., Sundström, V., Andersson, M. R. and Inganäs, O. High luminescence from a substituted polythiophene in a solvent with low solubility. *Chemical Physics Letters* **337**, 277-283 (2001).

54. Erb, T., Zhokhavets, U., Gobsch, G., Raleva, S., Stühn, B., Schilinsky, P., Waldauf, C. and Brabec, C. J. Correlation between structural and optical properties of composite polymer/fullerene films for organic solar cells. *Advanced Functional Materials* **15**, 1193-1196 (2005).

55. Janssen, R. A. J., Hummelen, J. C. and Sariciftci, N. S. Polymer-fullerene bulk heterojunction solar cells. *MRS Bulletin* **30**, 33-36 (2005).

56. Brabec, C. J., Winder, C., Sariciftci, N. S., Hummelen, J. C., Dhanabalan, A., Hal, P. A. v. and Janssen, R. A. J. A low-bandgap semiconducting polymer for photovoltaic devices and infrared emitting diodes. *Advanced Functional Materials* **12**, 709-712 (2002).

57. Huynh, W. U., Dittmer, J. J. and Alivisatos, A. P. Hybrid nanorod-polymer solar cells. *Science* **295**, 2425-2427 (2002).

58. Li, L.-s., Hu, J., Yang, W. and Alivisatos, A. P. Band gap variation of size- and shape-controlled colloidal CdSe quantum rods. *Nano Letters* **1**, 349-351 (2001).

59. Huynh, W. U., Dittmer, J. J., Teclemariam, N., Milliron, D. J., Alivisatos, A. P. and Barnham, K. W. J. Charge transport in hybrid nanorod-polymer composite photovoltaic cells. *Physical Review B* **67**, 115326 (2003).

60. Ginger, D. S. and Greenham, N. C. Charge transport in semiconductor nanocrystals. *Synthetic Metals* **124**, 117-120 (2001).

61. Ginger, D. S. and Greenham, N. C. Charge injection and transport in films of CdSe nanocrystals. *Journal of Applied Physics* **87**, 1361-1368 (2000).

62. Huynh, W. U., Dittmer, J. J., Libby, W. C., Whiting, G. L. and Alivisatos, A. P. Controlling the morphology of nanocrystal-polymer composites for solar cells. *Advanced Functional Materials* **13**, 73-79 (2003).

63. Anderson, N. A., Hao, E., Ai, X., Hastings, G. and Lian, T. Ultrafast and long-lived photoinduced charge separation in MEH-PPV/nanoporous semiconductor thin film composites. *Chemical Physics Letters* **347**, 304-310 (2001).

64. Roest, A. L., Kelly, J. J., Vanmaekelbergh, D. and Meulenkamp, E. A. Staircase in electron mobility of a ZnO quantum dot assembly due to shell filling. *Physical Review Letters* **89**, 036801 (2002).

65. Hal, P. A. v., Wienk, M. M., Kroon, J. M., Verhees, W. J. H., Slooff, L. H., Gennip, W. J. H. v., Jonkheijm, P. and Janssen, R. A. J. Photoinduced electron transfer and photovoltaic response of a MDMO-PPV:TiO2 bult-heterojunction. *Advanced Materials* **15**, 118-121 (2003).

66. Beek, W. J. E., Wienk, M. M. and Janssen, R. A. J. Efficient hybrid solar cells from zinc oxide nanoparticles and a conjugated polymer. *Advanced Materials* **16**, 1009-1013 (2004).

67. Kwong, C. Y., Djurišić, A. B., Chui, P. C., Cheng, K. W. and Chan, W. K. Influence of solvent on film morphology and device performance of poly(3-hexylthiophene):TiO_2 nanocomposite solar cells. *Chemical Physics Letters* **384**, 372-375 (2004).

68. Coakley, K. M., Liu, Y., Goh, C. and McGehee, M. D. Ordered organic-inorganic bulk heterojunction photovoltaic cells. *MRS Bulletin* **30**, 37-40 (2005).

69. Kannan, B., Castelino, K. and Majumdar, A. Design of nanostructured heterojunction polymer photovoltaic devices. *Nano Letters* **3**, 1729-1733 (2003).

70. Grätzel, M. Photoelectrochemical cells. *Nature* **414**, 338-344 (2001).

71. Gong, D., Grimes, C. A., Varghese, O. K., Hu, W., Singh, R. S., Chen, Z. and Dickey, E. C. Titanium oxide nanotube arrays prepared by anodic oxidation. *Journal of Materials Research* **16**, 3331-3334 (2001).

72. Vayssieres, L. Growth of arrayed nanorods and nanowires of ZnO from aqueous solutions. *Advanced Materials* **15**, 464-466 (2003).

73. Coakley, K. M., Liu, Y., McGehee, M. D., Frindell, K. L. and Stucky, G. D. Infiltrating semiconducing polymers into self-assembled mesoporous titania films for photovoltaic applications. *Advanced Functional Materials* **13**, 301-306 (2003).

74. Breeze, A. J., Schlesinger, Z., Carter, S. A. and Brock, P. J. Charge transport in TiO_2/MEH-PPV polymer photovoltaics. *Physical Review B* **64**, 125205 (2001).

75. Coakley, K. M. and McGehee, M. D. Photovoltaic cells made from conjugated polymers infiltrated into mesoporous titania. *Applied Physics Letters* **83**, 3380-3382 (2003).

76. Ravirajan, P., Haque, S. A., Durrant, J. R., Bradley, D. D. C. and Nelson, J. The effect of polymer optoelectronic properties on the performance of multilayer hybrid polymer/TiO2 solar cells. *Advanced Functional Materials* **15**, 609-618 (2005).

77. Coakley, K. M., Srinivasan, B. S., Ziebarth, J. M., Goh, C., Liu, Y. and McGehee, M. D. Enhanced hole mobility in regioregular polythiophene infiltrated in straight nanopores. *Advanced Functional Materials* **15**, 1927-1932 (2005).

78. McBranch, D., Campbell, I. H. and Smith, D. L. Optical determination of chain orientation in electroluminescent polymer films. *Applied Physics Letters* **66**, 1175-1177 (1995).

79. Konenkamp, R., Dloczik, L., Ernst, K. and Olesch, C. Nano-structures for solar cells with extremely thin absorbers. *Physica E* **14**, 219-223 (2002).

80. Law, M., Greene, L. E., Johnson, J. C., Saykally, R. and Yang, P. Nanowire dye-sensitized solar cells. *Nature Materials* **4**, 455-459 (2005).

81. Greene, L. E., Law, M., Tan, D. H., Montano, M., Goldberger, J., Somorjai, G. and Yang, P. General route to vertical ZnO nanowire arrays using textured ZnO seeds. *Nano Letters* **5**, 1231-1236 (2005).

82. Peterson, R. B., Fields, C. L. and Gregg, B. Epitaxial chemical deposition of ZnO nanocolumns from NaOH solutions. *Langmuir* **20**, 5114-5118 (2004).

83. Ohyama, M., Kozuka, H. and Yoko, T. Sol-gel preparation of ZnO films with extremely preferred orientation along (002) plane from zinc acetate solution. *Thin Solid Films* **306**, 78-85 (1997).

84. Zhang, X., Li, X. M., Chen, T. L., Bian, J. M. and Zhang, C. Y. Structural and optical properties of $Zn_{1-x}Mg_xO$ thin films deposited by ultrasonic spray pyrolysis. *Thin Solid Films* **492**, 248-252 (2005).

85. O'Regan, B. and Grätzel, M. A low-cost, high-efficiency solar cell based on dye-sensitized colloidal TiO_2 films. *Nature* **353**, 737-740 (1991).

86. Rensmo, H., Keis, K., Lindström, H., Södergren, S., Solbrand, A., Hagfeldt, A., Lindquist, S.-E., Wang, L. N. and Muhammed, M. High light-to-energy conversion efficiencies for solar cells based on nanostructured ZnO electrodes. *Journal of Physical Chemistry B* **101**, 2598-2601 (1997).

87. Keis, K., Magnusson, E., Lindström, H., Lindquist, S.-E. and Hagfeldt, A. A 5% efficient photoelectrochemical solar cell based on nanostructured ZnO electrodes. *Solar Energy Materials & Solar Cells* **73**, 51-58 (2002).

88. Beermann, N., Vayssieres, L., Lindquist, S.-E. and Hagfeldt, A. Photoelectrochemical studies of oriented nanorod thin films of hematite. *Journal of The Electrochemical Society* **147**, 2456-2461 (2000).

89. Kang, Y., Park, N.-G. and Kim, D. Hybrid solar cells with vertically aligned CdTe nanorods and a conjugated polymer. *Applied Physics Letters* **86**, 113101 (2005).

90. Huang, M. H., Wu, Y., Feick, H., Tran, N., Weber, E. and Yang, P. Catalytic growth of zinc oxide nanowires by vapor transport. *Advanced Materials* **13**, 113-116 (2001).

91. Yang, P., Yan, H., Mao, S., Russo, R., Johnson, J., Saykally, R., Morris, N., Pham, J., He, R. and Choi, H.-J. Controlled growth of ZnO nanowires and their optical properties. *Advanced Functional Materials* **12**, 323-331 (2002).

92. Baxter, J. B. and Aydil, E. S. Epitaxial growth of ZnO nanowires on a- and c-plane sapphire. *Journal of Crystal Growth* **274**, 407-411 (2005).

93. Li, Y., Meng, G. W., Zhang, L. D. and Phillipp, F. Ordered semiconductor ZnO nanowire arrays and their photoluminescence properties. *Applied Physics Letters* **76**, 2011-2013 (2000).

94. Liu, R., Vertegel, A. A., Bohannan, E. W., Sorenson, T. A. and Switzer, J. A. Epitaxial electrodeposition of zinc oxide nanopillars on single-crystal gold. *Chemistry of Materials* **13**, 508-512 (2001).

95. O'Regan, B., Sklover, V. and Grätzel, M. Electrochemical deposition of smooth and homogeneously mesoporous ZnO films from propylene carbonate electrolytes. *Journal of The Electrochemical Society* **148**, C498-C505 (2001).

96. Vayssieres, L., Keis, K., Lindquist, S.-E. and Hagfeldt, A. Purpose-built anisotropic metal oxide material: 3D highly oriented microrod array of ZnO. *Journal of Physical Chemistry B* **105**, 3350-3352 (2001).

97. Hsu, J. W. P., Tian, Z. R., Simmons, N. C., Matzke, C. M., Voigt, J. A. and Liu, J. Directed spatial organization of zinc oxide nanorods. *Nano Letters* **5**, 83-86 (2005).

98. Govender, K., Boyle, D. S., Kenway, P. B. and O'Brien, P. Understanding the factors that govern the deposition and morphology of thin films of ZnO from aqueous solution. *Journal of Materials Chemistry* **14**, 2575-2591 (2004).

99. Sounart, T. L., Liu, J., Voigt, J. A., Hsu, J. W. P., Spoerke, E. D., Tian, Z. and Jiang, Y. Sequential Nucleation and Growth of Complex Nanostructured Films. *Advanced Functional Materials* **16**, 335-344 (2006).

100. Tian, Z. R., Voigt, J. A., Liu, J., Mckenzie, B., Mcdermott, M. J., Rodriquez, M. A., Konishi, H. and Xu, H. Complex and oriented ZnO nanostructures. *Nature Materials* **2**, 821-826 (2003).

101. Yamabi, S. and Imai, H. Growth conditions for wurtzite zinc oxide films in aqueous solutions. *Journal of Materials Chemistry* **12**, 3773-3778 (2002).

102. Li, W.-J., Shi, E.-W., Zhong, W.-Z. and Yin, Z.-W. Growth mechanism and growth habit of oxide crystals. *Journal of Crystal Growth* **203**, 186 (1999).

103. Liu, T.-Q., Sakurai, O., Mizutani, N. and Kato, M. Preparation of spherical fine ZnO particles by the spray pyrolysis method using ultrasonic atomization techniques. *Journal of Materials Science* **21**, 3698-3702 (1986).

104. Shalish, I., Temkin, H. and Narayanamurti, V. Size-dependent surface luminescence in ZnO nanowires. *Physical Review B* **69**, 245401 (2004).

105. Cross, R. B. M., Souza, M. M. D. and Narayanan, E. M. S. A low temperature combination method for the production of ZnO nanowires. *Nanotechnology* **16**, 2188-2192 (2005).

106. Greene, L. E., Law, M., Goldberger, J., Kim, F., Johnson, J. C., Zhang, Y., Saykally, R. J. and Yang, P. Low-temperature wafer-scale production of ZnO nanowire arrays. *Angewandte Chemie* **42**, 3031-3034 (2003).

107. Yan, H., Huang, Q., Cui, J., Veinot, J. G. C., Kern, M. M. and Marks, T. J. High-brightness blue light-emitting polymer diodes via anode modification using a self-assembled monolayer. *Advanced Materials* **15**, 835-838 (2003).

108. Sommeling, P. M., Rieffe, H. C., Roosmalen, J. A. M. v., Schönecher, A., Kroon, J. M., Wienke, J. A. and Hinsch, A. Spectral response and IV-characterization of dye-sensitized nanocrystalline TiO2 solar cells. *Solar Energy Materials & Solar Cells* **62**, 399-410 (2000).

109. Kroon, J. M., Wienk, M. M., Verhees, W. J. H. and Hummelen, J. C. Accurate efficiency determination and stability studies of conjugated polymer/fullerene solar cells. *Thin Solid Films* **403-404**, 223-228 (2002).

110. Eastment, R. M. and Mee, C. H. B. Work function measurements on (100), (110) and (111) surfaces of aluminium. *Journal of Physics F: Metal Physics* **3**, 1738-1745 (1973).

111. Dweydari, A. W. and Mee, C. H. B. *Physica Status Solidi A* **27**, 223 (1975).

112. Eastman, D. E. Photoelectric work functions of transition, rare-earth, and noble metals. *Physical Review B* **2**, 1-2 (1970).

113. Mihailetchi, V. D., Koster, L. J. A. and Blom, P. W. M. Effect of metal electrodes on the performance of polymer:fullerene bulk heterojunction solar cells. *Applied Physics Letters* **85**, 970-972 (2004).

114. Lachkar, A., Selmani, A., Sacher, E., Leclerc, M. and Mokhliss, R. Metallization of polythiophenes I. Interaction of vapor-deposited Cu, Ag and Au with poly(3-hexylthiophene) (P3HT). *Synthetic Metals* **66**, 209-215 (1994).

115. Kohan, A. F., Ceder, G., Morgan, D. and Walle, C. G. V. d. First-principles study of native point defects in ZnO. *Physical Review B* **61**, 15019-15027 (2000).

116. Mahan, G. D. Intrinsic defects in ZnO varistors. *Journal of Applied Physics* **54**, 3825-3832 (1983).

117. Ong, B., Wu, Y., Jiang, L., Liu, P. and Murti, K. Polythiophene-based field-effect transistors with enhanced air stability. *Synthetic Metals* **142**, 49-52 (2004).

118. Ong, B. S., Wu, Y., Liu, P. and Gardner, S. High-performance semiconducting polythiophenes for organic thin-film transistors. *Journal of the American Chemical Society* **126**, 3378-3379 (2004).

119. Kang, H. S., Kang, J. S., Kim, J. W. and Lee, S. Y. Annealing effect on the property of ultraviolet and green emissions of ZnO thin films. *Journal of Applied Physics* **95**, 1246-1250 (2004).

120. Olson, D. C., Shaheen, S. E., Collins, R. T. and Ginley, D. S. A hybrid photovoltaic device from poly(3-hexylthiophene) intercalated into ZnO nanofibers. *Advanced Functional Materials* In Press. (2006).

121. Xue, J., Uchida, S., Rand, B. P. and Forrest, S. R. 4.2% efficient organic photovoltaic cells with low series resistances. *Applied Physics Letters* **84**, 3013-3015 (2004).

122. Olson, D. C., Piris, J., Collins, R. T., Shaheen, S. E. and Ginley, D. S. Hybrid photovoltaic devices of polymer and ZnO nanofiber composites. *Thin Solid Films* **496**, 26-29 (2006).

123. Deng, X. Y., Lau, W. M., Wong, K. Y., Low, K. H., Chow, H. F. and Cao, Y. High efficiency low operating voltage polymer light-emitting diodes with aluminum cathode. *Applied Physics Letters* **84**, 3522-3524 (2004).

124. Niu, Y.-H., Ma, H., Xu, Q. and Jen, A. K.-Y. High-efficiency light-emitting diodes using neutral surfactants and aluminum cathode. *Applied Physics Letters* **86**, 083504 (2005).

125. Brabec, C. J., Sariciftci, N. S. and Hummelen, J. C. Plastic solar cells. *Advanced Functional Materials* **11**, 15-26 (2001).

126. Coakley, K. M. and McGehee, M. D. Conjugated polymer photovoltaic cells. *Chemistry of Materials* **16**, 4533-4542 (2004).

127. Brabec, C. J., Koppe, M., Morana, M., Muehlbacher, D., Waldauf, C., Denk, P. and Scharber, M. C. Advances in the performance of organic bulk heterojunction solar cells: towards first products. *SPIE Annual Meeting* San Diego, (2005).

128. Gregg, B. A. The photoconversion mechanism of excitonic solar cells. *MRS Bulletin* **30**, 20-22 (2005).

129. Heller, C. M., Campbell, I. H., Smith, D. L., Barashkov, N. N. and Ferraris, J. P. Chemical potential pinning due to equilibrium electron transfer at metal/C60-doped polymer interfaces. *Journal of Applied Physics* **81**, 3227-3231 (1997).

130. Frohne, H., Shaheen, S. E., Brabec, C. J., Müller, D. C., Sariciftci, N. S. and Meerholz, K. Influence of the anodic work function on the performance of organic solar cells. *ChemPhysChem* **3**, 795-799 (2002).

131. Mihailetchi, V. D., Blom, P. W. M., Hummelen, J. C. and Rispens, M. T. Cathode dependence of the open-circuit voltage of polymer:fullerene bulk heterojunction solar cells. *Journal of Applied Physics* **94**, 6849-6854 (2003).

132. Gadisa, A., Svensson, M., Andersson, M. R. and Inganäs, O. Correlation between oxidation potential and open-circuit voltage of composite solar cells based on blends of polythiophenes/fullerene derivative. *Applied Physics Letters* **84**, 1609-1611 (2004).

133. Liu, J., Shi, Y. and Yang, Y. Solvation-induced morhpology effects on the performance of polymer-based photovoltaic devices. *Advanced Functional Materials* **11**, 420-424 (2001).

134. Ohtomo, A., Kawasaki, M., Koida, T., Masubuchi, K., Koinuma, H., Sakurai, Y., Yoshida, Y., Yasuda, T. and Segawa, Y. $Mg_xMn_{1-x}O$ as a II-VI widegap semiconductor alloy. *Applied Physics Letters* **72**, 2466-2468 (1998).

135. Chen, L., Ye, Z., Ma, D., Zhao, B., Ling, C. and Zhu, L. Influence of Ar/O_2 gas ratios on the crystal quality and band gap of $Zn_{1-x}Cd_xO$ thin films. *Journal of Crystal Growth* **274**, 458-463 (2005).

136. Matsubara, K., Tampo, H., Shibata, H., Yamada, A., Fons, P., Iwata, K. and Niki, S. Band-gap modified Al-doped $Zn_{1-x}Mg_xO$ transparent conducting films deposited by pulsed laser deposition. *Applied Physics Letters* **85**, 1374-1376 (2004).

137. Zhao, D., Liu, Y., Shen, D., Lu, Y., Zhang, J. and Fan, X. Photoluminescence properties of $Mg_xZn_{1-x}O$ alloy thin films fabricated by the sol-gel deposition method. *Journal of Applied Physics* **90**, 5561-5563 (2001).

138. Rao, G. V., Säuberlich, F. and Klein, A. Influence of Mg content on the band alignment at CdS/(Zn,Mg)O interfaces. *Applied Physics Letters* **87**, 032101 (2005).

139. Liang, W. Y. and Yoffe, A. D. Transmission spectra of ZnO single crystals. *Physical Review Letters* **20**, 59-62 (1968).

140. Park, W. I. and Yi, G.-C. Electroluminescence in n-ZnO nanorod arrays vertically grown on p-GaN. *Advanced Materials* **16**, 87-90 (2004).

141. Piris, J. and Kopidakis, N. Private Communication (2005).

142. Kaneto, K., Hatae, K., Nagamatsu, S., Takashima, W. and Pandey, S. S. Photocarrier mobility in regioregular poly(3-hexylthiophene) studied by the time of flight method. *Japanese Journal of Applied Physics* **38**, L1188-L1190 (1999).

143. Loewe, R. S., Khersonsky, S. M. and McCullough, R. D. A simple method to prepare head-to-tail coupled, regioregular poly(3-alkylthiophenes) using Grignard Metathesis. *Advanced Materials* **11**, 250-253 (1999).